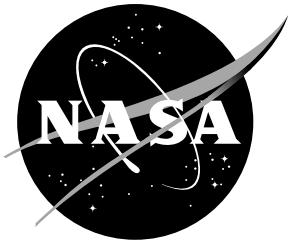


NASA Technical Memorandum 110325



The Upper Atmosphere Research Satellite In-Flight Dynamics

Stanley E. Woodard
Langley Research Center, Hampton, Virginia

April 1997

National Aeronautics and
Space Administration
Langley Research Center
Hampton, Virginia 23681-0001

Abstract

Upper Atmosphere Research Satellite flight data from the first 737 days after launch (September 1991) was used to investigate spacecraft disturbances and responses. The investigation included two in-flight dynamics experiments (approximately three orbits each). Orbital and configuration influences on spacecraft dynamic response were also examined. Orbital influences were due to temperature variation from crossing the Earth's terminator and variation of the solar incident energy as the orbit precessed. During the terminator crossing, the rapid ambient temperature change caused the spacecraft's two flexible appendages to experience thermal elastic bending (thermal snap). The resulting response was dependent upon the orientation of the solar array and the solar incident energy. Orbital influences were also caused by on-board and environmental disturbances and spacecraft configuration changes resulting in dynamic responses which were repeated each orbit. Configuration influences were due to solar array rotation changing spacecraft modal properties. The investigation quantified the spacecraft dynamic response produced by the solar array and high gain antenna harmonic drive disturbances. The solar array's harmonic drive output resonated two solar array modes. Friction in the solar array gear drive provided sufficient energy dissipation which prevented the solar panels from resonating catastrophically; however, the solar array vibration amplitude was excessively large. The resulting vibration had a latitude-specific pattern.

CONTENTS

Abstract	i
Contents.....	ii
Nonmenclature.....	iii
1. Introduction.....	1
1.1 UARS In-Flight Dynamics Study Highlights.....	3
1.2 Publications and Presentations.....	1
2. UARS Overview.....	5
2.1 Science Measurement Characteristics	6
2.2 Disturbances Known Before Launch.....	7
2.3 Attitude Determination.....	7
2.4 Spacecraft Physical Characteristics	7
3. Typical UARS Orbital Dynamics.....	9
3.1 UARS Subsystems.....	10
3.1.1 Modular Attitude Control System.....	10
3.1.2 Inertial Reference Unit Gyros	10
3.1.3 Solar Array	11
3.1.4 High Gain Antenna.....	11
3.1.5 Solar Stellar Pointing Platform.....	12
3.2 Instruments.....	13
3.2.1 Halogen Occultation Experiment	13
3.2.2 High Resolution Doppler Imager.....	13
3.2.3 Microwave Limb Sounder	14
3.2.4 Elastically Flexible-Body Motion	15
4. Subsystem and Instrument Contribution to Space Dynamic Response.....	17
4.1 Solar Array Drive.....	17
4.2 Solar Array Modal Contribution	19
4.3 High Gain Antenna Drive.....	20
4.4 HRDI and MLS	21

5. Orbital and Configuration Influences on Spacecraft Dynamic Response.....	23
5.1 Jitter Amplitude Variation with Tip Inertia Rotation.....	23
5.2 Appendage Modal Variation with Tip Inertia Rotation.....	24
5.3 Disturbance Transmission Variation with Appendage Rotation	26
5.4 Thermal Elastic Bending Analysis	27
Concluding Remarks.....	30
Acknowledgments	32
Appendage 1: Modal Variation with Tip Inertia Rotation	35
Appendage 2: UARS Disturbance Experiment.....	40
Appendage 3: UARS Payload Interaction Experiment.....	43
Tables	50
Figures	43

Nomenclature

A	Plant matrix
B	Control influence matrix
C	Output matrix
CLAES	Cryogen Limb Array Etalon Spectrometer
E	Beam modulus of elasticity
HALOE	Halogen Occultation Experiment
HGA	High Gain Antenna
HRDI	High Resolution Doppler Imager
I	Beam area moment of inertia
I_r, I_p, I_y	Space platform roll, pitch and yaw inertia
I_{ip}	Free-Free beam rotational tip inertia
IM	Instrument Module
ISAMS	Improved Stratospheric and Mesospheric Sounder
ℓ	Beam length
m_{ip}	Free-Free beam tip mass
MLS	Microwave Limb Sounder
N_{HD}	Harmonic drive speed reduction ratio
N_{SG}	Spur gear speed reduction ratio
SSPP	Solar Stellar Pointing Platform
t	Time
U	Control torque input matrix
UARS	Upper Atmosphere Research Satellite
WINDII	Wind Imaging Interferometer
X	First-Order state vector
Y	Output vector
ZEPS	Zenith Energetic Particle System
α	Proportionality constant
β	Complement of the angle between the orbit normal and the Earth-to-Sun vector ($^\circ$)
$\Gamma(\mathbf{X}, t)$	Mode shape matrix
θ	Vibration amplitude
$\dot{\theta}$	Payload rotational speed ($^\circ/s$)
θ_{max}	Maximum vibration amplitude
θ_{min}	Minimum vibration amplitude
λ	Root of characteristic equation normalized by beam length, ℓ
$\lambda_n \ell$	Root of characteristic equation for n th mode
ρ	Beam mass/unit length
$\phi(x)$	Shape function
ω	Natural frequency
ω_{HD}	Harmonic drive output frequency (Hz)
ω_n	Natural frequency of n th mode
ω_0	Space platform orbital velocity

1. Introduction

On September 12, 1991, NASA launched the Upper Atmosphere Research Satellite (UARS)^{1, 2}. The goal of UARS was to carry out the first systematic, comprehensive study of the stratosphere and to furnish new data on the mesosphere and thermosphere. UARS provided critical data on the chemical composition of the upper atmosphere, particularly the structure of the Earth's protective ozone layer in the stratosphere. This satellite mission was the first element of a long-term national program to study global atmospheric change.

In addition to its atmospheric sciences mission, data from the first 737 days past the launch of UARS was used to investigate in-flight spacecraft dynamics. Figs. 1 and 2 show the spacecraft in pre-launch and operating configurations, respectively. Although the UARS spacecraft was used in this study, identification and measurement of spacecraft disturbances and their respective response can be used to increase the accuracy of pre-launch predictions on many spacecraft¹⁻¹⁰. Furthermore, as instrument pointing requirements become more demanding, spacecraft disturbances that were previously unimportant are becoming limiting factors in the quality of science data. The investigation included two in-flight experiments (approximately three-orbit each) using UARS.

Objectives of the first experiment were to isolate all disturbances known before launch, create disturbance combinations, create spacecraft dynamic responses suitable for system identification, examine spacecraft quiescence and identify any disturbances not known before launch. A primary goal of the experiment was to determine how each instrument and subsystem disturbance contributed to the overall spacecraft dynamic response. The first experiment was conducted during the last four hours of May 1, 1992 (233rd day after launch, Greenwich Mean Time), five hours after the spacecraft had rotated 180 degrees about its yaw axis. Analysis of flight data before the experiment indicated that the solar array edgewise and flatwise modes were constantly excited. Prelaunch analysis indicated that the Microwave Limb Sounder (Fig. 1) antenna limb viewing scan profile was the excitation source. Thus, the experiment provided a means to identify the solar array excitation source.

Examination of data from the first experiment lead to the conclusion that the solar array drive was the dominant disturbance source. Prelaunch analysis had predicted that any disturbance produced by the solar array drive was negligible. Furthermore, the data from the first experiment provided cases to examine payload-payload interaction. The second experiment was conducted on September 17, 1993 from 1300 through 1705 (737th day after launch, Greenwich Mean Time). Part of second experiment was conducted during the spacecraft yaw maneuver to examine spacecraft dynamics when the solar array was stationary.

The objectives of the second experiment were the same as those of the first. However, the second experiment focused more on payload-payload interaction and examining the dynamic response due to the instruments and subsystems without the influence of the solar array drive.

Flight data from the first 737 days after the launch was also analyzed to determine the orbital effects and spacecraft configuration effects on the spacecraft dynamic response. Orbital influences were due to temperature variation from crossing the Earth's terminator and variation of the solar incident energy as the orbit precessed^{11, 12}. Configuration influences were due to solar array rotation. The rotation changed spacecraft modal properties and the amount of solar energy incident upon the solar array. During the terminator crossing, the rapid ambient temperature change caused the spacecraft's two flexible appendages to experience thermal elastic bending (thermal snap). The resulting response was dependent upon the orientation of the solar array and the solar incident energy. Orbital influences were also caused by on-board and environmental disturbances and spacecraft configuration changes (due to solar array rotation) resulting in dynamic responses which were repeated each orbit.

The UARS solar array rotated about an axis parallel to the spacecraft's pitch axis at a rotation rate which results in a complete revolution for each orbit. The solar array rotation was dynamically equivalent to the solar array being stationary and the spacecraft rotating about the solar array drive shaft. The UARS yaw inertia was significantly higher than the roll inertia. During rotations, the inertia at the drive shaft (tip inertia) would vary from the roll inertia to the yaw inertia. The tip inertia, the modal properties of the solar array and the response amplitude varied harmonically at twice the orbital frequency. Three effects were observed. The first effect was that when the disturbances remained constant, the vibration amplitude varied inversely with the tip inertia¹³. A second effect was that variations of the tip inertia (boundary conditions) produced corresponding changes in the solar array frequencies of vibration and mode shapes¹³. A third effect that occurred due to the rotation of a flexible appendage was the variation of disturbance transmission resulting from the changing orientation of mode shapes¹³.

This paper presents analysis results from the experiments and flight data of the first 737 days after launch. Following an overview of the spacecraft, results are presented which show solar array drive, solar array modal, high gain antenna drive and appendage thermal-elastic bending contribution to the spacecraft dynamic response. The paper then presents the effects of orbital and configuration variation on spacecraft dynamic response. Spacecraft jitter (the angular excursion of an instrument's line-of-sight in a reference time interval (such as a sampling time period)) amplitude variation with tip inertia rotation is presented. The influence of solar array rotation direction and the solar incident energy on jitter amplitude is presented afterwards. Next, the spacecraft modal variation with tip inertia rotation is presented. The inertia variation results in modal bands for the solar array edgewise and flatwise modes. Three subsystem disturbances have

frequencies which overlap the bands. The results of examining configuration and orbital variations on thermal bending of the solar array is presented next. The last section presents analysis of the disturbance transmission variation with appendage rotation. The results of studying the in-flight dynamics of the UARS have shown the significance of the effects of spacecraft inertia variations on the modal characteristics of flexible appendages and on spacecraft jitter. Furthermore, results of these analyses can be extended to spacecraft with similar dynamic characteristics such as the Mir and the International Space Station.

1.1 UARS In-Flight Dynamics Study Highlights

The following are a highlights from the UARS dynamic study:

- UARS Disturbance Experiment, May 1, 1992.
- UARS Payload-Interaction Experiment, September 17, 1993.
- Experimental investigation of in-flight disturbances
- Identification of thermal elastic bending of boom extension boom containing ZEPS instrument.
- Long term (600 day duration) analysis of solar array thermal bending
- Correlation of WINDII and HRDI wind measurements with UARS vibration
- Identification and analysis of payload-payload interaction and structure-payload interaction.
- Discovery of latitude specific vibration response produced by UARS solar array drive.
- Identification of the tracking and relay high gain antenna effects on spacecraft response.
- Analysis of solar array modal variations with rotation about drive shaft.
- Examination of reduction gear drive dynamic effects on spacecraft response.
- Development of sub-assembly methodology and architecture to model multi-payload spacecraft. Approach includes nonlinear dynamics.

1.2 Publications and Presentations

The following are journal, nonformal and conference publications resulting from the study of UARS in-flight dynamics:

1. S. E. Woodard, M. Garnek, J. D. Molnar and W. L. Grantham, "The Upper Atmosphere Research Satellite Jitter Study," *Flight Experiments Technical Interchange Meeting*, Monterey, CA, October 5-9, 1992.
2. Molnar, J. and Garnek, M., "UARS In-Flight Jitter Study for EOS," NASA CR 191419, Jan 1993.
3. A. J. Butterfield and S. E. Woodard, "Payload-Payload Interaction and Structure-Payload Interaction Observed on the Upper Atmosphere Research Satellite," *AAS/AIAA Astrodynamics Specialist Conference*, Victoria, British Columbia, Canada, August 16-19, 1993.
4. C. R. Larson, S. E. Woodard, L. Tischner, E. Tong, M. Schmidt, J. Cheng, E. Fujii, and S. Ghofranian, "Upper Atmosphere Research Satellite (UARS) Dynamic Analysis Design System (DADS) Control-Structures Interaction Simulation Development," *AIAA 33rd Aerospace Sciences Meeting and Exhibit*, Reno, NV, January 9-12, 1995, AIAA Paper No. 95-0622.
5. S. E. Woodard and A. Nagchaudhuri, "Application of the LMS and Filtered-X LMS Algorithm to Spacecraft Jitter Compensation," *Fifth Annual AAS/AIAA Space Flight Mechanics Conference*, AAS Paper No. 95-211, Albuquerque, NM, February 13-15, 1995.
6. A. J. Butterfield and S. E. Woodard, "Science Instrument and Structural Interactions Observed on the Upper Atmosphere Research Satellite," *Journal of Spacecraft and Rockets*, Vol. 33, No. 4, July-August 1996.
7. C. R. Larson, S. E. Woodard, L. Tischner, E. Tong, M. Schmidt, J. Cheng, E. Fujii, and S. Ghofranian, "Multipayload Modeling for the Upper Atmosphere Research Satellite," *Journal of Spacecraft and Rockets*, Vol. 33, No. 4, July-August 1996

8. S. E. Woodard, D. A. Gell, R. Lay, and R. Jarnot, "Experimental Investigation of Spacecraft In-Flight Disturbances and Dynamic Response," *Journal of Spacecraft and Rockets*, Vol. 34. No. 2, March-April 1997.
9. S. E. Woodard, R. Lay, R. Jarnot and D. Gell, "Measured Spacecraft Dynamic Effects on Atmospheric Science Instruments," 35th Aerospace Sciences Meeting, Reno, NV, Jan 6-9, 1997.
10. S. E. Woodard, R. Lay, R. Jarnot and D. Gell, "Measured Spacecraft Dynamic Effects on Atmospheric Science Instruments, submitted to the *IEEE Transactions on Geoscience and Remote Sensing*.
11. S. E. Woodard, "Orbital and Environmental Influences on Spacecraft Dynamic Response," submitted to *Journal of Guidance, Control and Dynamics*.
12. S. E. Woodard, "The Upper Atmosphere Research Satellite In-Flight Dynamics," NASA Technical Memorandum 110325.

2. UARS Overview

The UARS observatory, Figs. 1 and 2, included ten science instruments mounted on an instrument module which was affixed to a multimission modular spacecraft^{5, 6}. The modular spacecraft provided attitude control using the reaction wheel assembly; communication and data handling; electrical power distribution; and propulsion^{5,6,14}. A high gain antenna (HGA) provided forward and return communication links to the two Tracking and Data Relay Satellites (TDRS)^{5,6}. A Solar-Stellar Pointing Platform (SSPP) and six solar array panels on a single sail were also attached to the IM^{5,6}.

2.1 Science Measurement Characteristics

There were five types of measurements, Fig. 3, used on UARS. Emission measurements were performed by instruments mounted to the instrument module which were non-gimballed⁵. Thus, their line-of-sight pointing was entirely dependent upon the spacecraft attitude. Solar/Stellar pointing was done by the SSPP which pointed three instruments mounted on it to the sun for measurement⁵. It pointed to certain bright blue stable stars so that one of its instruments could compare solar ultraviolet output to that of the stellar targets. Thus, its line-of-sight pointing changed from the sun to the various stellar targets. Continuous periodic disturbances resulted from the High Resolution Doppler Imager^{3, 7} and the Microwave Limb Sounder which were limb viewing instruments that determined the altitude profiles of atmospheric parameters by repetitiously taking vertical scans of the atmosphere's limb. Similar to limb viewing, were measurements using the solar occultation technique. Disturbances from HALOE (Halogen Occultation Experiment) solar occultation measurements were relatively short in duration but required precise tracking of the sun³.

Particle environment monitoring was also performed on UARS. Some of the particle environment measurements were done by an instrument which was at the end of an elastically flexible instrument boom. In Table 1 are the placement (the ability to position a boresight to a predefined pointing direction), knowledge (the definitive (after-the-fact) determination of the instrument boresight pointing direction), long term stability (the maximum excursion of a boresight over a given time period), and short term stability (jitter) requirements for all instruments⁴. One arc-s of roll displacement results in 0.0124 km displacement in the atmospheric limb. These pointing requirements were determined by each instrument's respective principal investigator based upon instrument characteristics and the physical parameter being measured. The Wind Imaging Interferometer (WINDII) had the most stringent pointing requirement of 4 arc-s per 2 s window about the roll axis (axis of least inertia)^{4,7,8}.

2.2 Disturbances Known Before Launch

Six of the UARS instruments and subsystems were gimballed. During the course of an orbit many disturbances were imparted to the platform which included impulses and periodic disturbances^{3, 7-12}. The satellite had two elastically flexible appendages (the solar array and an instrument boom) which were excited by multiple disturbance sources on-board the spacecraft. In Table 2 are descriptions of disturbances known before launch which have a measurable impact on spacecraft jitter. Many of these disturbances were triggered by the spacecraft's position in orbit such as thermal snap of the solar array as the spacecraft passed through the Earth's terminator (Refs. 7, 11 and 12) or HALOE events during orbital sunrise and sunset (Refs. 3 and 7). Some were due to UARS relative position to other spacecraft such as the line-of-sight of the high gain antenna to the Tracking and Data Relay Satellites (East and West) in geostationary orbits^{5, 6}. Other disturbances which were assumed to be negligible are due to internal mechanisms of the UARS's science instruments and subsystems. After launch, it was determined through observation and correlation of flight data that the combined dynamics of the solar array and solar array drive; and the high gain antenna drive dynamics during tracking and rewinding are major disturbance sources of continuous spacecraft jitter.

2.3 Attitude Determination

UARS' attitude determination and control subsystem had numerous sensors on-board for attitude determination^{5, 6, 14}. These included an earth sensor assembly module. Fixed-Head star trackers and an inertial reference unit. However, due to limitations in either sampling rate or resolution, the only means of measuring attitude suitable for studying jitter was with the inertial reference unit gyros at the aft end of the spacecraft. These gyros had a resolution of 0.05 arc-sec with a sampling rate of 7.8125 Hz.

2.4 Spacecraft Physical Characteristics

Design and analysis concerns for multi-payload spacecraft included identifying any adverse payload-payload interaction or structure-payload interaction. Such interactions were dominated by the gimballed instrument and subsystem inertia, payload motion profiles, gimbal location, gimballed payload center of mass relative to gimbal location; spacecraft mass and inertia; the modal properties of the primary structure and flexible appendages; torque profiles inputted at the gimbal drive shafts; and, attitude control system bandwidth and roll-off relative to appendage motion frequency. The inertia ratios for the gimballed instruments and subsystems to the spacecraft roll, pitch, and yaw inertia are given in Table 3 (Ref. 10). This ratio was a critical parameter to the overall contribution of each instrument to spacecraft jitter.

Structural frequencies, subsystem operating frequencies, and gimballed science instruments frequencies below 4.0 Hz (the Nyquist frequency for the rate gyros is 3.90625 Hz)^{3, 7, 14} are shown in Fig. 4. The structural frequencies are listed in Table 5 for various solar array positions. In Table 4, are the stiffness properties for the deployed appendages. The attitude control system had a bandwidth of 0.07 rad/sec with a roll-off of 36 dB per decade^{6, 16}. Disturbances due to rewind of the Microwave Limb Sounder antenna were partially attenuated by the attitude control system. A band represents the structural frequencies for the first two solar array modes. The structural frequencies of the modes varied as the solar array rotated through a complete revolution^{7, 8, 13}. During this rotation, the frequencies crossed. Harmonic drive output frequencies for the SSPP, solar array drive, and the high gain antenna during their tracking were also within the frequency band of the solar array. During separate parts of an orbit, the subsystems with harmonic drives will resonated both the solar array flatwise and edgewise modes.

3. Typical UARS Orbital Dynamics

The complexity of UARS as a science platform and how the science measurement and subsystem events affect the motion of the spacecraft can be understood by examining the events of one orbit. Fig. 5 illustrates all events which imparted disturbances to the satellite during the first orbit of January 28, 1992. These events are described in Table 6. During this orbit (first orbit of the day) all UARS instruments and subsystems were operating nominally. The data and analysis will give spacecraft control-structure designers and researchers an understanding of in-flight disturbance events and their effect on spacecraft jitter. The Microwave Limb Sounder (MLS) and the High Resolution Doppler Imager (HRDI) imparted continuous repetitious disturbances to the spacecraft throughout the orbit.

Analysis of flight-data for the first orbit of January 28, 1992 (the 139th day past launch) is presented in this section. During this time, the UARS instruments and subsystems which were examined were all functioning nominally. The events shown for this day are typical with the minor exception that instrument scanning patterns are changed throughout the life of the spacecraft to improve measurements; adjust for seasonal variations in the atmosphere; and, to focus more on a particular atmospheric constituent. This section will first present time histories of the UARS subsystems (HGA, solar array, reaction wheels) followed by similar time histories of the instruments. Along with these time histories, will be descriptions of their pointing requirements and reference orientations. Rate gyro data will be presented next, followed by analysis of the data. The time histories are for the orbit whose events were presented in Fig. 5. These events are listed and numbered sequentially in Table 6.

3.1 UARS Subsystems

3.1.1 Modular Attitude Control System

The Modular Attitude Control System (MACS) maintained an Earth pointed orientation to accuracy of ± 108 arcsec per axis using four reaction wheels^{4, 5, 6, 7, 9, 10}. Three wheels were mounted orthogonally such that their axes were parallel to spacecraft the axes. A fourth wheel was mounted such that its rotation axis was skewed 54.74 degrees to the other three. Attitude knowledge was maintained to ± 60 arcsec per axis. In the normal control mode, a constant bias momentum was maintained on the skewed wheel to preclude the roll and yaw wheels from crossing zero speed. The normal mode controller for the UARS MACS used a regulator-type control law with a commanded torque whose magnitude was the accumulative sum of scaling position, position-integral, position-integral's integral, and position-derivative (PIID). The controller bandwidth was 0.07 rad/sec. Control law was executed and the wheel drive commands were sent every 0.512 sec. The time history of the MACS wheel torques for the first orbit of January 28, 1992 were shown in Fig. 6. Because the skewed wheel was maintained at a constant 50 N-m, the roll and yaw wheel did not have to cross zero (thus reducing attitude transients). Reaction wheels produced disturbances when they had a sudden change in rotational speed or imbalance. Many of these disturbances were due to the instruments slewing speed changing. Disturbance events listed in Table 6 are annotated on Fig. 6.

3.1.2 Inertial Reference Unit Gyros

Inputs to the MACS were measurements from the inertial reference unit rate gyros. All gyros had a bandwidth of approximately 2.0 Hz (-6db)^{4, 5, 7, 9, 10}. Gyro data was sampled every 0.128 sec. The measurements taken were the number of counts (0.05 arcsec per count) since the last sample. A digital inertial reference unit prefilter provided protection from structural resonant frequencies being aliased within the control bandwidth. Normally, the prefilter was only used in the orbit adjust mode. Other attitude measurements included two Earth sensors, three course sun sensors, a fine sun sensor, and fixed head star tracker. These sensors did not have the sampling frequency and resolution suitable for this study.

UARS inertial reference unit rate gyros were the most useful measurement source for this study. In Fig. 7 are time histories of the roll, pitch and yaw gyro counts. The solar array thermal snaps were the most pronounced events recorded with the inertial reference unit. These occurred due to the rapidly changing thermal conditions of the solar array as it crossed the Earth's penumbra. This is illustrated in Fig. 8. The pitch gyro data also shows orbital as well as attitudinal trends. Because most of the orbital motion was

resolved to the pitch axis (local vertical), the on-board computer subtracted out the orbital rate. This prevented the pitch gyro counter from constantly restarting. However, some residue of the orbital motion remained. All gyros had a very low rate/trend bias. The orbital motion and bias were more readily seen once the gyro data had been integrated, Fig. 9, to give position. By using sliding jitter windows of 2 seconds, the orbital motion and biases in yaw and roll were eliminated. Jitter was determined by taking the absolute value of the difference between the minimum and maximum position values within the window. The window was slid through the entire time history. The pitch axis still contained the residue of the orbital motion. The subsequent sliding 2 second jitter windows were sufficient for this study. Furthermore, larger jitter windows can be derived from combining the two second windows.

3.1.3 Solar Array

UARS orbits began with the spacecraft crossing the ascending node of its orbit. However, in this study, the solar array zero position was used as a means of referencing the beginning of an orbit because many of the dynamics observed in this study were correlated with the solar array position. The solar array had seven rotation rates, $-3 \omega_0$, $-2 \omega_0$, $-1 \omega_0$, 0 , $1 \omega_0$, $2 \omega_0$, and $3 \omega_0$ (where ω_0 was the nominal orbital angular velocity). The solar array had both an open loop and closed loop mode of operation^{5, 6}. Normally, it operated open loop. The solar array orientations for various positions were illustrated in Fig. 10. The encoder measured the relative position of the solar array with respect to the spacecraft axes (Fig. 10). The forward direction of rotation was defined as the direction the solar array was rotating when the spacecraft was flying in the forward direction. The spacecraft periodically (approx. every 36 days) changed its direction of flight (180 degree yaw maneuver) to prevent solar array energy collection and solar heating of payloads from becoming a problem. The time history of the solar array rotation for the first orbit of January 28, 1992 is shown in Fig. 11. The solar array was rotating in the forward direction.

3.1.4 High Gain Antenna

UARS high gain antenna was a two-axes gimbal driven parabolic antenna. The two gimbals were controlled by the high gain antenna gimbal drive electronics which used regulator-type (proportional, integral, and derivative) control. Both the UARS on-board computer and ground station could be used as a source for commands^{5, 6}. The outboard axis, alpha, was nominally parallel to the spacecraft pitch axis, Y . Inboard and perpendicular to the alpha axis was the beta axis. With respect to the spacecraft coordinate system, alpha and beta were defined as:

$$\alpha = \arctan \frac{X}{Y} \tag{3.1}$$

and

$$\beta = \arctan \frac{-Y}{\sqrt{X^2 + Z^2}} \tag{3.2}$$

When α and β are both zero, the high gain antenna coordinate system is co-aligned to the spacecraft coordinate system and the high gain antenna is oriented toward the Earth (+Z Ref. 6). The +X is in the direction of flight. The antenna alternated between tracking the Tracking and Data Relay Satellite (TDRS) - East (when UARS was over the Earth's eastern hemisphere) and Tracking and Data Relay Satellite - West. Depending upon UARS orbital parameters, it completed tracking one TDRS, rewinded, waited for the other TDRS to appear beyond the orbital horizon, and then tracked the other TDRS; or, after completing tracking of one TDRS, it will rewinded and then tracked the other TDRS. Fig. 12 shows the time history of the antenna alpha and beta gimbals for the first orbit of January 28, 1992. The disturbance from the HGA which resulted in jitter was when the antenna changed its rotational speed (i.e. from tracking to rewinding). The resulting impulse was proportional to the speed change and gimballed inertia. Vibration amplitudes and frequencies of the spacecraft depended upon the impulse magnitude, point and direction of application, the transmission of the impulse to the various mode shapes of the flexible appendages and modal parameters for the modes shapes such as damping, stiffness, and inertia.

3.1.5 Solar Stellar Pointing Platform

The Solar Stellar Pointing Platform was a two-axes gimbal driven payload mount which pointed the three instruments mounted on it to either the sun or selected stars. The two gimbals were controlled by the SSPP gimbal drive electronics which used regulator-type control which was similar to the high gain antenna. The UARS on-board computer was used as a source for commands^{5,6}. Its alpha and beta gimbal axes had the same orientation to the spacecraft as the high gain antenna with the alpha gimbal outboard of the beta gimbal. The time history of the SSPP alpha and beta gimbals for the first orbit of January 28, 1992 are shown in Fig. 13. Similar to the high gain antenna, the disturbances from the SSPP which resulted in jitter was when the SSPP changed its rotational speed.

3.2 Instruments

3.2.1 Halogen Occultation Experiment

The Halogen Occultation Experiment (HALOE) was mounted amidship on UARS near the High Resolution Doppler Imager (HRDI) instrument. Its objective was to measure the vertical distribution of O₃, HCl, HF, NO, CH₄, H₂O and NO₂ and the atmospheric pressure profile. HALOE used the solar occultation technique (Fig. 3). As the Sun-spacecraft line-of-sight transversed the Earth's atmospheric limb during satellite sunrise and sunset events, chemical species in the atmosphere which absorb infrared energy in well defined wavelength bands were measured by HALOE. Because the sun was used as a background light source, the instrument's instantaneous field of view (IFOV) had to be maintained during calibration and measurements. A stepper-motor-driven biaxial gimbal system, fine and coarse sun sensors, and microprocessor-based closed-loop feedback sun tracking control logic were used to maintain the IFOV. The biaxial gimbal assembly (BGA) contained independently controlled gimbals with a $\pm 185^\circ$ azimuth range and a 39° elevation range. Coarse and fine sun sensors provided error signals to the control algorithm.

HALOE alternated between sunrise and sunset scanning sequences. In Fig. 14 are shown the elevation gimbal angle histories during the above mentioned events. Orbital motion was accommodated by the control law operation every 0.128 sec. The degree of orbital motion compensation varied with the angle formed by the sun-spacecraft line-of-sight and the spacecraft's velocity vector. Because orbital motion was constant, stepping of the HALOE gimbal generated a disturbance at 7.8125 Hz. This disturbance to the platform was unimpeded due to the bandwidth (0.01 Hz) of the UARS attitude control system and affected the line-of-sight pointing of all science payloads.

3.2.2 High Resolution Doppler Imager

The High Resolution Doppler Imager was mounted amidship on UARS. HRDI observed the Doppler shifts of spectral lines within the spectral band of molecular oxygen. These shifts were measured in two different directions, yielding two components of the wind velocity relative to the spacecraft⁵. A triple-etalon Fabry-Perot interferometer served as a high resolution spectral filter to reject continuous emissions outside the desired absorption lines. The interferometer was mounted to a two-axes gimballed telescope whose motion was controlled by a microprocessor. HRDI measured Doppler shifts by performing a vertical altitude scan in the direction forward of the spacecraft's velocity. The telescope was then rotated 90 degrees and a second vertical altitude scan was performed. The sequence of measurements yielded two measurements of the same

region of the atmosphere in a time interval which was relatively short compared to the characteristic time scales for changes in the wind field. HRDI had an open-loop scan profile for the day and a different open-loop scan profile for the night part of the orbit which are shown in Fig. 15

In Figs. 16 and 17 are shown the effect of the attitude control system on accommodating the HRDI scans. When HRDI started its night scan, the attitude control system had no influence on how its motion effected the spacecraft. During the HRDI day scan, the frequency was low enough that the attitude control system had some effect on the subsequent motion of the spacecraft. The HRDI telescope had a smaller inertia ratio than the other instruments but its scanning frequency during the night portion of an orbit had significant effect on the spacecraft motion. The inertia ratio between the gimballed instruments and subsystems to the spacecraft inertia is given in Table 3. The inertia ratio had a significant effect on how much subsequent motion the spacecraft had due to the motion of the instruments. This was due to the same torque being applied to the payload and to the spacecraft but in an opposite sense. The subsequent motion of the payload and the spacecraft was proportional to their respective inertia resolved to the gimbal drive shaft. Observed, Fig. 16, on UARS was a switching of scanning profiles of the High Resolution Doppler Imager and the corresponding yaw angular position of UARS. UARS attitude control system had a control bandwidth of 0.01 Hz. Before 3420, the scanning pattern had a frequency of 0.083 Hz and amplitude of 74 deg. After 3420 seconds, HRDI had a scanning frequency of 0.0067 Hz and amplitude of 51 deg. The HRDI azimuth gimbal history and the resulting yaw motion are shown in Fig. 17. It is readily apparent that the effect of the attitude control system on jitter was to attenuate rigid-body motion if it was within the controller bandwidth or roll-off.

3.2.3 Microwave Limb Sounder

The Microwave Limb Sounder (MLS) had two gimballed parts. The antenna stepping history and the switching mirror position history for a complete orbit are shown in Fig. 18 (Ref. 5). An microwave antenna scanned the vertical profile of the atmosphere. The scan cycle of 65.5 seconds consisted of a forward limb viewing trace followed by a rewind. At the beginning and end of an orbit, the antenna steps were adjusted to account for the Earth's oblateness. A switching mirror was synched with the antenna and moved through three positions: an internal calibration target; a zero-reference space view; and the atmospheric signal from the antenna system (limb). The inertia ratio for MLS was far higher than that of HRDI but the attitude control system had more influence on the subsequent MLS motion as compared with what it had with on HRDI night scan. The motion profile of the MLS and the motion of the spacecraft about its roll axis are shown in Fig. 19. The MLS antenna scanning frequency was 0.015 Hz. Similar to

the HRDI day scan, the attitude control system attenuated the subsequent rigid-body motion due to the antenna motion.

3.3 Elastically Flexible-Body Motion

The flexible appendages of UARS which had structural resonance frequencies within the Nyquist frequency of the rate gyros were the extension boom for the Zenith Energetic Particle System instrument and the solar array. Before launch, the primary known excitations of these appendages were impulses due to instrument change in motion. All pre-launch analysis was performed using a structural finite element model of the UARS spacecraft. The flexible appendages of the spacecraft could each be considered as a free-free beam with a tip mass and tip inertia due to the spacecraft. Ref. 16 has shown that such a consideration will allow one to predict variations of modal properties as one changes boundary conditions. In the case of the UARS appendages, the changes were due to solar array edgewise and flatwise modes transverse vibration. During solar array rotation, the tip inertia of the array (the spacecraft) varies. Thus, in one configuration the transverse vibration for one mode had the spacecraft yaw inertia as its tip inertia. As the solar array rotated through 90° , the same mode had the roll inertia as its tip boundary condition. Because the yaw inertia was triple that of the roll inertia, the finite element analysis of the solar array modes resulted in 18.7 % variation in the solar array 1st bending mode and a 19.4 % variation in the solar array 1st bending edgewise mode. The variation of these two modes with the solar array position is depicted in Fig. 20. The small difference in frequency between 90° and 180° is because the solar array center of gravity is offset from its rotational axis. The fixed appendages such as the Zenith Energetic Particle System boom had its modal properties vary because as the solar array rotates, it changed the overall system inertia.

Tables 7 through 9 are the result of performing power spectral density analysis at various solar array positions using the in-flight roll, pitch and yaw gyro data. At each position, the dominant frequencies from the PSDs are listed in descending order. Since the gyros are collocated, one could not determine the mode shape associated with each frequency. Thus it was very difficult to conclusively identify the modes of vibration. Examination of the two solar array modes near .25 Hz does indicated that their values did varied with solar array position. However, identifying which mode was the flatwise and which was the edgewise cannot be achieved using only gyro measurements. Vibration about the roll gyro was dominated by the .94 Hz mode during most of the orbit. Similarly, the 2.93 Hz mode dominated the vibration about the yaw axis. The vibration about the pitch axis was dominated by the .94 Hz mode also and one or both of the 0.25 Hz solar array modes. In Tables 8 and 9, are shown the frequencies of 0.085 Hz for solar array positions of 90° , through 180° which were due to the night scan of HRDI instrument. Although most of the tabulated frequencies were in proximity to the values derived from finite element analysis, some could

not be attributed to any known pre launch prediction such as the .40 and .57 Hz modes about the yaw axis; the .33 Hz modes about roll at 45° and 135° ; and, the 0.0363 Hz found about roll and yaw at 0° .

The jitter response was the result of all rigid-body motion and vibratory motion of the flexible elastic appendages imparted to the main platform. In Fig. 21, the jitter response for roll, pitch, and yaw are shown. Disturbance events are annotated, Table 6, on the jitter time histories. During the entire orbit, the Microwave Limb Sounder (MLS) instrument was constantly scanning. The High Resolution Doppler (HRDI) instrument was also constantly scanning but used two scan profiles for orbital day and night (events 2 and 15 were the transitions.) Sunset and sunrise thermal snaps resulted in the most prominent jitter responses. Impulses due to the instruments and subsystems were proportional to the inertia of the payloads and how much the slew rate and direction had changed. The flexible modes excitation will depend upon the orientation of the appendage and the axis about which the instrument moved. All events produced a noticeable change in the jitter response of one or more gyros. The rewind of the MLS antenna appeared as 65 s lobes on the roll jitter response.

The pitch gyro accommodated the changes in pitch attitude as well as the orbital motion in an inertial frame of reference. As a means of keeping the gyro from constantly having to restart its counter, the orbital rate was subtracted from the pitch gyro measurements using UARS on-board computer. The harmonic variation in the pitch response was the residue orbital motion which was not subtracted out. The jitter response was due to all the numbered events and the continuous disturbances due to HRDI and MLS.

The spectral histories for the roll axis are depicted in Figs. 22 and 23. Disturbances are also annotated for the spectral densities. All spectral analyses were normalized to the peak value for each analysis. The Figs. illustrate that during the entire orbit, the energy level that the modes have was varying. The 0.25 Hz modes were constantly excited for the entire orbit. Modes near 1.0 Hz were excited during most of the orbit. However, neither the 0.25 Hz nor the 1.0 Hz modes were constantly dominant mode (Table 7). There were periods during the orbit where modes were excited but there was no known disturbances such as between events 15 and 16 (Table 6).

4.0 Subsystem and Instrument Contribution to Space Dynamic Response

4.1 Solar Array Drive

One of the first results from the May 1 experiment was the unexpected vibration level of the edgewise and flatwise modes and the five-minute beats dominating roll and yaw responses. The Wind Imaging Interferometer science instrument on UARS had a roll and yaw jitter requirement of 4 arc-s/ 2 s (i.e., 4 arc-s during a 2 s window) which was the minimum spacecraft jitter requirement. All jitter time histories in this paper used a 2 s window duration. Figs. 24 and 25 (from the May 1, 1992 experiment) show the roll and yaw jitter response during the ascending part of two orbits in the experiment. During the approximately 34-minute period (78973-81000 s past start of day) when all major disturbances known before launch were quiescent, roll jitter exceeded 15.0 arc-s/ 2 s and yaw jitter exceeded 6.0 arc-s/2 s (Figs. 4b and 5b). Figs. 24 and 25 also show repeated 5-minute (approximately) beats for roll and yaw. Furthermore, power spectral density frequency analysis indicated strong excitation of the solar array fundamental flatwise and edgewise modes.

The figures also show the response with respect to spacecraft latitude and solar array position. Because the solar array rotated once per orbit, any anomalies it experienced which were specific to a particular solar array position would also be specific to a particular latitude in orbit. Many of the jitter peaks occurred during approximately the same latitudes in orbit. The response for two orbits is shown to demonstrate that the jitter anomalies occur every orbit. The roll jitter response (Fig. 24) had two distinct beats at approximately 20° S and 20° N. In both orbits, the jitter exceeded 15 arc-s. The smaller 5-minute beats that came before and after the two major beats were also repeated. The yaw jitter response (Fig. 25) had three distinctive beats at approximately 20° S, 2° S and 20° N. During most of the yaw jitter beats, the 4 arc-s/ 2 s jitter requirement was exceeded. None of the anomalies were due to thermal snap of the solar array which occurred during the descending part of the orbit.

Fig. 26 shows mapping of points on UARS' ground track that exceeded certain jitter level thresholds. These mappings used 15 hours of flight data from the 133rd day past launch (January 22, 1992). Data from this day was not part of the experiment. On January 22, 1992, the solar array was rotating in the forward direction. During the May 1, 1992 experiment, the solar array was rotating in the reverse direction. Thresholds are 4 arc-s/2 s (minimum jitter requirement), Fig. 26a, and 10 arc-s/2 s, Fig. 26b. From Fig. 26, it can be seen that the jitter exceeded the thresholds only at certain latitudes. The 10 arc-s/2 s roll jitter threshold, Fig. 26b, was exceeded at latitudes of 57° S (sunrise thermal snap), 46° N (sunset thermal snap), 10° S, and 38° S.

Analysis of Figs. 24 through 26 showed that the jitter response was latitude specific with different response characteristics for forward and backward rotation of the solar array. The dominant trends in the jitter patterns were independent of any subsystem or instrument dynamics but varied with solar array position. The correlation of jitter to solar array position was constant. However, the correlation of jitter to groundtrack latitude was valid for short term (approximately one day) due to the precession of the orbit. The link between the spacecraft jitter and spacecraft latitude is warranted because many of the science measurements were referenced to latitude. If the measured jitter levels exceeded instrument pointing requirements consistently for certain latitudes, then the impact of the excessive jitter could result in science measurement anomalies being incorrectly attributed to atmospheric phenomena. The latitude of the false measurement anomalies also precessed with orbit. Ref. 15 has presented case studies which demonstrated the impact of excessive jitter on science measurements. The aforementioned findings refocused the efforts of the investigation to identify and analyze the excitation source.

On June 2, 1992 (day 265 past launch), after the spacecraft yaw maneuver immediately following the May 1, 1992 experiment, the solar array stopped rotating unexpectedly. It also started rotating approximately 50 minutes afterward without any commands being given. Figs. 27 and 28 (from June 2, 1992 flight data) show the solar array position and the spacecraft roll displacement as the solar array stopped and as it started again, respectively. Before stopping at approximately 72950 s, the roll gyro measured attitude displacements which exceeded 1.0 arc-s during the 0.128s sampling intervals. The significant reduction in jitter when the solar array stopped rotating validated the conclusion that the solar array drive was the source of jitter. When the solar array started rotating again, the impulse resulted in roll attitude displacements in excess of 1.2 arc-s during the 0.128s sampling intervals. Furthermore, the roll displacement exceeded levels of 0.5 arc-s 50 s after the impulse. The prime contractor for the UARS, General Electric, investigated the cause of the anomaly. They found that the solar array drive stepper motor output, which had 23 pulses/s, transmitted through the harmonic drive, which had a 100:1 reduction ratio, produced a harmonic drive output of 0.23 pulses/s. The harmonic drive output frequency resonated the solar array edgewise and flatwise modes. Stopping the solar array eliminated the excitation source. The reduction in vibration also reduced the solar array flexing being transmitted back to the gear drive.

Ref. 8 had measured the free-decay damping of the spacecraft response to the solar array stopping to be 2.8% and had attributed this damping to the solar array edgewise mode of vibration. However, the friction in the gear drive was the probable cause of the high damping ratio. Because the edgewise mode of vibration was constrained by the gear drive, all of these damping effects would have significantly attenuated structural vibration of the solar array edgewise mode. Furthermore, when the gear drive clutch was locked and other disturbances were active, there was no high value of damping observed for the solar array flatwise and

edgewise modes. The damping effect of the gear drive countered the resonating effect of the solar array harmonic drive output. Friction in the gear drive attenuated energy placed into the solar array at the resonant frequency by the harmonic drive. The result was that the solar array had large but bounded levels of vibration. Therefore, any catastrophic damage to the solar array drive was prevented. However, the excessive flexing of the solar array transmitted through the gear drive could reduce the life of the drive.

4.2 Solar Array Modal Contribution

The two fundamental solar array modes of vibration dominated the spacecraft motion response. An objective of this investigation was to determine which mode had a larger contribution to the response. Because the only sensors suitable for this study (in terms of frequency and resolution) were the spacecraft gyros, vibration modes could not be identified from measurements alone. To determine which solar array mode dominated the response, the following reasoning was used. Although the solar array harmonic drive output frequency (0.23 Hz) was near the resonant frequencies of the solar array flatwise and edgewise modes (0.2 to 0.3 Hz), the solar array harmonic drive torque output was almost orthogonal to the flatwise mode but not with the edgewise mode. Since the modes are nearly mutually orthogonal, one can examine the response for the roll and yaw axis at the solar array positions which are 90° apart.

When the solar array was at the 180° or 360° position, the flatwise mode vibrated about the yaw axis and the edgewise mode vibrated about the roll axis (Figs. 24 and 25). At the 270° position, the flatwise mode vibrated about the roll axis and the edgewise mode vibrated about the yaw axis. If the flatwise mode dominated the response, one should expect to see a roll amplitude higher at the 270° position than at the 180° and 360° positions. Similarly, if the edgewise mode dominated the response, one should expect to see a yaw amplitude higher at the 270° position than at the 180° and 360° positions. At approximately 240° and 300°, both modes contributed to the roll and yaw jitter response which resulted in the higher amplitudes. The roll jitter amplitude was higher at the 180° and 360° positions than it was at the 270° position. Yaw jitter amplitude was higher at the 270° position than it was at the 180° and 360° positions. Therefore, one can infer that the edgewise mode was the dominant mode of vibration.

4.3 High Gain Antenna Drive

Flight data revealed that the high gain antenna experienced stiction (static friction) as shown in Fig. 29. At approximately 4720 s, the discontinuity in the periodic wave form was caused by the antenna overcoming static friction. Overcoming the stiction produced an impulse and subsequent roll jitter response of 0.8 arc-s. In addition to the stiction, the high gain antenna harmonic drive was also a disturbance source. Because of the June 2, 1992 solar array anomaly, the solar array was placed in an active control mode and then its rotation was stopped such that it would maximize solar incidence while stationary. It remained in this position for 42 days. However, during this time, isolated high gain antenna disturbances were then observed and analyzed.

The harmonic drive output frequency, ω_{HD} (Hz), for a payload having a rotational speed of $\dot{\theta}$ ($^{\circ}/s$) was:

$$\omega_{HD} = \frac{2\dot{\theta}N_{HD}N_{SG}}{360} \quad (4.1)$$

where N_{HD} and N_{SG} were the speed reduction ratios for the harmonic drive and the spur gear, respectively. The above expression represented the case where the harmonic drive speed reduction preceded that of the spur gear. The solar array reduction ratios, N_{HD} and N_{SG} , were 100 and 6.81, respectively. The high gain antenna and the Solar/Stellar Pointing Platform reduction ratios, N_{HD} and N_{SG} , were 200 and 3.24, respectively. The Solar/Stellar Pointing Platform was a gimballed instrument containing three UARS science instruments. The solar array, the high gain antenna and Solar/Stellar Pointing Platform targeting/tracking rotational speeds of approximately 0.06 $^{\circ}/s$ produced harmonic drive output frequencies of 0.23 Hz, 0.22 Hz and 0.22 Hz, respectively. The output frequencies resonated the solar array flatwise and edgewise modes (Fig. 4). The high gain antenna positioning (rewind) rotational speed of 0.31 $^{\circ}/s$ produced a harmonic drive output frequency of 1.12 Hz which resonated modes 6 and 7 (Fig. 4).

The effect that the high gain antenna harmonic drive had on jitter is shown in Figs. 29 and 30 using data from the 266th day past launch (June 3, 1992). The high gain antenna was targeting one of the tracking data and relay satellite spacecraft from 4600 s (past start of day) to approximately 5350 s. Afterwards, it positioned itself for the other tracking data and relay satellite. From 4600 to 4800 s, the high gain antenna targeting maneuver was an isolated disturbance. Fig. 29 shows the time history of the time history of the high gain antenna alpha gimbal with the rotation removed (4600-4800 s) and roll jitter (4600-4800 s) while the high gain antenna was targeting a tracking data and relay satellite.

Frequency analysis is shown in Fig. 30 for the high gain antenna targeting and positioning maneuvers using roll and pitch gyro data. Figs. 30a and 30c show the power spectral density of the roll and pitch gyro data, respectively, during the targeting maneuver. The figures indicate that the harmonic drive on the high gain antenna was also an excitation source of the solar array edgewise and flatwise modes. Fig. 29b shows that the jitter was up to 1.0 arc-s/2 s during targeting. From 5600 to 5800 s, the only disturbance present was the high gain antenna during its positioning (rewind) maneuver. Figs. 30b and 30d show the power spectral of the roll and pitch gyro data, respectively, during the positioning maneuver. The modes excited by the positioning maneuver are annotated. During the positioning maneuver, the modes near approximately 0.7, 0.95 and 1.1 Hz were excited. Although 1 arc-s is small with respect to the UARS pointing requirement of 4 arc-s, the identification of the disturbance is important for future spacecraft because the response amplitude will be higher if the disturbance has a higher transmission to the solar array modes or if the spacecraft size is smaller.

4.4 HRDI and MLS

The contribution that the High Resolution Doppler Imager (HRDI) had on UARS dynamic response is shown in Fig. 31. Fig. 31a shows the time history of the HRDI azimuth gimbal during the transition from the HRDI day scan to the night scan. The HRDI telescope views the atmospheric limb on one side of the spacecraft then turns to view the limb on the other side. The frequency that it repeats this cycle is 0.083 Hz which is outside of the 0.01 Hz attitude control system bandwidth. The HRDI telescope/UARS yaw inertia ratio is 1.20×10^{-5} . The HRDI azimuth scans are about an axis axis parallel to the yaw axis. The motion of HRDI results in a “tail wagging the dog” effect which is shown in Fig. 31b.

Pre-launch analysis had predicted that the Microwave Limb Sounder (MLS) would produce the largest spacecraft jitter response (2.6 arc-s/(2 s) about the roll axis). The MLS/UARS roll inertia is 3.90×10^{-4} . The instrument had a scan profile that included 27 forward steps and 2 rewind steps. The total MLS antenna angular excursion is 1.32° . Fig. 32 shows the MLS antenna steps and the spacecraft roll jitter response for days 301 and 737. The spikes observed in Figs. 32a and 32d are due the MLS rewind. The peak roll jitter observed for both day 301 (Fig. 32b) and day 737 (Fig. 32d) was 2.6 arc-s/ (2 s). Roll jitter for the two days was examined to determine if there was any pronounced change in the dynamic response due to the complete outgassing of the cryogen from one of the science instruments. The cryogen completely outgassed on day 603. Although the spacecraft mass was reduced by 7%, there was no significant change in the roll jitter response.

5. Orbital and Configuration Influences on Spacecraft Dynamic Response

5.1 Jitter Amplitude Variation with Tip Inertia Rotation

UARS solar array positions are shown in Fig. 10. The orientation of the solar panels changed 360° each orbit. When the solar array vibrated, its vibration was imparted to the spacecraft and resulted in spacecraft vibration. Because of conservation of momentum, the vibration was scaled such that its maximum occurred when the tip (boundary) inertia was minimum and its minimum occurred when the tip inertia was maximum. The relation between the roll, I_r , and yaw inertia, I_y , (assuming $I_y > I_r$) is given¹⁶ by

$$I_y = \alpha I_r$$

with α as a proportionality constant. If the solar array was rotating at the orbital angular velocity, ω_o , then the tip inertia varied as:

$$I_{tip}(t) = \left(\frac{I_y + I_r}{2} \right) + \left(\frac{I_y - I_r}{2} \right) \sin(2\omega_o t) \quad (5.1)$$

and the corresponding vibration amplitude, $\theta(t)$, varied as

$$\theta(t) = \left(\frac{\theta_{max} + \theta_{min}}{2} \right) + \left(\frac{\theta_{max} - \theta_{min}}{2} \right) \cos(2\omega_o t) \quad (5.2)$$

When the disturbance source was the same, the vibration amplitude, $\theta(t)$, was dependent upon the tip inertia. By the time integral of conservation of momentum:

$$I_y \theta_{min} = I_r \theta_{max} \quad (5.3)$$

The variation of spacecraft median roll and yaw jitter (from day 233 past spacecraft launch) with solar array rotation is shown in Fig. 33. Results from Ref. 7 demonstrated that the solar array edgewise mode was the dominant mode of vibration. When the solar array was in the 90°/270° position, the edgewise mode vibrated about an axis parallel to the spacecraft yaw axis and the flatwise mode vibrated about the roll axis. When the solar array is in the 0°/180° position, the edgewise mode vibrates about an axis parallel to the spacecraft roll axis and the flatwise mode vibrates about the yaw axis. Therefore, the peaks for yaw and roll median jitter occurred at the 90°/270° and 0°/180° positions, respectively. Thus, analysis of Fig. 33 corroborates Eq. (5.1-5.3).

Fig. 34 shows the maximum and average roll jitter for days 128 through 737 past the launch of UARS. The effect of the solar array rotation direction is apparent. The average and maxima shown in Fig. 34 excluded jitter during the thermal bending of the solar array. Due to the precession of the orbit plane, the Beta angle swept out an angle of $\pm 80.45^\circ$ (Ref. 6). At large values of the Beta angle, solar array energy collection and sun impingement on the payloads became a problem. To alleviate the problem, the spacecraft was rotated 180° about its yaw axis approximately every 30-36 days. After each yaw maneuver, the direction of solar array rotation was changed. When the solar array was rotating in reversed direction, the jitter was higher than when the solar array was rotating in the forward direction as shown in Fig. 34. The UARS jitter requirement was 4 arc-s/2-s. The significance of this finding, Fig. 34, is that the requirement was violated more during days when the solar array was rotating in the reverse direction. Hence, the accuracy of science measurements which had to adhere to the 4 arc-s/2-s requirement varied approximately every other month.

Because the orbit plane precessed between yaw maneuvers, the tracking instruments varied their tracking trajectories correspondingly. The change in tracking trajectories produced a corresponding change in the spacecraft response. Fig. 35 shows the variation in spacecraft roll jitter with Beta angle for the same days used in Fig. 34. Jitter measurements during thermal bending of the solar array were also excluded from the results shown in Fig. 35. The dominant trend observed was that as the magnitude of the Beta angle increased, the roll jitter increased. However, the values in the reversed direction were higher than those in the forward direction of solar array rotation. It can be inferred from Fig. 35 that between yaw maneuvers, the jitter levels grew monotonically.

5.2 Appendage Modal Variation with Tip Inertia Rotation

One effect of variable spacecraft mass and inertia on appendage transverse vibration was the changing modal frequencies and mode shapes. Appendix 1 and Ref. 16 present a development and examination of the Euler beam equation with the appropriate boundary conditions which show short-term (orbital) periodic changes in modal characteristics when flexible appendages rotated and long-term effects due to mass expenditure (fuel and/or cryogen expenditures). The following characteristic equation for the Euler beam of length, ℓ , with tip mass, m_{tip} , and tip inertia, I_{tip} , resulting from Appendix 1 is

$$\begin{aligned}
& \lambda^4 [I - \cos(\lambda\ell) \cosh(\lambda\ell)] + \lambda \left(\frac{m_{tip} \omega^2}{EI} \right) [\sin(\lambda\ell) \cosh(\lambda\ell) - \cos(\lambda\ell) \sinh(\lambda\ell)] \\
& + \lambda^3 \left(\frac{I_{tip} \omega^2}{EI} \right) [\cos(\lambda\ell) \sinh(\lambda\ell) + \sin(\lambda\ell) \cosh(\lambda\ell)] + I_{tip} m_{tip} \left(\frac{\omega^2}{EI} \right)^2 [I + \cos(\lambda\ell) \cosh(\lambda\ell)] = 0
\end{aligned} \tag{5.4}$$

The beam was assumed to have mass/unit length, ρ , modulus of elasticity, E , cross sectional area, A , and area moment of inertia, I . The root of the characteristic equation normalized by beam length, ℓ , is λ and the natural frequency is ω .

Every combination of boundary conditions resulted in different frequencies and mode shapes. However, the frequencies and mode shapes varied from those of a free-free beam to those of a clamped-free beam as the mass and inertia both approached infinity. The characteristic equation, Eq. (5.4), results in that of the free-free beam with no tip mass and no tip inertia; fixed-free for infinite tip mass and infinite tip inertia; sliding-free for infinite inertia and no tip mass; and pinned-free for infinite mass and no tip inertia. The natural frequency of the n th mode is given as

$$\omega_n = (\lambda_n \ell)^2 \sqrt{\frac{EI}{\rho \ell^4}}. \tag{5.5}$$

The results demonstrate that using free-free mode shapes for flexible appendages is only valid for spacecraft with small values of mass and inertia. The cantilever mode shapes are valid only for both large values of inertia and mass. All values of mass and inertia between zero and infinity have modal properties that are dependent on Eq. (5.4). Eq. (5.4) demonstrates that orbital variation in the tip inertia (as the solar array rotates) caused variations in modal frequencies and mode shapes. The variations were harmonic with a frequency of twice the orbital rate.

As shown in Fig. 36, a consequence of this analysis was that when the modal frequencies varied with orbit, so did the potential for resonance due to instrument disturbances. The two resonance peaks shown in Fig. 36 were those for the end frequencies of a modal band. A modal band is defined as the resulting range of frequencies that a mode of vibration can have due to a harmonic change in boundary condition (e.g., rotation of tip inertia). The resonance peak varied harmonically throughout an orbit (2 cycles per orbit). As mass is expended (e.g., fuel for orbit adjust, cryogen sublimation), spacecraft mass and inertia will be reduced and the modal band will be shifted to increasing frequency. Fig. 37 shows the range of the UARS solar array flatwise and edgewise frequencies measured from day 128 through day 737 for the 90°, 180°, 270° and 360°

positions. At each position, there was a spread of the frequencies. However, the lower and upper extremities of the spread were harmonic with respect to the 360° of rotation. This harmonic variation of the extremities was indicative of modal bands. The modal band was defined by the highest frequency observed (0.29 Hz at 180°) and the lowest frequency observed (0.21 Hz at 90°). Fig. 37 also shows the output frequencies for the harmonic drives for the solar array (0.23 Hz), the high gain antenna (HGA, 0.22 Hz) and the gimbaled instrument mount (Solar-Stellar Pointing Platform (SSPP), 0.22 Hz). The harmonic drive output frequencies overlapped the modal band. The implication was that during the orbit, each of the three harmonic drives was in transitory resonance with the solar array flatwise and edgewise modes of vibration.

Another implication of this result was that when one considers structural models in control design, one must consider modal bands instead of discrete frequencies. Controller design must be robust enough to accommodate entire bands. Furthermore, controllers designed via optimization strategies are usually designed about some nominal configuration. Thus, variations in modal properties will result in suboptimal control performance for all other configurations.

5.3 Disturbance Transmission Variation with Appendage Rotation

Many disturbances on-board the spacecraft had fixed points of application and direction. Their transmission through the spacecraft was constant. However, the resulting disturbance response due to rotating flexible appendages varied with the appendage orientation to the disturbance source. This was true for all disturbances except for the solar array drive mechanism. The mode shapes changed (due to varying tip inertia and rotation) their orientation with respect to the disturbances. The overall dynamical system can be generalized as:

$$\begin{aligned}\dot{\mathbf{X}} &= \mathbf{A}\mathbf{X} + \mathbf{B}\mathbf{U} \\ \mathbf{Y} &= \mathbf{C}\mathbf{X}\end{aligned}\tag{5.6}$$

with \mathbf{U} fixed, and

$$\mathbf{B}^T = [\mathbf{0} \quad \Gamma(\mathbf{X}, t)].\tag{5.7}$$

The mode shapes, $\Gamma(\mathbf{X}, t)$, varied harmonically with a frequency of twice the solar array rotation frequency (orbital frequency). With fixed disturbances imparted to the rotating solar arrays, the resulting

jitter response had amplitude variations that were also harmonic and in synch with twice the solar array rotation rate. Because the spacecraft's latitude varied with solar array rotation, the resulting jitter response was latitude specific⁷. This result was significant because atmosphere observing satellites may attribute measurements that appeared as latitude specific to be due to an atmospheric phenomena when it was actually due to the latitude specific vibration pattern of the platform from which measurements were taken. Furthermore, since this was due to variation of mode shape orientation with respect to fixed disturbances, this effect was independent of the tip inertia variation due to rotation of the solar array.

5.4 Thermal Elastic Bending Analysis

This section presents analysis of environmental disturbance effects which resulted from the temperature gradient created when a spacecraft entered or exited the Earth's terminator. As a spacecraft's solar array entered sunlight, the side facing the sun heated at a faster rate than the side not facing the sun^{11, 12}. The thermal gradient caused the array to bend away from the sun. As the spacecraft entered the Earth's shadow, the side facing the sun cools more rapidly than the other side. The solar array temperature gradient was inversely dependent upon the angle, β . The angle β is defined as the complement of the angle between the orbit normal and the Earth-to-Sun vector¹¹. Fig. 38 shows the UARS solar array being deployed. Thermal bending is illustrated in Fig. 8. The bending resulted in an attitude perturbation. Perturbations were more pronounced about the spacecraft roll axis (axis of least inertia). This was caused by the solar energy incident on the large surface area of the array panel and the panels large mass moment of inertia about the spacecraft roll axis. The spacecraft attitude control system responded to the change in attitude with a correcting torque which restored the spacecraft's nominal attitude.

The thermal bending of the solar array was the most pronounced disturbance event recorded with the attitude control system rate gyros. Fig. 39 shows the roll attitude during two orbital sunrises for two orbits with different β angles. These angles are indicated on Figs. 39a and 39b. The peaks in Fig. 39, caused by solar array thermal bending, were approximately 125 arc-s and 75 arc-s for β angles of 25° and 38°, respectively. In addition to thermal bending, the solar array shadow temporarily shielded the instrument boom containing the Zenith Energetic Particle System instrument from the sun. This resulted in the thermal elastic bending of that boom being delayed by 300-400 s. The delay varied inversely with the Beta angle. The instrument boom bending effects were less pronounced because of the smaller solar incident surface area and smaller mass inertia. Furthermore, the bending stiffness for the instrument boom was an order of magnitude higher than that of the solar array. Much attention has been focused on the solar array thermal bending and its effect on the science measurements. However, the instrument boom produced a roll attitude displacement of 12 arc-s. This displacement may also have had some marginal effect on science measurements.

Data from orbits was examined at approximately 15 day intervals from day 128 through 737 past launch. The trough-to-peak roll attitude displacement and displacement duration was measured for each orbital sunset and sunrise thermal bending event. The displacements were then correlated with the β angle and solar array orientation during the displacement. Figs. 40 and 41 show the trough-to-peak roll attitude displacement resulting from thermal bending of the solar array during orbital sunrise and sunset, respectively. The displacements are annotated (rounded to nearest arc-s) for the respective β angle and solar array position. The magnitude of roll attitude perturbation was dependent upon the β angle and solar array orientation with respect to the drive shaft.

During orbital sunrise, Fig. 40, the displacement was larger for Beta angles near 17° and solar array orientations of 160° . The sunrise attitude displacements was as high as 271 arc-s. During orbital sunset, Fig. 41, the displacement was larger for Beta angles near 0° and solar array orientations near 90° . The sunset attitude displacement was as high as 425 arc-s. The perturbation events were usually 180 s in duration. Duration was dependent upon the β angle and the solar array orientation with respect to its drive shaft. The solar array completed approximately 1/3 revolution between sunset and sunrise. When the solar array was oriented at 90° (or 270° position) for maximum electrical power production, it also experienced the maximum attitude perturbation for sunset (sunrise).

The effect of spacecraft mass loss on thermal bending was also examined. UARS cryogen was completely outgassed on May 5, 1993 (day 603). UARS launch weight was 14820 lbs. Approximately 7% of UARS mass was outgassed. The mass loss should have resulted in the perturbation amplitude changing approximately 7%. Perturbations varied 180% due to variations in β angles. Perturbations varied 323% due to variations in solar array orientation angles. Figs. 42a and 42b show the roll attitude displacements from days 128 through 737 for sunset and sunrise thermal snaps, respectively. The displacements were referenced to the solar array position (ordinate) and day past launch (abscissa). The displacements were annotated similar to Figs. 40 and 41. The β angles for the displacements given in Figs. 42a and 42b are given in Fig. 42c. The effect of changing solar array position or Beta angle dominated the influence of thermal bending. Measurement of mass loss effects on thermal bending was not discernible due to the those effects.

UARS must meet a long-term stability requirement of bounding roll attitude displacement to 108 arc-s during any 60 s interval. Many of the perturbations examined violated this requirement. The stability requirements were necessary for interpretation of science data. Analysis has shown that the thermal bending of the solar array results in trough-to-peak roll attitude displacements of 425 arc-s during a 47 s interval.

The perturbations have also been observed on LANDSAT 4 and 5. Symmetric dual solar array satellites experienced such perturbation but they are more pronounced for asymmetric single arrays. When unobstructed viewing from the spacecraft side is required, such as on UARS or the Earth Observing System A.M. satellite, it is necessary to use single array spacecraft. Because the perturbations violated the long-term stability requirements and can be expected for single array spacecraft, it is critical that spacecraft designers have valid models to predict the response to thermal bending.

Concluding Remarks

Analysis using the Upper Atmosphere Research Satellite (UARS) flight data from the first 737 days past launch has provided better understanding of UARS in-flight dynamics. The investigation included two in-flight experiments on May 1, 1992 and September 17, 1993 which measured responses caused by disturbances on the satellite and the interaction between instruments. The solar array and the high gain antenna harmonic drives were identified as the excitation sources. High gain antenna stiction was also identified.

The solar array drive's harmonic drive output frequency resonated the solar array edgewise and flatwise modes with higher transmissivity to the edgewise mode. The solar array edgewise mode was the dominant mode of vibration. The response was latitude-specific with different jitter characteristics for forward and reverse rotation of the solar array. Because the edgewise mode of vibration was constrained (less slippage and flexing) by the gear drive, the drive damping countered the resonating effect of the solar array drive harmonic drive output. The solar array had bounded levels of vibration which exceeded the spacecraft pointing requirements. Because of the drive damping, catastrophic damage to the solar array was prevented. However, the flexing of the solar array panel transmitted through the gear drive may have reduced gear drive life.

Analysis of the high gain antenna showed that the drive excited the solar array edgewise and flatwise modes during targeting and two other structural modes during positioning. The high gain antenna also experienced stiction (static friction) which also produced a measurable disturbance. Although the jitter (up to 0.8 arc-s) was far less than that caused by the solar array, the amount was large enough to consider in the overall jitter budget of smaller spacecraft that must maintain pointing requirements similar to UARS.

Although UARS had many disturbance sources, orbital and configuration changes greatly influenced the dynamic response. Flight data has shown that modal frequencies and jitter amplitudes varied with a frequency of twice the solar array rotation rate. The variation of the solar array modal frequencies (near .25 Hz) produced a modal band. Within the band, the resonance frequency varied harmonically. Three UARS disturbances had frequencies which overlapped the modal band and thus produced a transitory resonance. Another consequence of modal variations due to configuration change was that disturbance transmission was also dependent upon the modal properties of a system. Hence, as the modal properties changed the disturbance transmission path changed.

Flight data indicated that both elastically flexible appendages experienced thermal elastic bending as the spacecraft crossed the Earth's terminator. Furthermore, the solar array provided a temporary shield between the boom containing the Zenith Energetic Particle System and the sun. This shield resulted in the thermal elastic bending of that boom being delayed by 300-400 s. The displacement was inversely dependent upon the Beta angle, β .

Analysis of the thermal elastic bending of the solar array has shown the effect of Beta angle and the solar array orientation on the spacecraft dynamic response. Trough-to-peak amplitude variations were as high as 425 arc-s. During sunset, the bending was higher for Beta angles near 0° and solar array orientation of near 90° . The roll attitude perturbations resulting from the solar array bending varied 180% due to Beta angle variations and 323% due to solar array orientation variations. The effect of the 7% mass loss on the thermal bending perturbations was not discernible due to the effects of array orientation variations and Beta angle variations.

The precession of the orbit caused the β angle to increase. Solar and stellar tracking instruments adjusted their tracking trajectories to accommodate the precession. The increased tracking activity produced higher disturbance levels which resulted in higher jitter amplitudes as the β angle increased. Between yaw maneuvers, the jitter increased monotonically. The direction of solar array rotation also had a pronounced effect on the subsequent jitter levels. The reversed solar array rotation resulted in higher jitter amplitudes than forward rotation.

Acknowledgments

The author extends his appreciation to the following people for their assistance and support: William L. Grantham, Jerry Newsom, John G. Wells Jr., Sudha M. Natarajan, and Janet L. Barnes of NASA Langley Research Center; Ansel Butterfield of Bionetics; Richard R. Lay and Robert F. Jarnot of the Jet Propulsion Laboratory; David A. Gell of University of Michigan; Richard Quinn, John Molnar, Anthony Camello, Eric Tate, Mike Garnek, Bob Hughes, John Stetson, Lara Phillip and George Futchko of Lockheed Martin; Farrell Scott of Florida A and M University; and Richard Beck, Bob Neff, and Sandy Austin of NASA Goddard Space Flight Center and Joseph Laufer.

References

- ¹Grantham, W. L., "NASA Future Mission Needs and Benefits of Controls-Structures Interaction Technology," NASA TM 104034, Jan 1991.
- ²Trevathan, C. E. and Burr, P. T. "Mission Requirements Document for the Upper Atmosphere Research Satellite," NASA Goddard Space Flight Center Document 430-1601-001, Sept. 1984.
- ³Butterfield, A. J. and Woodard, S. E., "Measured Spacecraft Instrument and Structural Interactions," *Journal of Spacecraft and Rockets*, Vol. 33, No. 4, July-August, 1996, pp. 556-562.
- ⁴Neste, S. L., "UARS Pointing Error Budgets," General Electric Astro-Space Division, PIR U-1K21-UARS-517, March 20, 1987.
- ⁵General Electric Company Astro-Space Division, "Upper Atmosphere Research Satellite Project Data Book," NASA Goddard Space Flight Center, April 1987.
- ⁶General Electric Company Astro-Space Division, "Upper Atmosphere Research Satellite Command and Telemetry Handbook," SDS-4219, January 1991.
- ⁷Woodard, S. E., Lay, R., Jarnot, R., Gell, D., "Experimental Investigation of Spacecraft In-Flight Disturbances and Dynamic Response," *Journal of Spacecraft and Rockets*, Vol. 34. No. 2, March-April 1997.
- ⁸Molnar, J. and Garnek, M., "UARS In-Flight Jitter Study for EOS," NASA CR 191419, Jan 1993.
- ⁹Sheldon, K. M., "Disturbance Torque Summary for UARS," PIR U-1K21-UARS-232, September 1985.
- ¹⁰Mills, R. and Garnek, M., "UARS Dynamic Disturbance Torque Analysis," PIR U-1K21 UARS 279, PIR U-1R44-UARS-1351, November 1985.

¹¹Zimbelman, D. F., “Thermal Elastic Shock and its Effect on Topex Spacecraft Attitude Control,” 14th Annual American Astronautical Society Guidance and Control Conference, February 2-6, 1991, Keystone, Colorado.

¹²Lambertson, M., Underwood, S., Woodruff, C. and Garber, A., “Upper Atmosphere Research Satellite Attitude Disturbances During Shadow Entry and Exit,” American Astronautical Society Paper No. AAS 93-319, 1993.

¹³Woodard , S. E., “Concurrent Fuzzy Logic Control of a Gimballed Payload and Space Platform System,” *Ph.D. Dissertation*, Duke University, Dept. of Mechanical Engineering and Materials Science, November 1995.

¹⁴Freesland, D., “Upper Atmosphere Research Satellite Attitude Determination and Control,” 15th Annual American Astronautical Society Guidance and Control Conference, Keystone, Colorado, February 8-12, 1992.

¹⁵Woodard, S. E., Gell, D. A. and Lay, R. R., “Measured Spacecraft Dynamic Effects on Atmospheric Science Instruments,” 35th Aerospace Sciences Meeting and Exhibit, AIAA Paper 97-0419, Reno, NV, 1997.

¹⁶Woodard ,S. E., “Concurrent Fuzzy Logic Control of a Gimballed Payload and Space Platform System,” *Ph.D. Dissertation*, Duke University, Dept. of Mechanical Engineering and Materials Science, November 1995.

Appendage 1

Modal Variation with Tip Inertia Rotation

One effect of variable spacecraft mass and inertia on appendage transverse vibration is due to the changing modal frequencies and mode shapes. The vibration of an appendage results in platform vibration. Development and examination of the Euler beam equation with the appropriate boundary conditions will show short-term (orbital) periodic changes in modal characteristics when flexible appendages rotate and long-term effects due to mass expenditure (fuel and/or cryogen expenditures).

Many flexible appendages can be modelled as Euler beams. Fig. 43 shows the free body diagram of an element of a beam with bending moment, M , shear force, V , uniform load distribution, W , and transverse displacement, y , measured along x . The boundary conditions for an appendage attached to a space platform are shown in Figure 44. The platform has mass, m_{tip} , and inertia, I_{tip} .

The Euler beam equation for such a system is given as:

$$(EIy'')'' + \rho A y'' = 0 \quad (A1.1)$$

with

$$(\quad)'' = \frac{\partial^2(\quad)}{\partial x^2}.$$

If harmonic motion is assumed, then separation of variables can be used to consider a solution of the following form

$$y(x,t) = \phi(x) \sin \omega t. \quad (A1.2)$$

The beam is assumed to have mass/unit length, ρ , modulus of elasticity, E , cross-sectional area, A , and area moment of inertia, I . This results in the equation:

$$(EI\phi'')'' - \rho A \omega^2 \phi = 0. \quad (A1.3)$$

Boundary conditions for a free-free beam are:

$$\frac{d^2\phi(0)}{dx^2} = 0, \quad \frac{d^2\phi(\ell)}{dx^2} = 0$$

$$\frac{d^3\phi(0)}{dx^3} = 0, \quad \frac{d^3\phi(\ell)}{dx^3} = 0$$

In this paper, only the free vibration of a uniform beam with fixed coefficients is considered, thus:

$$\frac{d^4\phi}{dx^4} - \lambda^4\phi = 0 \tag{A1.4}$$

where

$$\lambda^4 = \frac{(\rho A \omega^2)}{EI}$$

The partial derivatives of y with respect to time are

$$\frac{\partial y}{\partial t} = \omega\phi(x) \cos \omega t$$

$$\frac{\partial^2 y}{\partial t^2} = -\omega^2\phi(x) \sin \omega t$$

$$\frac{\partial^3 y}{\partial x \partial t^2} = -\omega^2\phi'(x) \cos \omega t$$

A general solution to the homogeneous differential Eq. (A1.4) is

$$\phi(x) = A_1 \cos(\lambda x) + A_2 \sin(\lambda x) + A_3 \cosh(\lambda x) + A_4 \sinh(\lambda x)$$

If the free-free beam has a tip mass m_{tip} , and tip inertia I_{tip} , at $x = \ell$, the bending moment and shear dynamics are given by:

$$EIy'' = -I_{tip} \frac{\partial^3 y}{\partial x \partial t^2} = I_{tip} \omega^2 \phi'(x) \sin \omega t$$

$$EIy''' = m_{tip} \frac{\partial^2 y}{\partial t^2} = -m_{tip} \omega^2 \phi(x) \sin \omega t.$$

At $x = 0$, there are no shearing forces or bending moments, thus

$$M = 0, \quad \text{and therefore } y'' = 0$$

(A1.5)

$$V = 0, \text{ and therefore } y''' = 0$$

(A1.6)

Eqs. (A1.5) and (A1.6) result in:

$$-A_1\lambda^2 + A_3\lambda^2 = 0$$

$$-A_2\lambda^3 + A_4\lambda^3 = 0.$$

Thus $A_3 = A_1$ and $A_4 = A_2$.

The homogeneous solution reduces to

$$\phi(x) = A_1(\cos(\lambda x) + \cosh(\lambda x)) + A_2(\sin(\lambda x) + \sinh(\lambda x))$$

(A1.7)

with boundary conditions at $x = 0$ of

$$EI\phi''(\ell) - I_{ip}\omega^2\phi'(\ell) = 0$$

(A1.8)

and

$$EI\phi'''(\ell) + m_{ip}\omega^2\phi(\ell) = 0$$

(A1.9)

The first three spatial derivatives of Eq. (A1.7) are

$$\phi'(x) = A_1\lambda(-\sin(\lambda x) + \sinh(\lambda x)) + A_2\lambda(\cos(\lambda x) + \cosh(\lambda x))$$

(A1.10)

$$\phi''(x) = A_1\lambda^2(-\cos(\lambda x) + \cosh(\lambda x)) + A_2\lambda^2(-\sin(\lambda x) + \sinh(\lambda x))$$

(A1.11)

$$\phi'''(x) = A_1\lambda^3(+\sin(\lambda x) + \sinh(\lambda x)) + A_2\lambda^3(-\cos(\lambda x) + \cosh(\lambda x))$$

(A1.12)

Substituting Eqs (A1.10) and (A1.11) into Eq. (A1.8),

$$A_1 \lambda^2 (-\cos(\lambda \ell) + \cosh(\lambda \ell)) + A_2 \lambda^2 (-\sin(\lambda \ell) + \sinh(\lambda \ell)) - A_1 \left(\frac{I_{ip} \omega^2}{EI} \right) \lambda (-\sin(\lambda \ell) + \sinh(\lambda \ell)) - A_2 \left(\frac{I_{ip} \omega^2}{EI} \right) \lambda (\cos(\lambda \ell) + \cosh(\lambda \ell)) = 0$$

Let

$$a_{11} = \lambda (-\cos(\lambda \ell) + \cosh(\lambda \ell)) - \left(\frac{I_{ip} \omega^2}{EI} \right) (-\sin(\lambda \ell) + \sinh(\lambda \ell))$$

$$a_{12} = \lambda (-\sin(\lambda \ell) + \sinh(\lambda \ell)) - \left(\frac{I_{ip} \omega^2}{EI} \right) (\cos(\lambda \ell) + \cosh(\lambda \ell))$$

$$a_{11} A_1 + a_{12} A_2 = 0$$

Substituting Eqs. (A1.7) and (A1.12) into Eq. (A1.9),

$$A_1 \lambda^3 (\sin(\lambda \ell) + \sinh(\lambda \ell)) + A_2 \lambda^3 (-\cos(\lambda \ell) + \cosh(\lambda \ell)) - A_1 \left(\frac{m_{ip} \omega^2}{EI} \right) (\cos(\lambda \ell) + \cosh(\lambda \ell)) + A_2 \left(\frac{m_{ip} \omega^2}{EI} \right) (\sin(\lambda \ell) + \sinh(\lambda \ell)) = 0$$

Let

$$a_{21} = \lambda^3 (\sin(\lambda \ell) + \sinh(\lambda \ell)) + \left(\frac{m_{ip} \omega^2}{EI} \right) (\cos(\lambda \ell) + \cosh(\lambda \ell))$$

$$a_{22} = \lambda^3 (-\cos(\lambda \ell) + \cosh(\lambda \ell)) + \left(\frac{m_{ip} \omega^2}{EI} \right) (\sin(\lambda \ell) + \sinh(\lambda \ell))$$

$$a_{21} A_1 + a_{22} A_2 = 0$$

$$\begin{bmatrix} a_{11} & a_{12} \\ a_{21} & a_{22} \end{bmatrix} \begin{bmatrix} A_1 \\ A_2 \end{bmatrix} = \begin{bmatrix} 0 \\ 0 \end{bmatrix}$$

One solution of the above equation is a trivial solution of, i.e., $A_1 = A_2 = 0$. The other is setting the determinant to zero

$$a_{11}a_{22} - a_{12}a_{21} = 0.$$

The solution for A_1 and A_2 , and thus the modes shape, are dependent upon finding the roots of the determinant. The determinant results in the following characteristic equation for the beam with tip mass and inertia.

$$\begin{aligned} & \lambda^4 [I - \cos(\lambda\ell)\cosh(\lambda\ell)] + \lambda \left(\frac{m_{tip}\omega^2}{EI} \right) [\sin(\lambda\ell)\cosh(\lambda\ell) - \cos(\lambda\ell)\sinh(\lambda\ell)] \\ & \lambda^3 \left(\frac{I_{tip}\omega^2}{EI} \right) [\cos(\lambda\ell)\sinh(\lambda\ell) + \sin(\lambda\ell)\cosh(\lambda\ell)] + I_{tip}m_{tip} \left(\frac{\omega^2}{EI} \right)^2 [I + \cos(\lambda\ell)\cosh(\lambda\ell)] = 0 \end{aligned} \quad (A1.13)$$

Every combination of boundary condition will result in different modes and mode shapes. However, the modes and mode shapes will vary from those of a free-free beam to those of a clamped-free beam as the mass and inertia both tend to approach infinity. The characteristic equation, Eq. (A1.13), developed here also results in that of the free-free beam with no tip mass and no tip inertia; fixed-free for infinite tip mass and infinite tip inertia; sliding-free for infinite inertia and no tip mass; and pinned-free for infinite mass and no tip inertia. The characteristic equations which can result from Eq. (A1.13) are shown in Table 14.

Appendix 2

UARS DISTURBANCE EXPERIMENT Instrument Activities during Yaw Manuever Day May 1, 1992

SEQUENCE OF EVENTS DURING EXPERIMENT

EVENT TIME (+ - 00:01:00)	EVENT MNEMONIC
1992:122:00:00:00	EXPERIMENT BEGINS
1992:122:19:39:23	SSPP REWIND START
1992:122:19:46:00	HGA SLEW TO TDRS WEST(TDW)AT .31 DEG/SEC
1992:122:19:46:41	SSPP REWIND STOP
1992:122:19:46:45	SSPP STARTS TRACKING STELLAR TARGET 58210001
1992:122:19:50:05	SSPP ENDS TRACKING STELLAR TARGET 58210001
1992:122:19:50:05	SSPP REWIND START
1992:122:19:50:27	SSPP REWIND STOP
1992:122:19:50:35	SSPP STARTS TRACKING STELLAR TARGET 10080053
1992:122:19:53:18	EQUATOR CROSSING (DESCENDING NODE)
1992:122:19:53:55	SSPP ENDS TRACKING STELLAR TARGET 10080053
1992:122:19:53:55	SSPP REWIND START
1992:122:19:54:01	HGA ARRIVE TDW (WAITS FOR TDW TO COME INTO VIEW)
1992:122:19:54:05	SSPP REWIND END
1992:122:19:54:25	SSPP STARTS TRACKING STELLAR TARGET 58210001
1992:122:19:57:55	SSPP ENDS TRACKING STELLAR TARGET 58210001
1992:122:19:57:55	SSPP REWIND START
1992:122:20:00:00	HRDI CALIBRATION COMPLETE/HRDI STATIONARY
1992:122:20:04:34	SSPP REWIND STOPS
1992:122:20:13:17	HALOE SUNRISE SCAN STARTS (HALOE SUNRISE SCAN BEGINS AT 00:02:30 BEFORE SC_SUNRISTPA_ZERO AND ENDS APPROX. 00:06:40 LATER, HRDI STATIONARY)
1992:122:20:19:57	HALOE SUNRISE SCAN ENDS
1992:122:20:42:08	SSPP STARTS TRACKING SUN

1992:122:20:17:12	MLS NOMINAL SCAN
	MLS ON/OFF PROGRAM BEGINS
1992:122:20:17:12	MLS Quiet for 9 EMAFS-09:50 (EACH MLS EMAF IS 65 SEC)
1992:122:20:26:00	HGA TRACKS TDW
1992:122:20:27:02	MLS Normal Mirror Sequence for 5 EMAFS
1992:122:20:32:29	MLS Quiet for 5 EMAFS
1992:122:20:37:57	MLS Normal Antenna Sequence for 5 EMAFS

1992:122:20:43:25 **MLS Quiet for 5 EMAFS**
1992:122:20:48:52 **MLS Normal Mirror and Antenna**
 Scan Sequence for 5 EMAFS

MLS ON/OFF PROGRAM ENDS

1992:122:20:54:20 **MLS Quiet**

1992:122:20:57:00 HGA SLEW TO TRDS EAST(TDE)
1992:122:21:04:14 HGA ARRIVE TDE
1992:122:21:07:00 HGA TRACK TDE
1992:122:21:07:30 HALOE SUNSET SCAN BEGINS
 (HALOE SUNSET SCAN BEGINS AT 00:00:45
 BEFORE SC_TAN450SEC)

1992:122:21:15:38 SSPP STOPS TRACKING SUN
1992:122:21:15:38 SSPP REWIND STARTS
1992:122:21:16:38 HALOE SUNSET ENDS
 (HALOE SUNSET ENDS AT SC_SUNSETTPA_ZERO)

1992:122:21:22:51 SSPP REWIND STOPS
1992:122:21:23:57 SSPP STARTS TRACKING STELLAR TARGET 6450045
1992:122:21:32:38 SSPP STOPS TRACKING STELLAR TARGET 6450045
1992:122:21:32:38 SSPP REWIND STARTS
1992:122:21:35:00 HGA SLEW TO TDW
1992:122:21:42:35 HGA ARRIVE TDW
1992:122:21:46:34 SSPP REWIND STOPS
1992:122:21:49:33 HALOE SUNRISE SCAN STARTS
1992:122:21:56:13 HALOE SUNRISE SCAN ENDS
1992:122:22:08:00 HGA TRACK TDW
1992:122:22:18:23 SSPP STARTS TRACKING SUN
1992:122:22:30:00 **HRDI DAY SCAN STARTS**
1992:122:22:38:00 HGA SLEW TO TDE
1992:122:22:43:45 HALOE SUNSET SCAN STARTS
1992:122:22:45:21 HGA ARRIVE TDE
1992:122:22:46:34 **HRDI NIGHT SCAN STARTS**
 (HRDI NIGHT SCAN STARTS AT SC_SUNSETNAD
 + APPROX. 00:00:30)

1992:122:22:51:00 HGA TRACK TDE
1992:122:22:51:53 SSPP STOPS TRACKING SUN
1992:122:22:51:53 SSPP REWIND STARTS
1992:122:22:52:53 HALOE SUNSET SCAN ENDS

MLS ON/OFF PROGRAM BEGINS

1992:122:22:56:40 **MLS Quiet for 9 EMAFS-09:50 (EACH MLS**
 EMAF IS 65 SEC)
1992:122:22:59:12 SSPP REWIND STOPS
1992:122:22:59:12 SSPP STARTS TRACKING STELLAR TARGET 58210001
1992:122:23:05:48 SSPP STOPS TRACKING STELLAR TARGET 58210001
1992:122:23:05:48 SSPP REWIND STARTS
1992:122:23:06:30 **MLS Normal Mirror Sequence for 5 EMAFS**

1992:122:23:11:01 SSPP REWIND STOPS
1992:122:23:11:58 **MLS Quiet for 5 EMAFS**
1992:122:23:17:25 **MLS Normal Antenna Sequence for 5 EMAFS**
1992:122:23:19:00 HGA SLEW TO TDW
1992:122:23:22:53 **MLS Quiet for 5 EMAFS**
1992:122:23:28:21 **MLS Normal Mirror and Antenna Scans**
1992:122:23:26:02 HGA ARRIVE TDW

1992:122:23:25:58 HALOE SUNRISE SCAN STARTS

MLS ON/OFF PROGRAM ENDS

1992:122:23:32:38 HALOE SUNRISE SCAN ENDS
Scan Sequence for 5 EMAFS

1992:122:23:34:43 HRDI DAY SCAN STARTS
1992:122:23:35:00 **MLS NORMAL MIRROR AND ANTENNA SCAN SEQUENCE**
1992:122:23:50:00 HGA TRACK TDW
1992:122:23:54:38 SSPP STARTS TRACKING SUN

1992.122.23.59.59 **EXPERIMENT ENDS**

Appendix 3

UARS PAYLOAD INTERACTION EXPERIMENT Instrument Activities during Yaw Manuever Day September 17, 1993

SSPP stationary for entire experiment.

High gain antenna view periods for Tracking and Data Relay Satellites

1993:260:10:50:00	1993:260:11:17:00	00:27:00	TDE
1993:260:11:48:00	1993:260:12:04:00	00:16:00	TDW
1993:260:12:12:00	1993:260:12:16:00	00:04:00	TDW
1993:260:12:31:00	1993:260:12:59:00	00:28:00	TDE
1993:260:13:28:00	1993:260:13:43:00	00:15:00	TDW
1993:260:13:51:00	1993:260:14:11:00	00:20:00	TDW
1993:260:14:35:00	1993:260:14:54:00	00:19:00	TDE
1993:260:15:24:00	1993:260:15:54:00	00:30:00	TDW
1993:260:16:06:00	1993:260:16:34:00	00:28:00	TDE
1993:260:17:12:00	1993:260:17:43:00	00:31:00	TDW
1993:260:17:48:00	1993:260:18:15:00	00:27:00	TDE
1993:260:18:59:00	1993:260:19:30:00	00:31:00	TDW

HRDI sequence of events

1993:260:13:00:00 HRDI stationary at least 8 min before MLS ON/OFF program.
1993:260:14:27:00 HRDI day scan begins 20 min after MLS begins limb pointing
(HRDI night scan begins at SC_SUNSETNAD + APPROX.
00:00:30 min)

HRDI night scan ends 5 min after HALOES scan ends

HRDI normal scan sequences commence 20 min before HALOE
scan

MLS sequence of events

Begin MLS ON/OFF program 8 minutes before solar array is parked to examining free decay with disturbance due to MLS. Solar array is parked before sunset that occurs during yaw orbit. Exact time depends upon offset which varies from 40 to 60 degrees to restrict peak current produced in battery charging. This has been a procedure since August 1992.

MLS on/off program begins

MLS Quiet for (8 min before solar array stops + 6 min after) 14 EMAFS- (EACH MLS EMAF
(Engineering major frame) IS 65 SEC)
MLS Normal Mirror Sequence for 4 EMAFS
MLS Quiet for 5 EMAFS

MLS Normal Antenna Sequence for 4 EMAFS
MLS Quiet for 5 EMAFS
MLS Normal Mirror and Antenna Scan Sequence for 4 EMAFS

MLS on/off program ends

MLS Quiet

MLS antenna maintains Earth's limb (35 to 36 km) after yaw completion (1993:260:14:07:07)
MLS commences normal scan sequence

**SEQUENCE OF EVENTS DURING UARS PAYLOAD
INTERACTION EXPERIMENT**

EVENT TIME (+ - 00:01:00)	EVENT MNEMONIC
1993:260:14:03:19	SC_SUNRIS150
1993:260:14:04:10	SC_FOV135SUN_ND
1993:260:14:04:32	SC_FOV135CLD_ND
1993:260:14:08:39	SC_FOV90SUN_ND
1993:260:14:08:53	SC_SUNRISNAD
1993:260:11:19:28	SC_ASCNODE
1993:260:11:39:53	SC_FOV45SUN_DN
1993:260:11:40:11	SC_FOV45CLD_DN
1993:260:11:42:25	SC_TAN450SEC
1993:260:11:44:17	SC_FOV90SUN_DN
1993:260:11:44:28	SC_SUNSETNAD
1993:260:11:44:40	SC_FOV90CLD_DN
1993:260:11:48:48	SC_FOV135SUN_DN
1993:260:11:49:02	SC_FOV135CLD_DN
1993:260:11:49:55	SC_SUNSET150
1993:260:11:50:37	SC_SUNSETCEN
1993:260:11:50:48	SC_SUNSETTPA_ZERO
1993:260:11:51:10	SC_SUNSETTAN
1993:260:12:07:30	SC_DESNODE
1993:260:12:25:48	SC_SUNRISTAN
1993:260:12:26:11	SC_SUNRISTPA_ZERO
1993:260:12:26:18	SC_SUNRISCEN
1993:260:12:27:03	SC_SUNRIS150
1993:260:12:27:55	SC_FOV45CLD_ND
1993:260:12:28:15	SC_FOV45SUN_ND
1993:260:12:32:24	SC_FOV90CLD_ND
1993:260:12:32:37	SC_SUNRISNAD
1993:260:12:32:50	SC_FOV90SUN_ND
1993:260:12:37:02	SC_FOV135CLD_ND
1993:260:12:37:17	SC_FOV135SUN_ND
1993:260:12:37:34	SC_SAAENT
1993:260:12:55:41	SC_ASCNODE
1993:260:12:57:29	SC_SAAEXT
<hr/>	
1993:260:13:00:00	EXPERIMENT BEGINS
<hr/>	
1993:260:13:00:00	HRDI stationary at least 8 min before MLS ON/OFF program.
1993:260:13:16:08	SC_FOV45SUN_DN
1993:260:13:16:29	SC_FOV45CLD_DN
1993:260:13:17:56	HALOE SUNSET SCAN BEGINS (DURING YAW ORBIT, HALOE SUNSET SCAN BEGINS AT SC_TAN450SEC +/- 00:00:45 sec. ALSO, THE ONLY HALOE EVENT OCCURS AT THE SUNSET

IMMEDIATELY BEFORE THE YAW. THERE IS NO HALOE
EVENT IMMEDIATELY AFTER THE YAW MANUEVER).

1993:260:13:18:41	SC_TAN450SEC
1993:260:13:20:31	SC_FOV90SUN_DN
1993:260:13:20:45	SC_SUNSETNAD
1993:260:13:20:58	SC_FOV90CLD_DN
1993:260:13:25:03	SC_FOV135SUN_DN
1993:260:13:25:19	SC_FOV135CLD_DN
1993:260:13:26:11	SC_SUNSET150
1993:260:13:26:53	SC_SUNSETCEN
1993:260:13:27:04	SC_SUNSETTPA_ZERO

1993:260:13:27:04	HALOE SUNSET SCAN ENDS (HALOE SUNSET ENDS AT SC_SUNSETTPA_ZERO)
-------------------	--

YAW MANUEVER BEGINS

1993:260:13:27:07	SC_YAWMAN
1993:260:13:27:26	SC_SUNSETTAN
1993:260:13:43:43	SC_DESNODE

1993:269:13:59:57	NORMALY HALOE SUNRISE SCAN STARTS. BUT DURING YAW, THIS EVENT DOES NOT OCCUR. (HALOE SUNRISE SCAN BEGINS AT 00:02:30 BEFORE SC_SUNRISTPA_ZERO AND ENDS APPROX. 00:06:40 LATER, HRDI STATIONARY)
-------------------	---

1993:260:14:02:05	SC_SUNRISTAN
1993:260:14:02:27	SC_SUNRISTPA_ZERO
1993:260:14:02:35	SC_SUNRISCEN

**SOLAR ARRAY WILL BEGIN TO
ROTATE AFTER SUNRISE**

1993:260:14:09:08	SC_FOV90CLD_ND
1993:260:14:13:17	SC_FOV45SUN_ND
1993:260:14:13:34	SC_FOV45CLD_ND
1993:260:14:17:03	SC_SAAENT
1993:260:14:31:55	SC_ASCNODE

1993:260:14:27:00	HRDI DAY SCAN BEGINS 20 MIN AFTER MLS BEGINS LIMB POINTING (HRDI NIGHT SCAN BEGINS AT SC_SUNSETNAD + APPROX. 00:00:30 MIN)
1993:260:14:33:30	SC_SAAEXT
1993:260:14:52:23	SC_FOV135CLD_DN
1993:260:14:52:46	SC_FOV135SUN_DN
1993:260:14:52:01	HALOE SUNSET SCAN BEGINS
1993:260:14:54:57	SC_TAN450SEC
1993:260:14:56:45	SC_FOV90CLD_DN
1993:260:14:57:01	SC_SUNSETNAD
1993:260:14:57:16	SC_FOV90SUN_DN
1993:260:14:57:31	HRDI NIGHT SCAN BEGINS AT SC_SUNSETNAD + APPROX. 00:00:30
1993:260:15:00:50	SC_ZOEENT
1993:260:15:01:18	SC_FOV45CLD_DN
1993:260:15:01:36	SC_FOV45SUN_DN
1993:260:15:02:19	SC_ZOEEXT
1993:260:15:02:27	SC_SUNSET150
1993:260:15:03:10	SC_SUNSETCEN
1993:260:15:03:20	SC_SUNSETTPA_
1993:260:15:03:20	HALOE SUNSET SCAN ENDS
1993:260:15:03:43	SC_SUNSETTAN
1993:260:15:08:00	HRDI NIGHT SCAN ENDS 5 MIN AFTER HALOES SCAN ENDS
1993:260:15:19:57	SC_DESNODE
1993:260:15:35:51	HALOE SUNRISE SCAN BEGINS
1993:260:15:38:21	SC_SUNRISTAN
1993:260:15:38:43	SC_SUNRISTPA_ZERO
1993:260:15:38:51	SC_SUNRISCEN
1993:260:15:39:35	SC_SUNRIS150
1993:260:15:40:25	SC_FOV135SUN_ND
1993:260:15:40:50	SC_FOV135CLD_ND
1993:260:15:42:31	HALOE SUNRISE SCAN ENDS
1993:260:15:44:53	SC_FOV90SUN_ND
1993:260:15:45:10	SC_SUNRISNAD
1993:260:15:45:26	SC_FOV90CLD_ND
1993:260:15:49:32	SC_FOV45SUN_ND
1993:260:15:49:52	SC_FOV45CLD_ND
1993:260:15:57:49	SC_SAAENT
1993:260:16:06:29	SC_SAAEXT
1993:260:16:08:09	SC_ASCNODE

1993:260:16:10:00	HRDI DAY SCAN BEGINS
1993:260:16:28:37	SC_FOV135CLD_DN
1993:260:16:29:03	SC_FOV135SUN_DN
1993:260:16:30:28	HALOE SUNSET SCAN BEGINS
1993:260:16:31:13	SC_TAN450SEC
1993:260:16:32:59	SC_FOV90CLD_DN
1993:260:16:33:17	SC_SUNSETNAD
1993:260:16:33:34	SC_FOV90SUN_DN
1993:260:16:33:47	HRDI NIGHT SCAN BEGINS AT SC_SUNSETNAD + APPROX. 00:00:30 MIN
1993:260:16:37:33	SC_FOV45CLD_DN
1993:260:16:37:54	SC_FOV45SUN_DN
1993:260:16:38:43	SC_SUNSET150
1993:260:16:39:26	SC_SUNSETCEN
1993:260:16:39:36	HALOE SUNSET SCAN ENDS
1993:260:16:39:36	SC_SUNSETTPA_ZERO
1993:260:16:39:59	SC_SUNSETTAN
1993:260:16:41:46	SC_ZOEENT
1993:260:16:48:09	SC_ZOEEXT
1993:260:16:56:10	SC_DESNODE
<hr/>	
1993:260:16:56:10	END EXPERIMENT
<hr/>	
1993:260:16:56:10	HRDI AND MLS BEGIN NORMAL OPERATIONS
1993:260:17:12:29	HALOE SUNRISE SCAN BEGINS
1993:260:17:14:37	SC_SUNRISTAN
1993:260:17:14:59	SC_SUNRISTPA_ZERO
1993:260:17:15:07	SC_SUNRISCEN
1993:260:17:15:51	SC_SUNRIS150
1993:260:17:16:39	SC_FOV135SUN_ND
1993:260:17:17:07	SC_FOV135CLD_ND
1993:260:17:19:09	HALOE SUNRISE SCAN ENDS
1993:260:17:21:07	SC_FOV90SUN_ND
1993:260:17:21:26	SC_SUNRISNAD
1993:260:17:21:44	SC_FOV90CLD_ND
1993:260:17:25:46	SC_FOV45SUN_ND
1993:260:17:26:09	SC_FOV45CLD_ND
1993:260:17:44:22	SC_ASCNODE

1993:260:18:04:52	SC_FOV135CLD_DN
1993:260:18:05:21	SC_FOV135SUN_DN
1993:260:18:06:45	HALOE SUNSET SCAN BEGINS
1993:260:18:07:30	SC_TAN450SEC
1993:260:18:09:14	SC_FOV90CLD_DN
1993:260:18:09:33	SC_SUNSETNAD
1993:260:18:09:52	SC_FOV90SUN_DN
1993:260:18:13:48	SC_FOV45CLD_DN
1993:260:18:14:12	SC_FOV45SUN_DN
1993:260:18:15:00	SC_SUNSET150
1993:260:18:15:42	SC_SUNSETCEN
1993:260:18:15:53	HALOE SUNSET SCAN ENDS
1993:260:18:15:53	SC_SUNSETTPA_ZERO
1993:260:18:16:15	SC_SUNSETTAN
1993:260:18:25:40	SC_ZOEENT
1993:260:18:32:24	SC_DESNODE

Limb Viewing Instruments (arc-s, 3 σ)												
Instrument	Placement			Knowledge			Long Term Stability			Short Term Stability (Jitter)		
	Roll	Pitch	Yaw	Roll	Pitch	Yaw	Roll	Pitch	Yaw	Roll	Pitch	Yaw
CLAES ¹	900	1800	1800	108	360	360	108/(60 s)			54/(1 s)		
ISAMS	720	1800	1080	360	900	540	Not Specified			Roll, Pitch: 36/(2 s)		
MLS ^{2, 3}	1800	1270	1270	225	1270	1270	90	180	180	18	36	36
							per 65 s			per 2 s		
WINDII	360	360	720	120	120	120	60/(18 s)			4/(2 s)	4/(2 s)	30/(2 s)
HRDI	360	360	360	108	108	100	72/(10 s)			36/(0.125 s)		
Boom and Body Mounted Instruments (arc-s, 3 σ)												
HALOE	2700			1332			36/(1 s)			9/(0.25 s)		
PEM: AXIS	1800			900			NA			88/(1 s)		
PEM: ZEPS	1800			1800			NA			88/(1 s)		
PEM: NEPS	1800			1800			NA			88/(1 s)		
Solar and Stellar Viewing Instruments (arc-s, 3 σ)												
ACRIM II	180 each axis			90 each axis			Not specified			Not Specified		
SOLSTICE (Solar /Stellar)	(180/360)			(90/180)			60/(1000 s)			60/(1 s)		
SUSIM	180			90			60/(1000 s)			60/(1 s)		

Table 1 Instrument pointing requirements.

¹ Knowledge for CLAES (roll) and HRDI and WINDII (roll, pitch and yaw) are after on-orbit alignment calibration.

² Nominal values, basic requirement is $\sqrt{\text{Pitch}^2 - \text{Yaw}^2} \leq 1800$.

³ A priori knowledge, i.e. without using definitive ephemeris or attitude knowledge.

Disturbance	Description	Trigger
Thermal Snap	Thermal elastic bending of solar array due to rapidly changing thermal environment	Terminator crossing
Halogen Occultation Experiment (HALOE) sunrise and sunset occultation measurements	HALOE unstows, targets and tracks sun through atmosphere then stows	Orbital sunrise and sunset
Microwave Limb Sounder (MLS) antenna	Approx. 27 forward steps followed by 2 rewind steps	Continuously repeated throughout orbit
MLS switching mirror	Rapid slew/stop through 3 positions	Continuously repeated throughout orbit
Solar/Stellar Pointing Platform (SSPP)	Positions, stops, targets (sun or stellar target), stops, positions for next target	Position of sun or stellar target
High gain antenna	Positions, stops, targets Tracking and Data Relay Satellite (TDRS), stops, positions for next TDRS	TDRS (east or west) positions
Solar array stopping and rewinding	Changing direction of solar array rotation	Yaw maneuver completion
High Resolution Doppler Imager (HRDI) day/night scan transition	Rapid rotation of azim. and elev. gimbals.	Orbital sunrise and sunset
HRDI day/night scans	Elev. rotation (down) followed by 90° azim. rotation followed by elev. rotation (up)	Continuous repeated day scans from sunrise to sunset. Same for night scans (sunset to sunrise)
Reaction wheels	Performs attitude changes, stability and momentum management	Change in attitude and rate; commanded attitude biases
Magnetic torques	Provides reaction wheel momentum unloading	Excessive change in attitude rate
Propulsion subsystem	Thrust to spacecraft using hydrazine propulsion module	Orbit adjustments. Also used in conjunction with magnetic torques to unload reaction wheels

Table 2 UARS disturbances known before launch.

	Roll	Pitch	Yaw
Solar Array, I_x (rotation)	1.87e-2	7.22e-3	6.43e-3
Solar Array, I_y	1.13e-1	4.34e-2	3.87e-2
Solar Array, I_z	1.15e-1	4.00e-2	3.92e-2
SSPP Alpha	3.50e-2	1.30e-2	1.20e-2
SSPP Beta	3.20e-2	1.20e-2	1.10e-2
HGA Alpha	1.10e-3	4.10e-4	3.70e-4
HGA Beta	2.40e-3	9.40e-4	8.40e-4
MLS Antenna	3.90e-4	-	-
MLS Scanning Mirror	-	-	7.30e-5
HALOE Elevation	1.20e-4	4.70e-5	-
HALOE Azimuth	-	-	3.90e-5
HRDI Elevation	1.90e-5	7.30e-6	-
HRDI Azimuth	-	-	1.20e-5

Table 3 Ratios of payload gimballed inertia to spacecraft inertia.

Appendage	EI_1 (psi)	EI_2 (psi)	GJ(psi)
Solar Array	5.33E6	4.20E6	1.20E6
HGA Boom	3.28E7	3.28E7	2.55E6
Instrument Boom (for ZEPS)	5.25E7	5.15E7	1.00E6
SSPP Boom	3.38E8	3.38E8	3.07E7
SSPP Gimbal	$k_{\theta_x} = k_{\theta_y} = 2.11E5 \frac{\text{in} \cdot \text{lb}}{\text{rad}}$		

Table 4 Stiffness properties for the deployed appendages.

Mode No.	45°	90°	135°	180°	270°	Description
1	0.222	0.262	0.221	0.213	0.249	Solar array 1st flatwise bending
2	0.278	0.232	0.279	0.288	0.231	Solar array 1st edgewise bending
3	0.716	0.716	0.717	0.718	0.718	Solar array 1st torsion about Y
4	0.794	0.794	0.794	0.794	0.795	ZEPS Boom 1st bending in X
5	0.851	0.844	0.850	0.855	0.831	ZEPS Boom 1st bending in Y
6	1.13	1.15	1.15	1.14	1.17	Solar array 2nd flatwise bending
7	1.18	1.18	1.18	1.18	1.19	Solar array support tubes
8	1.70	1.70	1.70	1.70	1.70	SSPP rotation about Y (Alpha)
9	1.82	1.82	1.82	1.82	1.82	SSPP rotation about X (Beta)
10	2.09	2.07	2.11	2.16	2.17	Solar array 3rd flatwise bending
11	2.35	2.35	2.35	2.35	2.35	ZEPS 1st torsion about Z
12	2.67	2.67	2.67	2.67	2.67	Solar array 2nd torsion about Y
13	3.50	3.50	3.50	3.50	3.50	HRDI telescope torsion about Z (azimuth)
14	3.56	3.56	3.56	3.56	3.83	HRDI telescope torsion about Y (zenith)

Table 5 Frequency (Hz) predictions at various solar array positions using finite element modelling analysis.

Event Number	Time (s)	Description
1	438	HALOE begins sunset scan
2	592	HRDI begins night scan
3	858	SSPP rewind
4	990	Sunset thermal snap
5	998	HALOE sunset scan ends
6	1028	SSPP begins stellar tracking
7	1492	SSPP rewind
8	1682	HGA slew to TDRS-West
9	2077	SSPP stops; waits for Sun to come in view
10	2096	HGA stops; waits for TDRS-West to come into view
11	2761	HALOE sunrise scan begins
12	2939	Sunrise thermal snap
13	2987	SSPP begins tracking Sun
14	3394	HALOE sunrise scan ends
15	3427	HRDI transitions to day scan
16	4161	HGA begins to track TDRS-West
17	5008	SSPP rewind
18	5190	SSPP stops; waits for stellar target to come in view
19	5825	HGA slew to TDRS-East

Table 6 Disturbance events during first orbit on January 28, 1992.

0°	45°	90°	135°	180°	225°	270°	315°	360°
0.9494	0.9442	0.9788	0.9435	0.9536	0.2725	0.2321	0.2321	0.9435
0.2802	0.2438	0.2574	0.2321	0.2321	0.2321	1.0495	0.9536	0.2725
0.2335	0.3372	0.2069	2.1645	0.2927	0.9889	1.9425	0.4793	0.2321
2.1582	2.9313	1.1151	0.3784	0.4894	1.0646	0.9788	1.9778	2.1493
0.0259	1.9611	1.5893	0.4793	2.1493	0.3936	2.0030	2.1746	2.9313
2.9364	2.3813	2.9061	1.0999	0.7114	1.1756	0.7467	1.9324	0.7114
0.7211	2.1634	1.3824	2.9313	2.9465	2.9465	2.5075	2.9818	1.0293

Table 7 Dominant frequencies (Hz) of vibration at various solar array positions using roll gyro data (Day 139).

0°	45°	90°	135°	180°	225°	270°	315°	360°
0.9494	0.9494	0.2574	0.9687	0.9435	0.2574	0.2574	0.2725	0.9889
0.2438	1.9611	0.0858	0.2321	0.0858	1.0646	1.0747	0.9435	0.2473
1.9559	0.2542	1.6599	2.0182	0.2473	1.0041	0.7467	3.8597	2.0282
2.9364	0.0934	1.3320	0.0858	1.9778	2.1140	2.0787	1.9324	0.7467
0.7315	2.9313	1.9072	1.2462	0.2574	2.8456	2.1241	2.0888	1.2967
0.2802	0.7315	1.4430	3.0524	0.3431	1.7457	1.9072	2.7245	2.8708
1.2244	1.2244	2.1746	1.8567	0.7215	1.7003	1.2109	3.0070	2.2099

Table 8 Dominant frequencies (Hz) of vibration at various solar array positions using pitch gyro data (Day 139).

0°	45°	90°	135°	180°	225°	270°	315°	360°
2.9313	2.9364	0.2321	2.9212	2.9313	2.9313	0.2321	2.9313	2.9313
0.9546	0.0830	2.9465	0.0757	0.0858	0.2473	2.9465	0.2321	0.2321
0.2438	0.2542	0.0858	0.2473	0.2473	0.9435	0.7215	0.7215	0.9536
0.0363	0.9650	0.4037	0.4037	0.4037	0.7367	0.9435	1.0141	0.7215
0.7211	0.4047	0.5651	0.5752	0.5651	0.1867	1.0394	1.2109	1.0394
1.2244	0.5759	0.7367	0.7367	0.9435	2.3461	2.1493	2.1493	1.2109
1.7069	0.7419	0.9183	0.9536	0.7367	1.2210	1.7003	0.4541	1.8718

Table 9 Dominant frequencies (Hz) of vibration at various solar array positions using yaw gyro data (Day 139).

Day	Beta Angle (deg)	Orbit Start (s)	Orbit Complete (s)	Instrument/ Subsystem Orbital Status					
				HALOE	HGA	HRDI	MLS	Solar Array	SSPP
128	9.02	36521	94665	+	+	+, S(after sunrise)	+	+, F	+
133	25.90	14446	20222	+	+	+	+	+, F	+
139	38.13	378	6137	+	+	+	+	+	+
188	-28.82	-	-	-	-	-	-	-	-
206	47.20	39690	45449	+	+	+	+	+, F	+
233	2.01	73215	78983	Disturbance Experiment					
265	2.38	-	-	-	-	-	S	S	-
266	6.30	-	-	-	+	-	-	S	-
281	64.73	-	-	-	-	-	-	S	-
301	20.60	39474	45257	-	+, S(40995 - 42122s)	-	+, S(45282 -)	S	-
306	0.45	-	-	+	+	S	+	+, F	+
307	-3.38	-	-	-	-	-	S	S	-
326	-34.24	76548	82332	+	+	+	+	+, B	+
339	6.60	45395	50924	+	+	+	+	+, F	+
356	64.16	43738	49514	S	+	+	+	+, F	+
370	25.34	47907	53682	+	+	+	+	+, F	+
386	-42.26	45309	51085	+	+	+	+	+, B	+
400	-53.95	47062	52837	+	+	+	+	+, B	+
417	10.52	-	-	+	+	+	+	+, F	+
431	38.26	45865	51641	+	+	+	+	+, F	+

+ Nominal, S Stationary, F Forward rotation of solar arry, B Backward rotation of solar arry, HALOE operates only during thermal snap

Table 10a Summary of orbital and instrument status (days 128 through 431).

Day	Beta Angle (deg)	Orbit Start (s)	Orbit Complete (s)	Instrument/ Subsystem Orbital Status					
				HALOE	HGA	HRDI	MLS	Solar Array	SSPP
447	-7.34	43728	49503	+	+	+	+	+, B	+
461	-62.55	43792	49469	S	+	+	+	+, B	+
478	-38.68	-	-	+	+	+	+	+, B	+
492	17.22	43652	49411	+	+	+	+	+, F	+
509	29.51	47955	53714	+	+	+	+	+, F	+
523	-19.68	48141	53900	+	+	+	+	+, B	+
537	-64.37	45936	51712	+	+	+	+	+, B	+
551	-23.10	43993	49760	+,S(50802-54087s)	+	+,S(50164-54118s)	+,S(50228-54246s)	+, B	+
568	48.21	44732	50507	+	+	+	+	+, F	+
582	45.88	43272	49031	+	+	+	+	+, F	+
598	-15.24	43960	49728	+	+	+	+	+, B	+
612	-37.21	47391	53158	+	+	+	+	+, B	+
629	15.85	48220	53979	+	+	+	+	+, F	+
632	28.37	-	-	no data	+	no data	S	+, F	+
643	74.08	45097	50873	-	+	+	+	+, F	+
737	-2.01	52904	58597	Payload-Interaction Experiment					

+ Nominal, S Stationary, F Forward rotation of solar array, B Backward rotation of solar array, HALOE operates only during thermal snap

Table 10b Summary of orbital and instrument status (days 447 through 737).

Day	Beta Angle (deg)	Roll Jitter Ampl. (arc-s)			Freq. (Hz) \pm 0.01526			
		Max.	Avg.	Med.	85-95 deg.	175-185 deg.	265-275 deg.	345-355 deg.
128	9.02	9.90	2.26	2.15	0.2138	0.2902	0.2367	0.2367
133	25.90	16.85	2.86	2.35	0.2444	0.2444	0.2444	0.2367
139	38.13	12.75	2.92	2.60	0.2367	0.2444	0.2444	0.2902
188	-28.82	-	-	-	-	-	-	-
206	47.20	15.80	3.13	2.50	0.2444	0.2444	0.2444	0.2902
233	2.01	14.95	3.40	2.85	0.2597	0.2367	0.2444	0.2367
265	2.38	-	-	-	-	-	-	-
266	6.30	-	-	-	-	-	-	-
281	64.73	-	-	-	-	-	-	-
301	20.60	3.35	0.60	0.50	-	-	-	-
306	0.45	-	-	-	-	-	-	-
307	-3.38	-	-	-	-	-	-	-
326	-34.24	16.00	3.94	3.25	0.2444	0.2902	0.2367	0.2367
339	6.60	7.95	2.22	2.05	0.2520	0.2444		
356	64.16	9.65	2.46	2.10	0.2520	0.2978	0.2444	0.2367
370	25.34	14.25	2.48	2.15	0.2444	0.2444	0.2444	0.2367
386	-42.26	17.65	3.70	3.20	0.2367	0.2367	0.2367	0.2367
400	-53.95	16.20	3.91	3.20	0.2367	0.2367	0.2444	0.2367
417	10.52	7.75	2.376	2.30	0.2597	0.2444	0.2520	0.2444
431	38.26	11.75	2.52	2.15	0.2215	0.2367	0.2444	0.2978

Table 11a Response summary for orbits from (days 128 through 431).

Day	Beta Angle (deg)	Roll Jitter Ampl. (arc-s)			Freq. (Hz) \pm 0.01526			
		Max.	Avg.	Med.	85-95 deg.	175-185 deg.	265-275 deg.	345-355 deg.
447	-7.34	13.50	3.55	3.15	0.2520	0.2367	0.2367	0.2367
461	-62.55	21.15	4.54	3.45	0.2367	0.2444	0.2444	0.2444
478	-38.68	18.15	3.83	3.15	0.2444	0.2367	0.2367	0.2367
492	17.22	10.25	1.95	1.60	0.2520	0.2978	0.2444	0.2826
509	29.51	11.8	2.17	1.75	0.2567	0.2444	0.2444	0.2902
523	-19.68	20.30	4.32	3.25	0.2444	0.2367	0.2444	0.2367
537	-64.37	20.2	4.33	3.30	0.2367	0.2367	0.2444	0.2367
551	-23.10	15.45	4.29	3.60	0.2367	0.2367	0.2444	0.2367
568	48.21	12.70	2.62	2.30	0.2520	0.2444	0.2444	0.2444
582	45.88	14.50	2.71	2.25	0.2444	0.2902	0.2444	0.2444
598	-15.24	14.75	3.94	3.45	0.2367	0.2367	0.2520	0.2444
612	-37.21	12.70	3.87	3.30	0.2367	0.2367	0.2444	0.2367
629	15.85	8.45	2.10	1.95	0.2520	0.2444	0.2444	0.2367
632	28.37	14.25	0.59	0.40	-	-	-	-
643	74.08	11.95	2.35	2.10	0.2367	0.2902	0.2367	0.2367
737	-2.01	14.85	3.63	2.95	0.2520	0.2444	0.2215	0.2451

Table 11b Response summary for orbits from (days 447 through 737).

Day	Beta Angle (deg)	Thermal Snap					
		Sunset			Sunrise		
		Solar Array Pos. (deg)	Disp (arc-s)	Duration (s)	Solar Array Pos. (deg)	Disp (arc-s)	Duration (s)
128	9.02	28.1	280.35	52.35	163.2	231.70	42.88
133	25.90	33.1	304.60	49.41	163.2	216.35	41.60
139	38.13	39.7	331.75	55.55	162.3	208.80	43.65
188	-28.82	-	320.05	44.03	-	194.10	48.00
206	47.20	38.87	316.60	48.89	149.9	270.70	44.54
233	2.01	147.5	360.50	48.26	13.2	161.65	43.77
265	2.38	-	-	-	-	-	-
266	6.30	267.2	108.50	42.11	267.2	52.15	80.00
281	64.73	-	-	-	-	-	-
301	20.60	277.5	115.45	63.49	277.5	62.00	59.65
306	0.45	67.0	385.20	48.00	-	-	-
307	-3.38	277.5	131.35	46.47	277.5	67.20	83.20
326	-34.24	106.0	400.45	44.67	342.6	94.00	48.26
339	6.60	75.3	366.10	48.25	-	-	-
356	64.16	16.5	45.85	108.29	127.5	109.15	57.09
370	25.34	82.8	350.85	44.67	212.5	159.25	59.65
386	-42.26	87.8	300.00	48.00	332.7	113.15	47.87
400	-53.95	71.2	234.70	43.90	335.2	89.40	68.48
417	10.52	75.3	396.00	44.03	209.2	159.55	56.19
431	38.26	91.1	296.75	46.85	213.3	121.20	52.61

Table 12a Thermal snap response summary for orbits from (days 128 through 431).

Day	Beta Angle (deg)	Thermal Snap					
		Sunset			Sunrise		
		Solar Array Pos. (deg)	Disp. (arc-s)	Duration (s)	Solar Array Pos. (deg)	Disp. (arc-s)	Duration (s)
447	-7.34	103.5	424.00	54.40	331.9	130.70	66.30
461	-62.55	-	< 25.00	-		< 25.00	-
478	-38.68	91.9	345.05	46.98	331.0	152.85	57.34
492	17.22	84.5	324.70	48.13	216.6	189.70	57.98
509	29.51	87.8	313.6	46.36	217.5	151.5	48.13
523	-19.68	86.95	297.10	65.28	320.2	157.35	48.38
537	-64.37	-	< 25.00	-		< 25.00	
551	-23.10	92.75	354.35	63.35	323.6	143.60	48.25
568	48.21	101.0	282.00	47.87	204.2	91.95	91.26
582	45.88	91.9	314.00	45.06	204.2	114.45	78.59
598	-15.24	98.5	342.30	49.79	327.7	212.30	56.45
612	-37.21	91.1	313.10	50.82	330.2	154.95	56.32
629	15.85	81.15	341.45	48.00	215.0	180.40	48.26
632	28.37	267.2			267.2	108.50	42.11
643	74.08	-	< 25.00	-	-	< 25.00	-
737	-2.01	110.9	425.15	47.49	336.8	129.70	47.62

Table 12b Thermal snap response summary for orbits from (days 447 through 737).

Day	Beta Angle (deg)	Roll Jitter 85-95 deg			Roll Jitter 175-185 deg.			Roll Jitter 265-275 deg.			Roll Jitter 345-355 deg.		
		Ampl. (arc-s)			Ampl. (arc-s)			Ampl. (arc-s)			Ampl. (arc-s)		
		Max.	Avg.	Med.	Max.			Max.	Avg.	Med.	Max.	Avg.	Med.
128	9.02	2.40	0.95	0.90	5.30	2.07	2.00	3.00	0.95	0.80	3.40	1.70	1.65
133	25.90	4.30	1.61	1.50	5.50	1.67	1.55	10.10	4.05	3.65	5.25	2.27	2.10
139	38.13	4.30	1.50	1.35	4.90	1.72	1.65	9.60	3.51	3.72	6.60	2.95	2.70
188	-28.82	-	-	-	-	-	-	-	-	-	-	-	-
206	47.20	4.25	1.51	1.35	5.30	2.12	2.05	5.50	1.60	1.25	5.45	2.37	2.15
233	2.01	5.85	1.51	1.20	6.35	3.24	3.07	3.80	1.16	1.10	5.85	3.10	3.05
265	2.38	-	-	-	-	-	-	-	-	-	-	-	-
266	6.30	-	-	-	-	-	-	-	-	-	-	-	-
281	64.73	-	-	-	-	-	-	-	-	-	-	-	-
301	20.60	-	-	-	-	-	-	-	-	-	-	-	-
306	0.45	1.35	0.46	0.40	-	-	-	-	-	-	-	-	-
307	-3.38	-	-	-	-	-	-	-	-	-	-	-	-
326	-34.24	6.15	2.43	2.15	6.20	3.01	2.95	10.20	3.95	3.55	6.05	2.97	2.95
339	6.60	2.60	0.87	0.75	6.35	2.28	2.00	-	-	-	-	-	-
356	64.16	5.35	1.88	1.70	3.75	1.60	1.50	5.85	1.87	1.70	5.05	2.21	2.10
370	25.34	5.55	2.15	2.10	3.20	1.24	1.20	4.50	1.64	1.60	7.00	2.83	2.65
386	-42.26	32.10 ¹	9.66	7.10	8.05	3.91	3.75	8.10	3.58	3.35	6.40	3.02	2.90
400	-53.95	12.05	6.01	5.80	8.00	3.64	3.50	8.15	3.32	3.05	5.15	2.25	2.20
417	10.52	3.05	0.70	0.60	5.10	2.05	1.95	4.15	1.38	1.22	5.25	2.38	2.40
431	38.26	31.45 ¹	7.17	2.00	5.65	1.93	1.70	6.05	1.84	1.50	6.70	2.30	2.15

Table 13a Roll jitter variation with solar array orientation (days 128 through 431).

¹ During Thermal Snap

Day	Beta Angle (deg)	Roll Jitter 85-95 deg			Roll Jitter 175-185 deg			Roll Jitter 265-275 deg			Roll Jitter 345-355 deg		
		Max.	Ampl. (arc-s) Avg.	Med.	Max.	Ampl. (arc-s) Avg.	Med.	Max.	Ampl. (arc-s) Avg.	Med.	Max.	Ampl. (arc-s) Avg.	Med.
447	-7.34	3.00	1.18	1.05	7.25	2.84	2.55	5.95	2.16	1.80	5.95	3.21	3.20
461	-62.55	15.65	8.18	7.85	5.80	2.32	2.20	4.90	1.93	1.82	7.70	2.99	2.75
478	-38.68	32.9	9.00	5.00	8.65	3.29	3.00	7.30	3.17	3.10	5.15	2.30	2.25
492	17.22	27.15	4.33	2.00	3.35	1.18	1.15	7.35	2.39	2.05	4.65	2.07	1.95
509	29.51	34.10	7.94	2.65	3.00	1.47	1.45	5.70	3.00	3.00	8.00	3.64	3.35
523	-19.68	27.1	7.11	3.60	6.55	3.03	2.90	8.40	3.07	2.75	6.60	2.47	2.30
537	-64.37	13.75	5.02	4.75	6.35	3.21	3.05	13.25	4.90	4.65	8.70	4.10	3.95
551	-23.10	33.10	8.59	4.85	4.60	2.18	2.10	10.75	4.28	4.15	6.30	3.22	3.10
568	48.21	5.75	1.47	1.30	4.90	1.36	1.25	5.75	2.09	1.85	6.20	2.20	2.00
582	45.88	27.60	9.07	5.75	5.95	1.75	1.50	5.80	2.50	2.35	6.00	2.51	2.45
598	-15.24	6.10	1.99	1.75	5.90	3.09	3.05	6.25	2.11	1.90	6.15	3.21	3.20
612	-37.21	28.90	8.75	5.25	6.65	2.94	2.85	10.35	4.37	4.10	5.65	3.13	3.05
629	15.85	5.00	1.59	1.45	3.10	1.58	1.55	6.75	2.70	2.70	5.95	3.20	3.20
632	28.37	-	-	-	-	-	-	-	-	-	-	-	-
643	74.08	8.65	2.90	2.60	6.70	2.74	2.60	4.55	1.80	1.70	5.90	2.90	2.95
737	-2.01	2.850	1.112	1.000	8.400	4.142	4.000	2.65	0.68	0.60	5.30	3.21	3.10

Table 13b Roll jitter variation with solar array orientation (days 447 through 737).

Tip Mass m_{tip}	Tip Inertia I_{tip}	Characteristic Equation
0	0	Free-Free $1 - \cos(\lambda\ell)\cosh(\lambda\ell) = 0$
∞	∞	Clamped-Free $1 + \cos(\lambda\ell)\cosh(\lambda\ell) = 0$
∞	0	Pinned-Free $\tan(\lambda\ell) - \tanh(\lambda\ell) = 0$
0	∞	Sliding-Free $\tan(\lambda\ell) + \tanh(\lambda\ell) = 0$
$0 \leq m_{tip} < \infty$	$0 \leq I_{tip} < \infty$	$\lambda^4 [1 - \cos(\lambda\ell)\cosh(\lambda\ell)]$ $+ \lambda \left(\frac{m_{tip}\omega^2}{EI} \right) [\sin(\lambda\ell)\cosh(\lambda\ell) - \cos(\lambda\ell)\sinh(\lambda\ell)]$ $+ \lambda^3 \left(\frac{I_{tip}\omega^2}{EI} \right) [\cos(\lambda\ell)\sinh(\lambda\ell) + \sin(\lambda\ell)\cosh(\lambda\ell)]$ $+ I_{tip}m_{tip} \left(\frac{\omega^2}{EI} \right)^2 [1 + \cos(\lambda\ell)\cosh(\lambda\ell)] = 0$

Table 14 Characteristic Equations Resulting From Different Tip Mass and Tip Inertia Boundary Conditions.

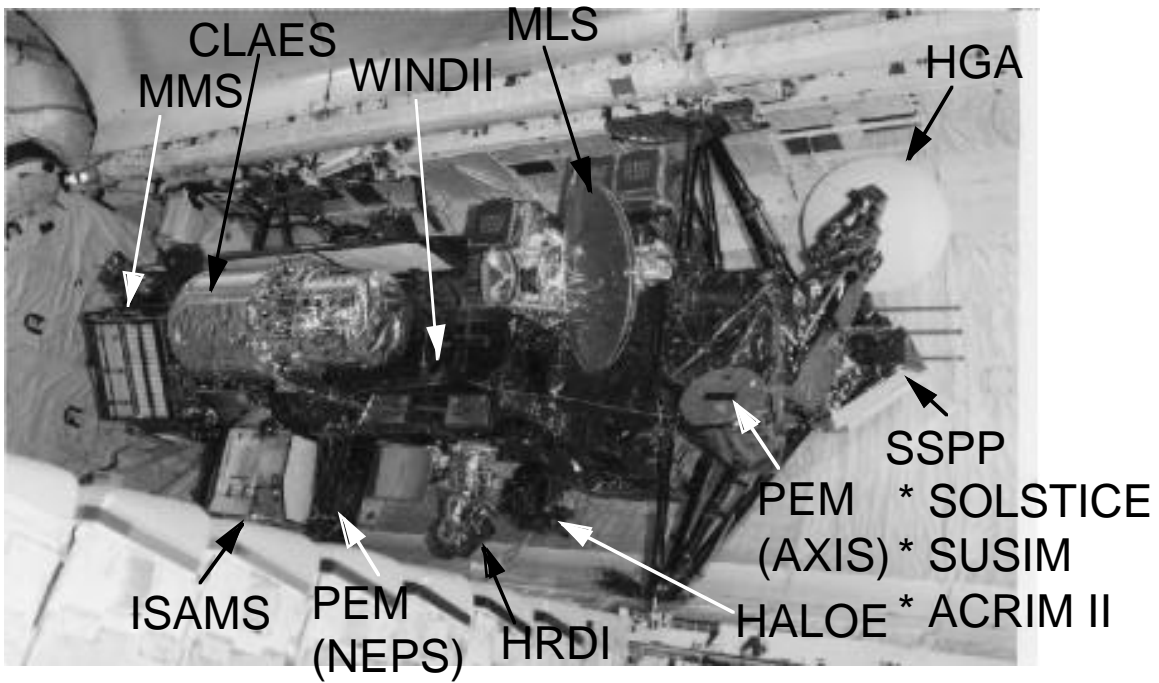


Fig. 1 The Upper Atmosphere Research Satellite in the bay of the Space Shuttle Discovery (STS-48).

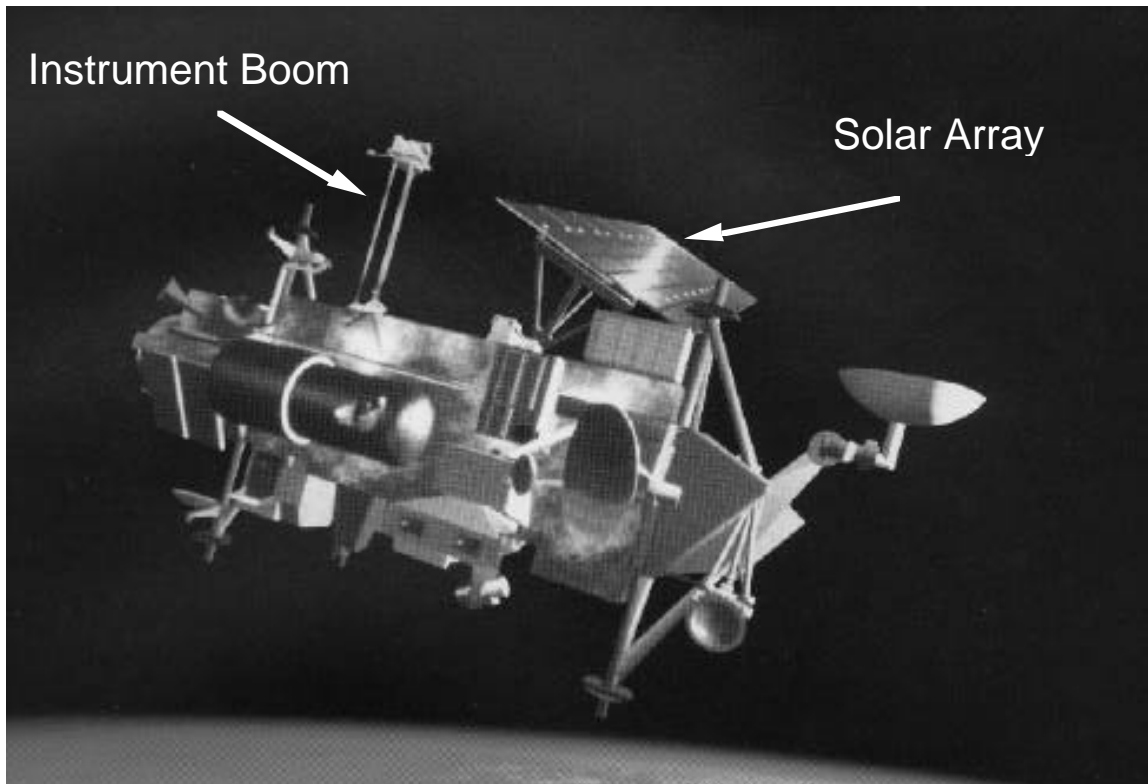
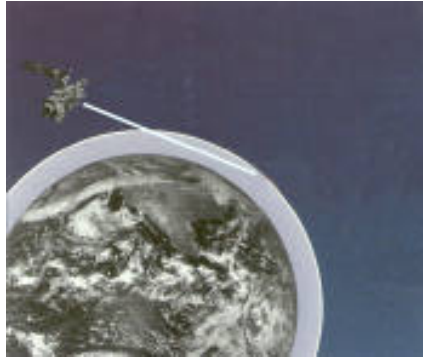


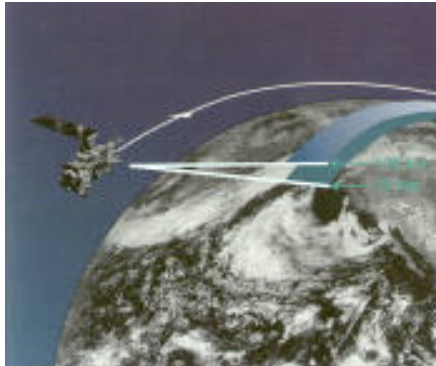
Fig. 2 Artist concept of the Upper Atmosphere Research Satellite on orbit.



a) Emission measurements: CLAES, WINDII and ISAMS.



b) Solar and Stellar Pointing: SOLSTICE, SUSIM and ACRIM II.



c) Limb-Viewing: MLS and HRDI.



d) Occultation: HALOE.

Particle Environment: PEM

Fig. 3 Science measurement types taken by UARS.

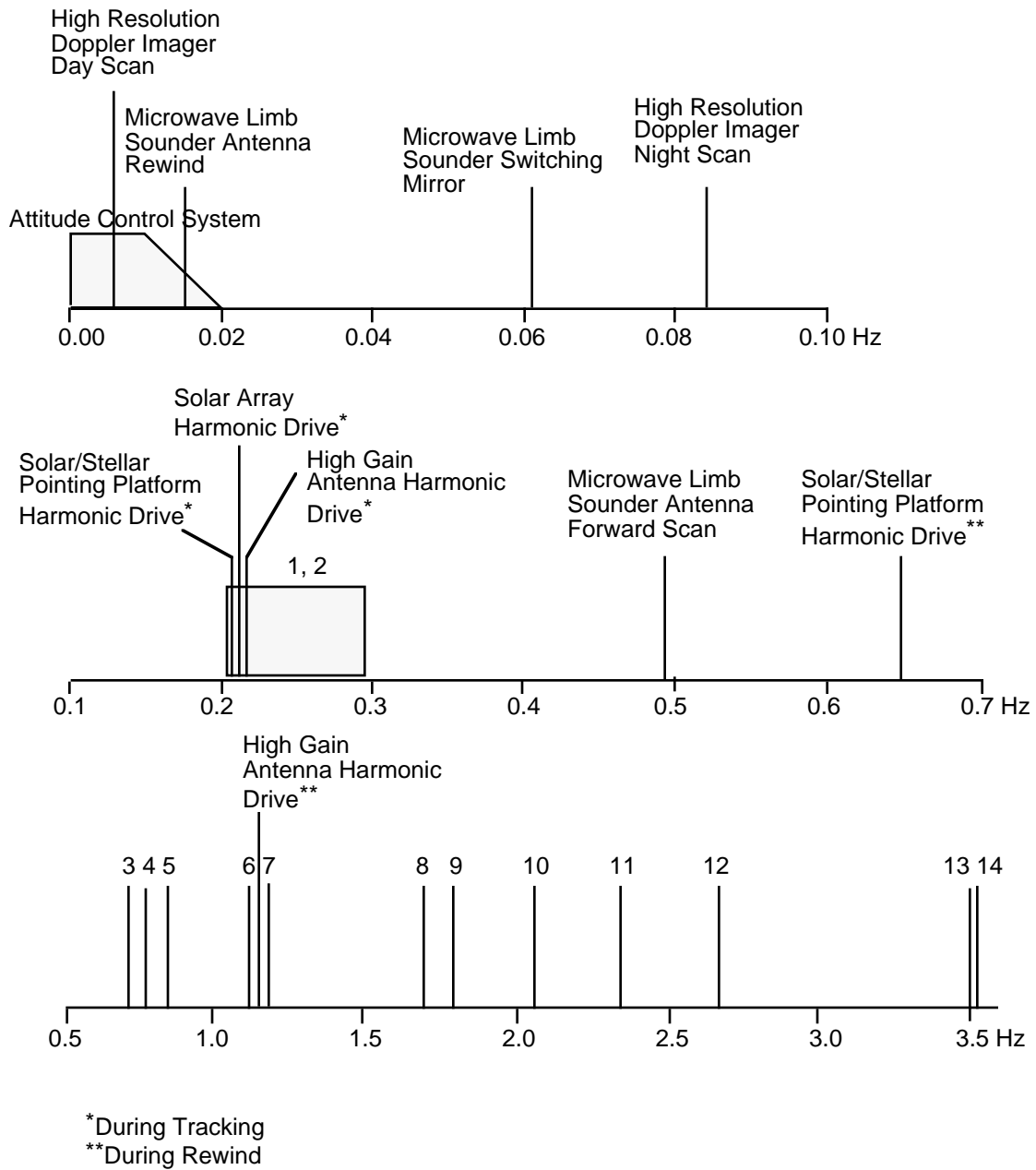


Fig. 4 UARS structural and instrument frequencies below 4.0 Hz.

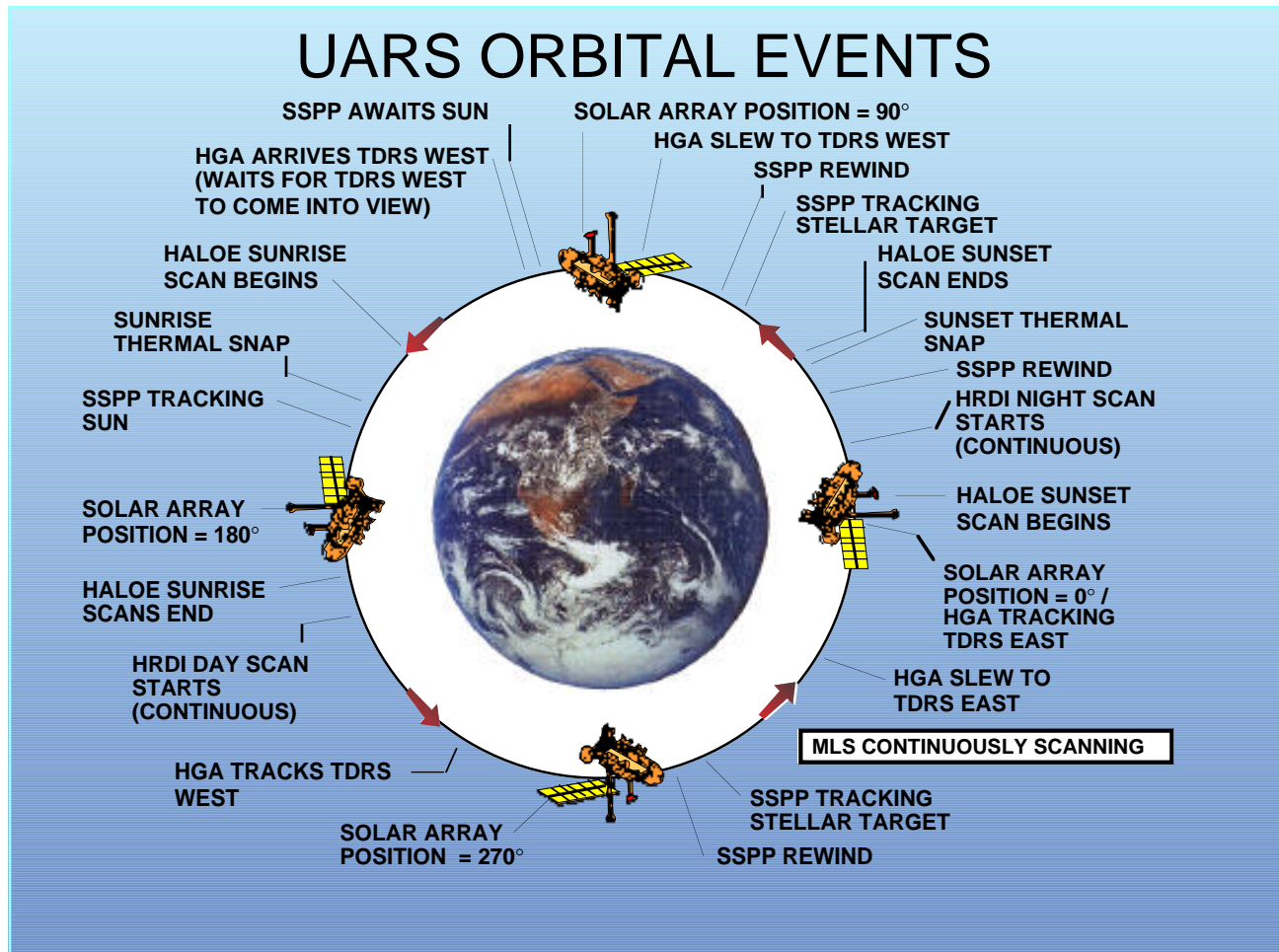


Fig. 5 Orbital events during the first orbit of January 28, 1992.

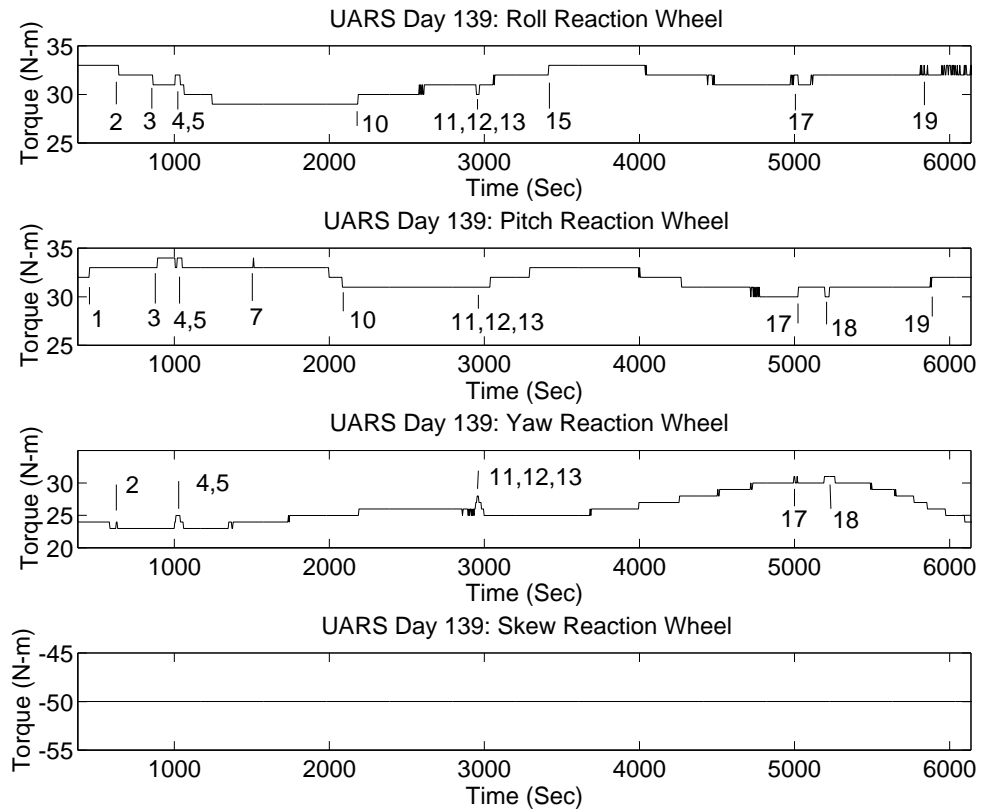


Fig. 6 Reaction wheel torque during the first orbit on January 28, 1992.

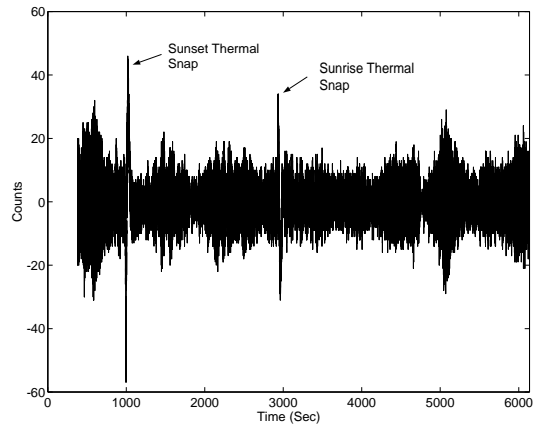


Fig. 7a Roll rate gyro counts.

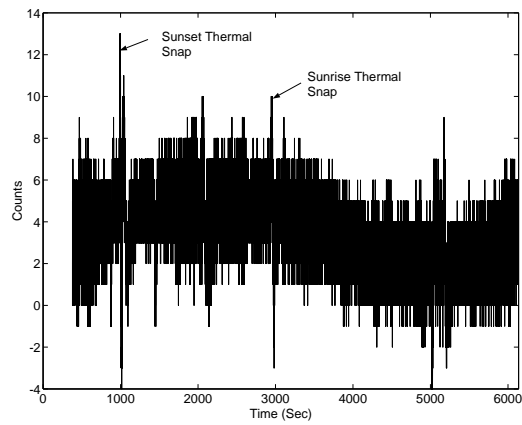


Fig. 7b Pitch rate gyro counts.

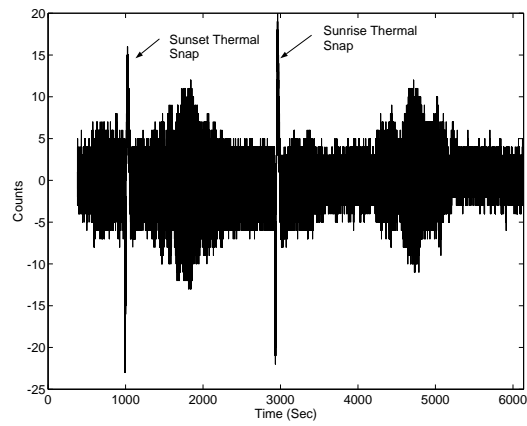


Fig. 7c Yaw rate gyro counts.

Fig. 7 UARS attitude rate during first orbit on January 28, 1997.

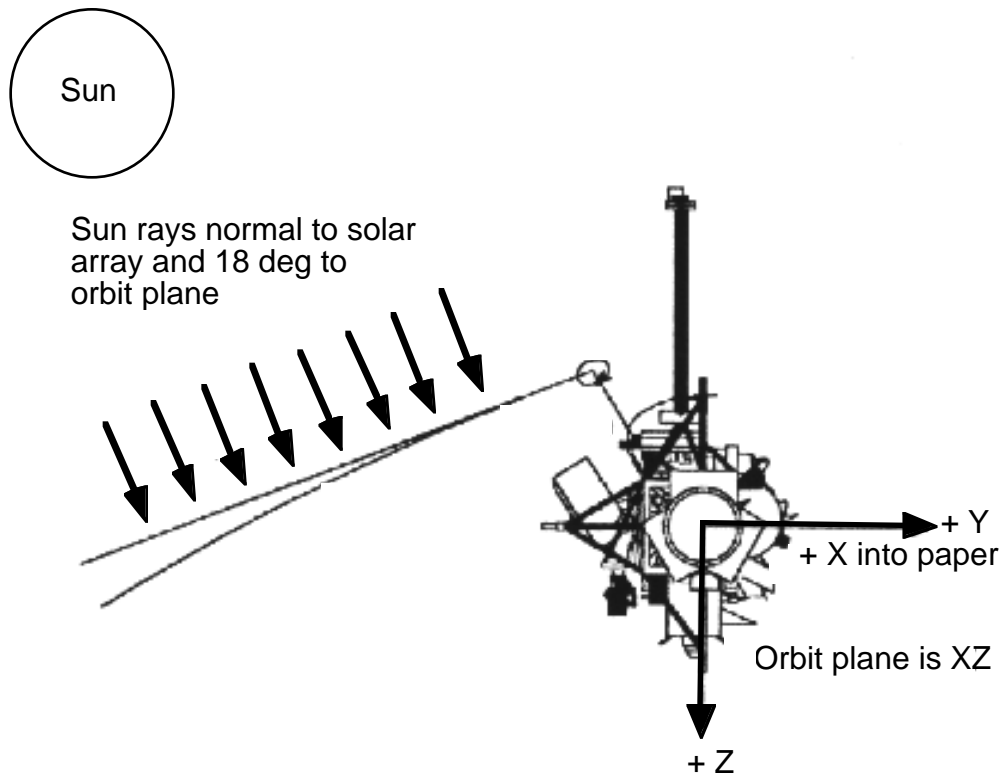


Fig. 8 Bending of UARS solar array at orbital terminator crossing

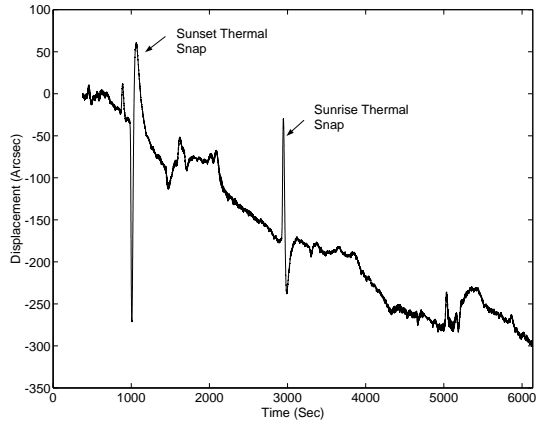


Fig. 9a Roll attitude.

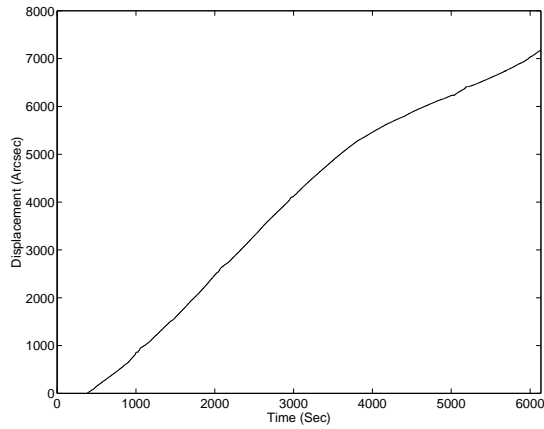


Fig. 9b Pitch attitude.

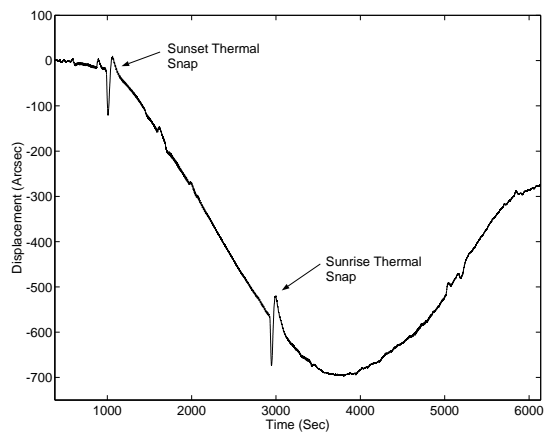


Fig. 9c Yaw attitude.

Fig. 9 UARS attitude during first orbit on January 28, 1997.

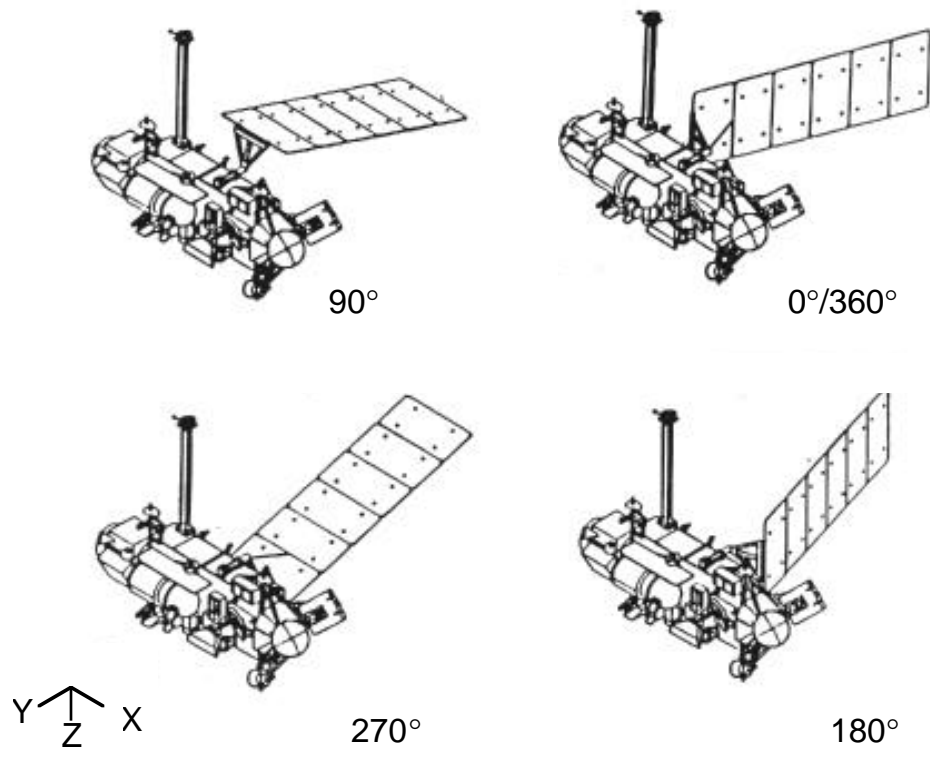


Fig. 10 UARS solar array positions.

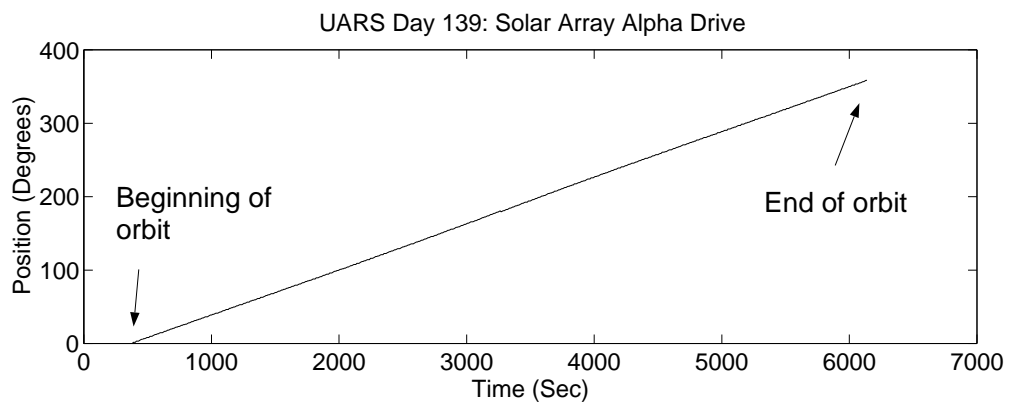


Fig. 11 Solar array position history for the first orbit of January 28, 1992.

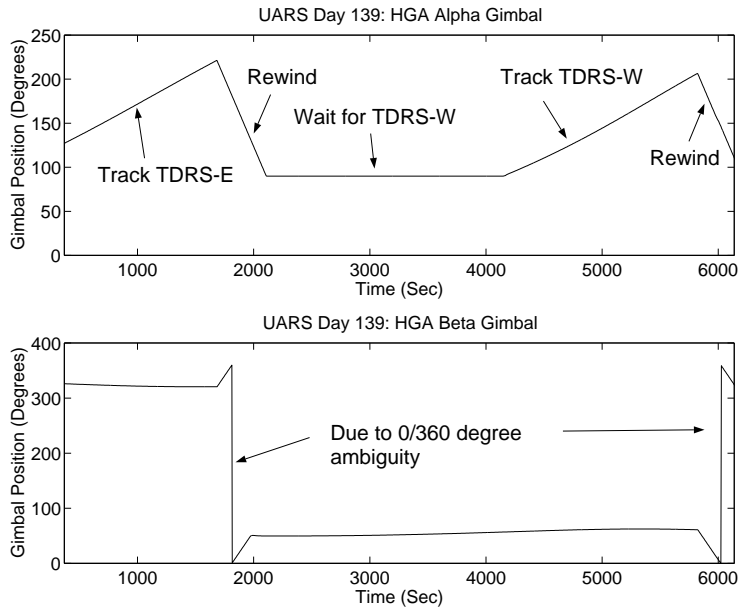


Fig. 12 High gain antenna azimuth and elevation gimbal rotation during the first orbit of January 28, 1992.

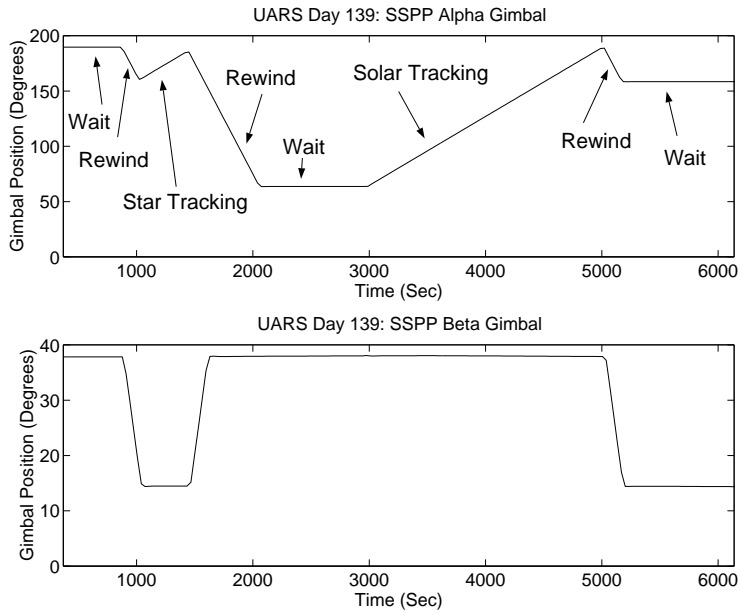


Fig. 13 Solar Stellar Pointing Platform azimuth and elevation gimbal rotation during the first orbit of January 28, 1992.

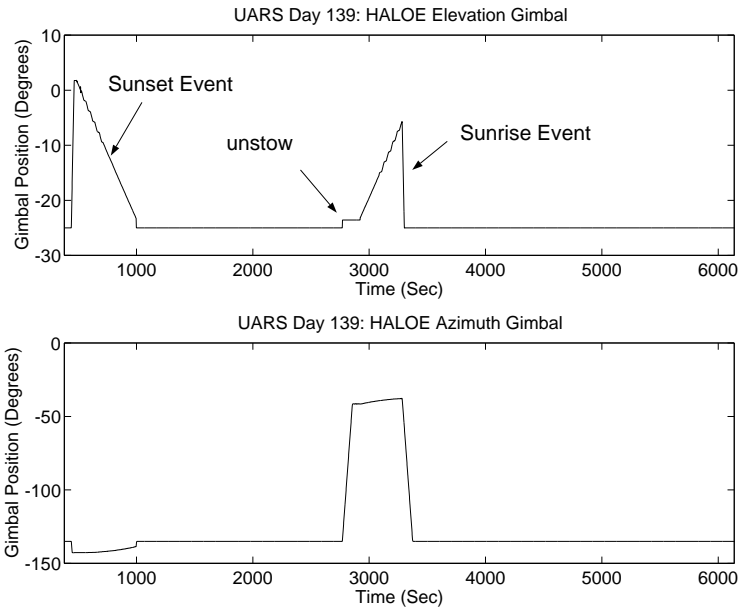


Fig. 14 Halogen Occultation Experiment azimuth and elevation gimbal rotation during the first orbit of January 28, 1992.

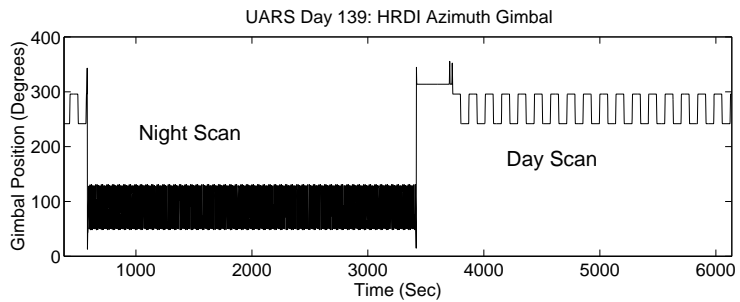


Fig. 15 High Resolution Doppler Imager azimuth and elevation gimbal rotation during the first orbit of January 28, 1992.

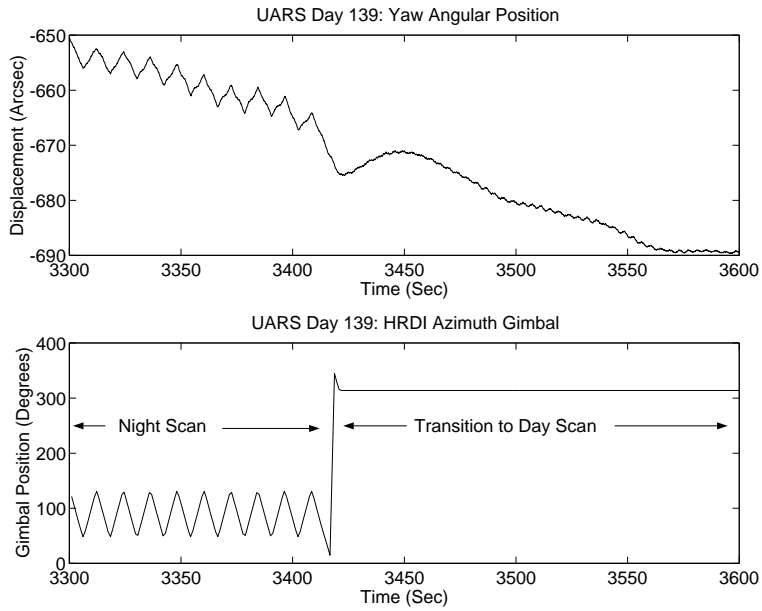


Fig. 16 The effect of the High Resolution Doppler Imager telescope on yaw attitude during the transition from night scanning to day scanning.

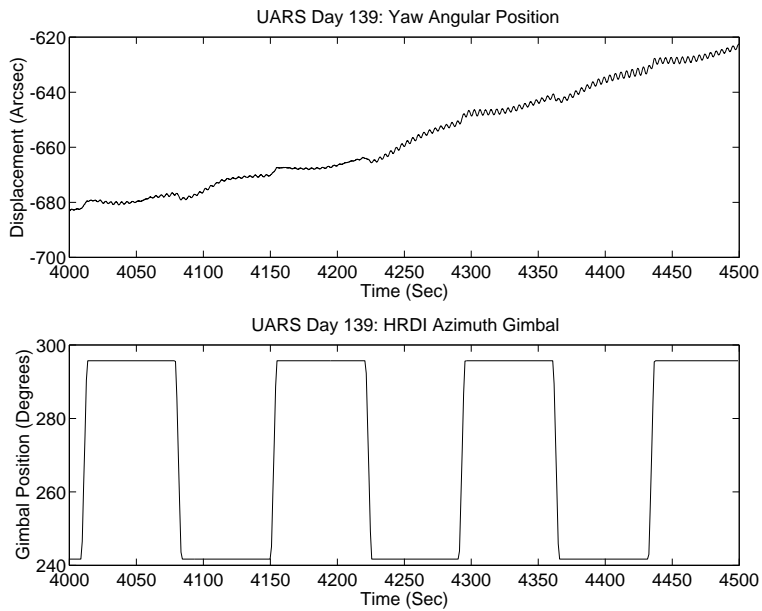


Fig. 17 The effect of the High Resolution Doppler Imager telescope on yaw attitude during day scanning.

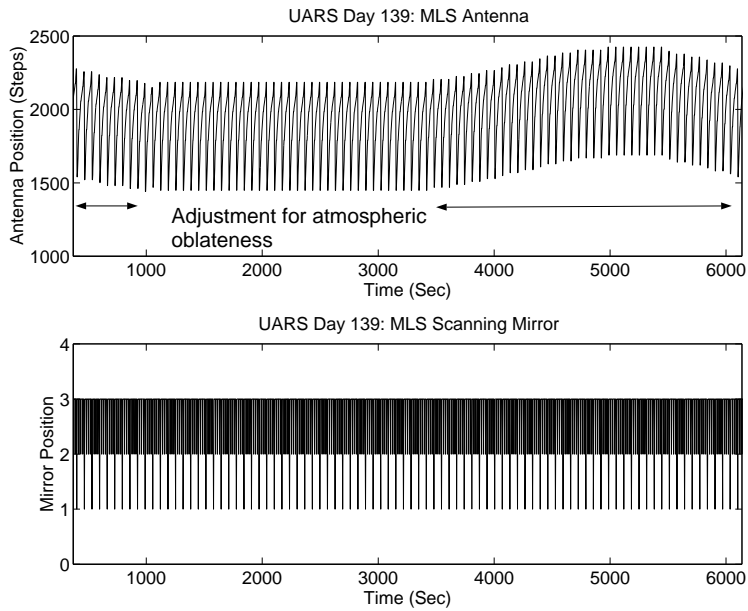


Fig. 18 Microwave Limb Sounder antenna stepping history and switching mirror history during the first orbit of January 28, 1992.

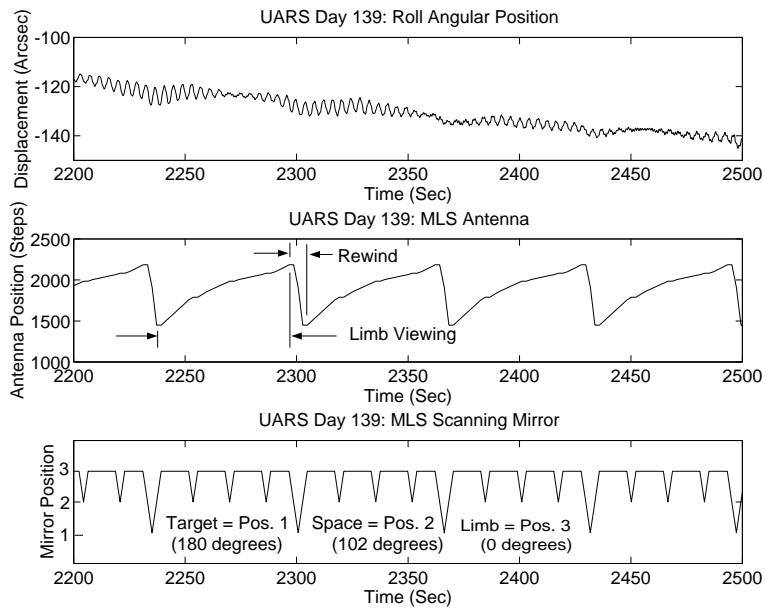


Fig. 19 UARS roll attitude, Microwave Limb Sounder antenna stepping history and switching mirror history during the first orbit of January 28, 1992.

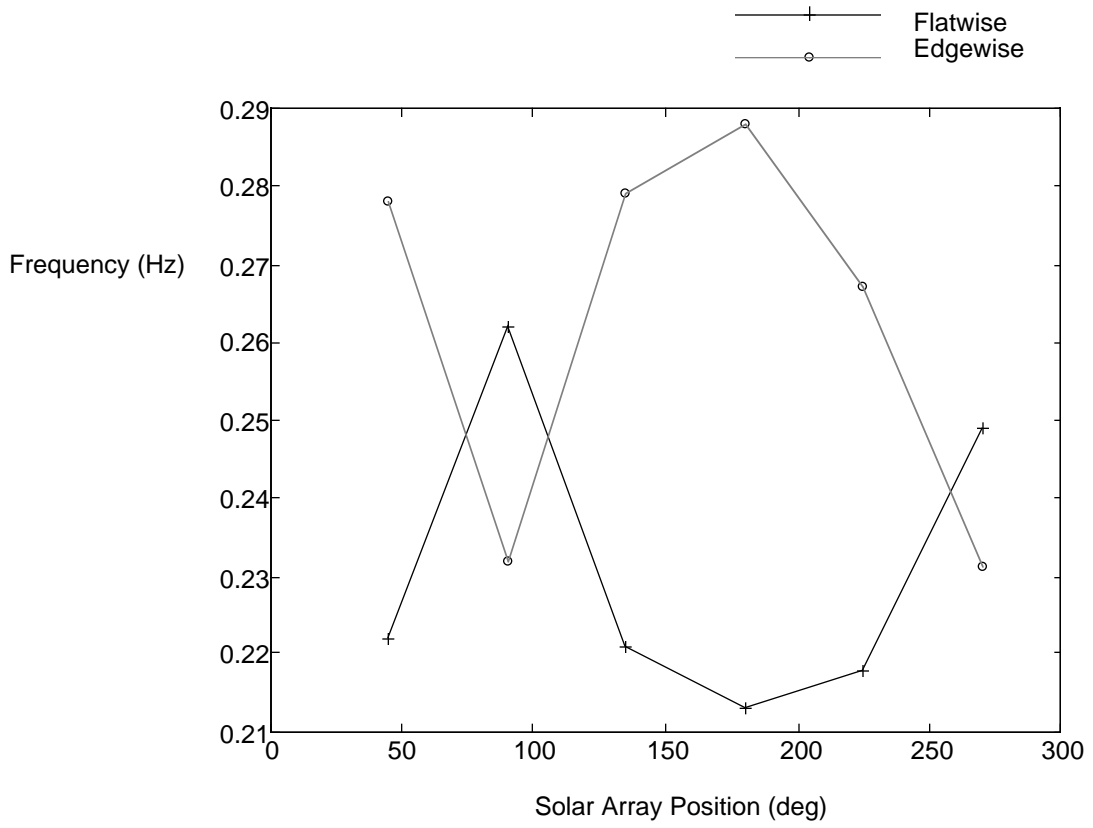


Fig. 20 Solar array edgewise and flatwise fundamental frequencies at various solar array positions.

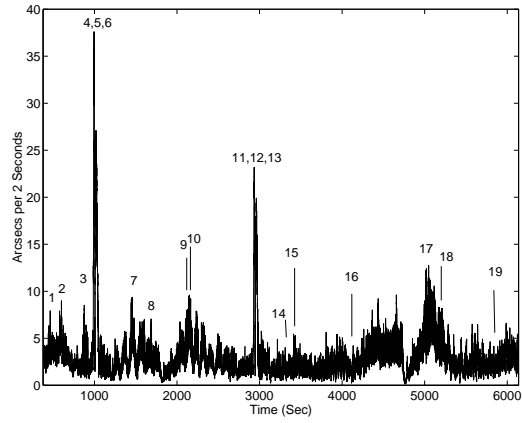


Fig. 21a Roll jitter.

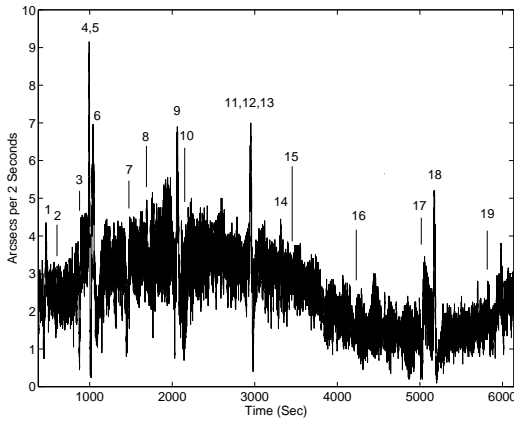


Fig. 21b Pitch jitter.

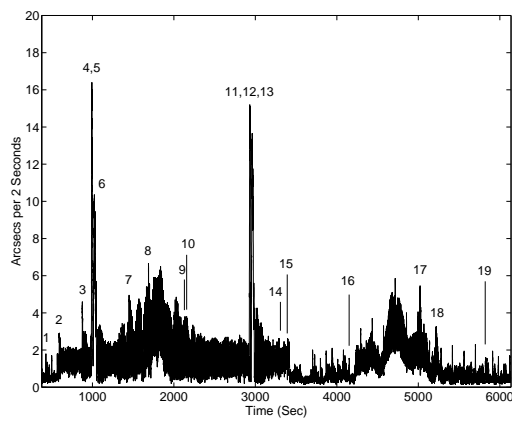
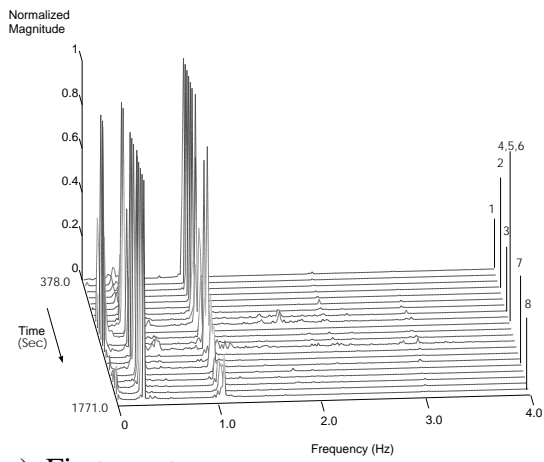
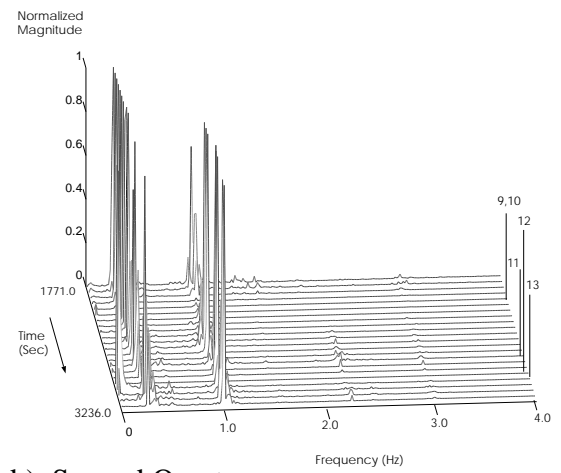


Fig. 21c Yaw jitter.

Fig. 21 UARS attitude rate during first orbit on January 28, 1997.

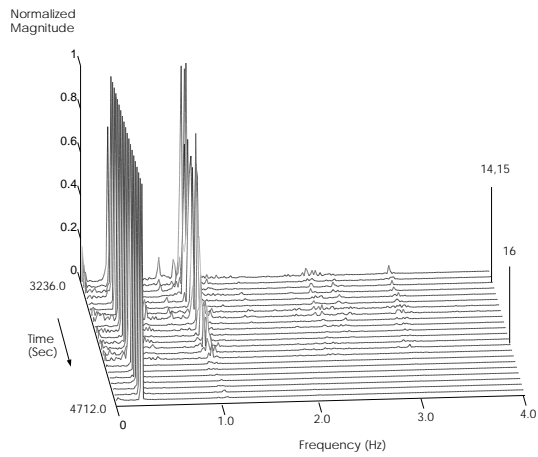


a) First quarter

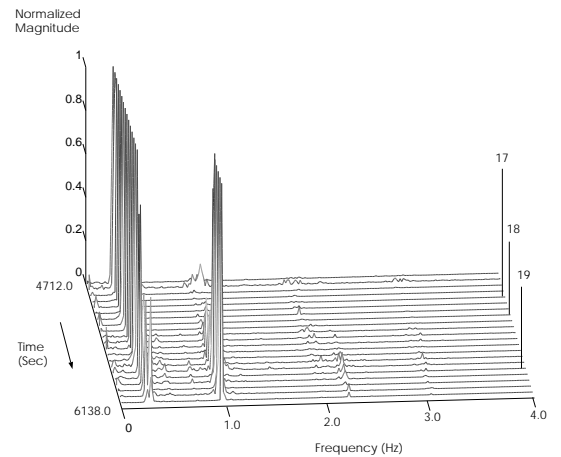


b) Second Quarter

Fig. 22 Spectral history of UARS frequencies below 4.0 Hz during first and second quarter of first orbits on January 28, 1992.



a) Third quarter



b) Fourth Quarter

Fig. 23 Spectral history of UARS frequencies below 4.0 Hz during third and fourth quarter of first orbits on January 28, 1992.

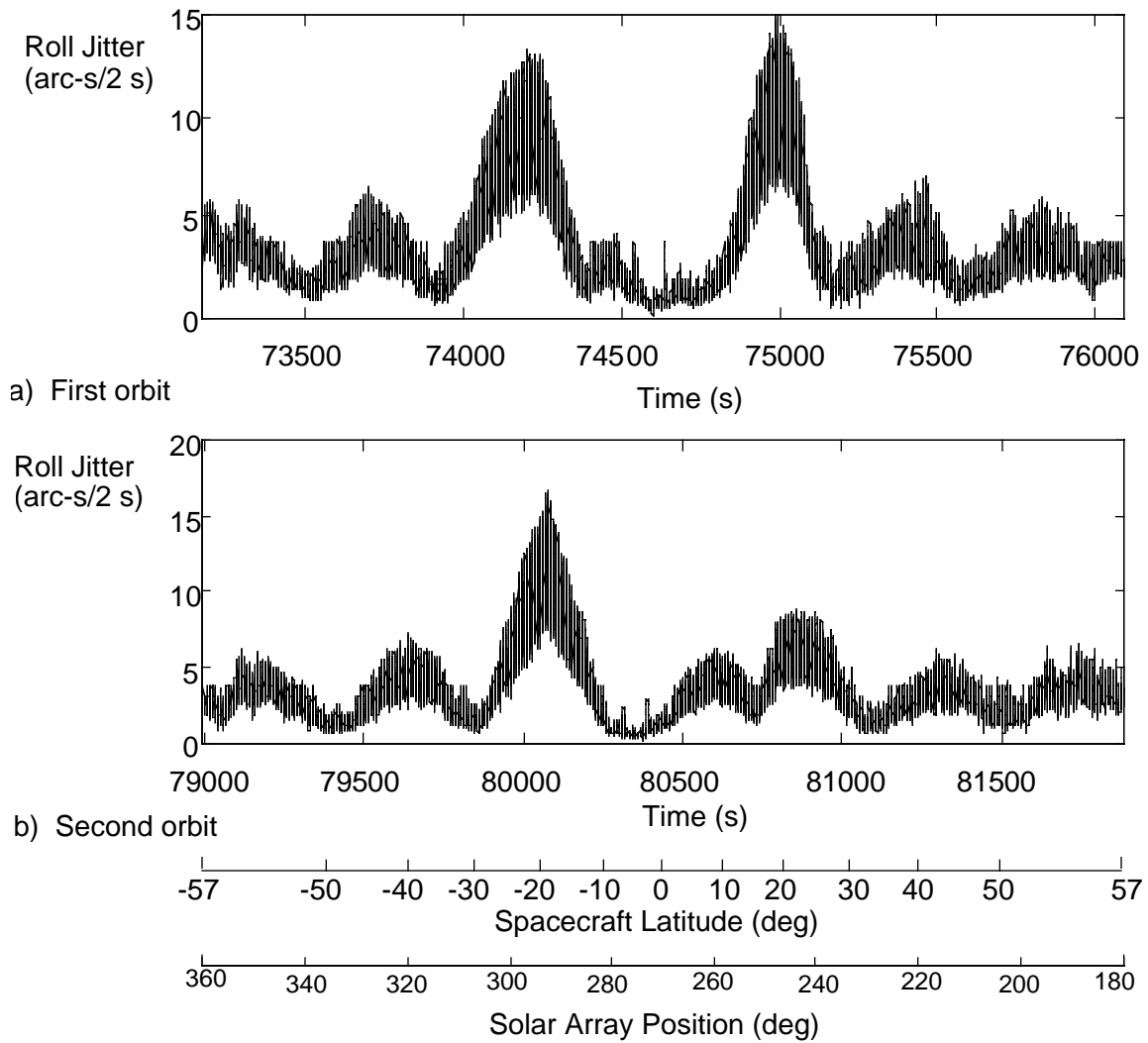


Fig. 24 Roll jitter at latitudes 57°S to 57°N during ascending part of both orbits in the experiment.

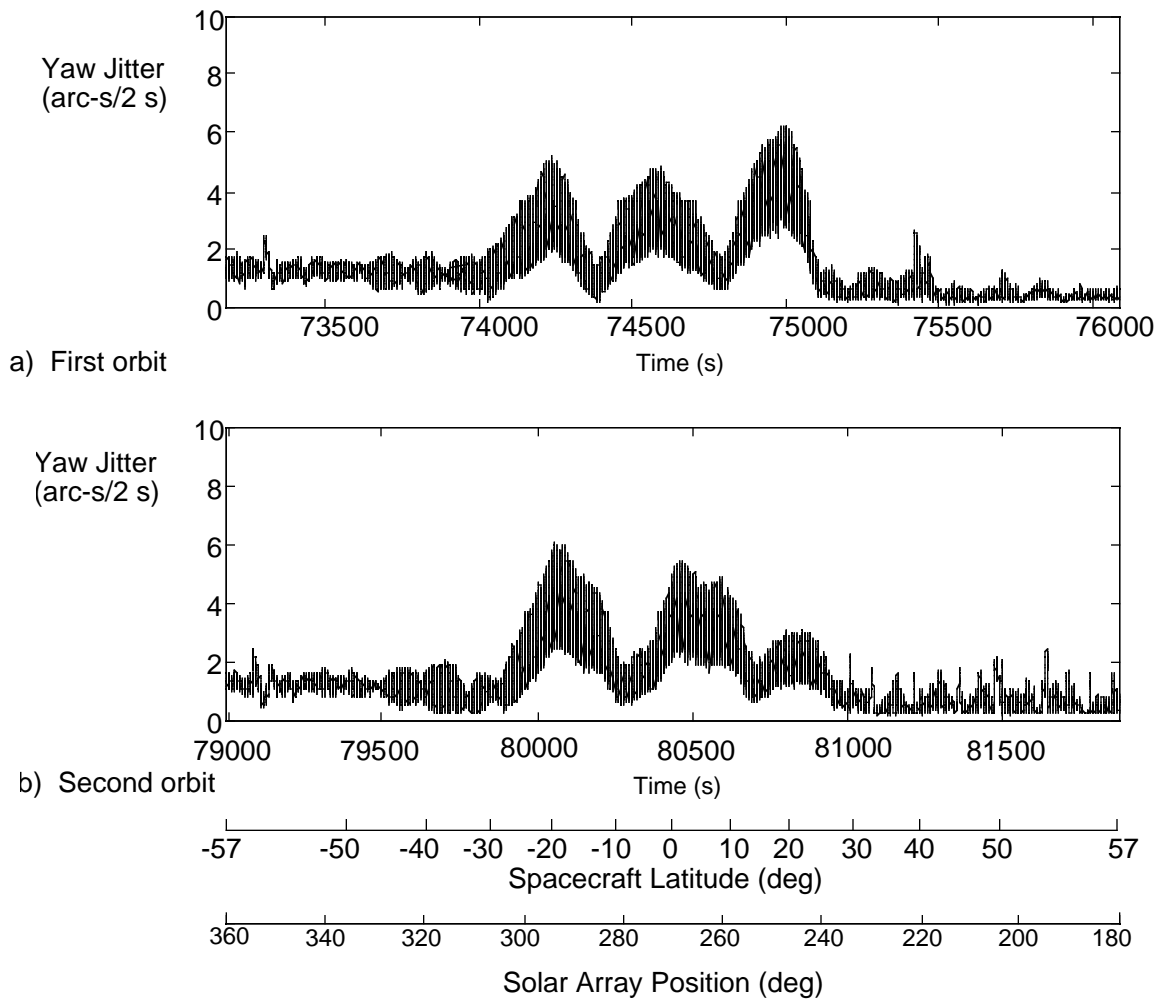
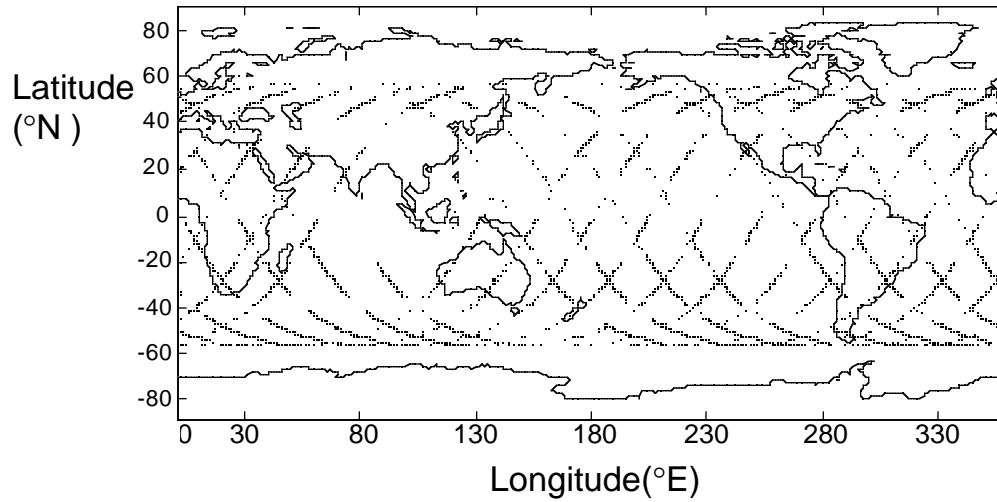
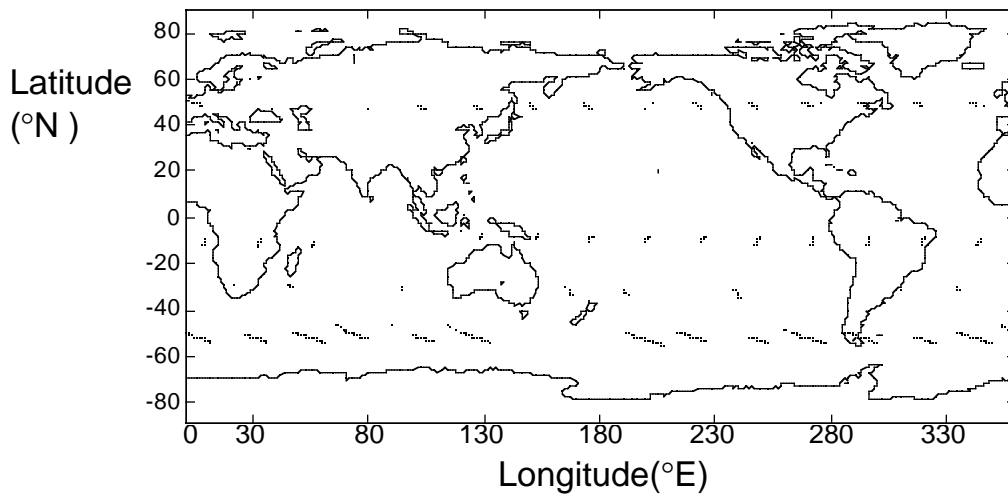


Fig. 25 Yaw jitter at latitudes 57°S to 57°N during ascending part of both orbits in the experiment.

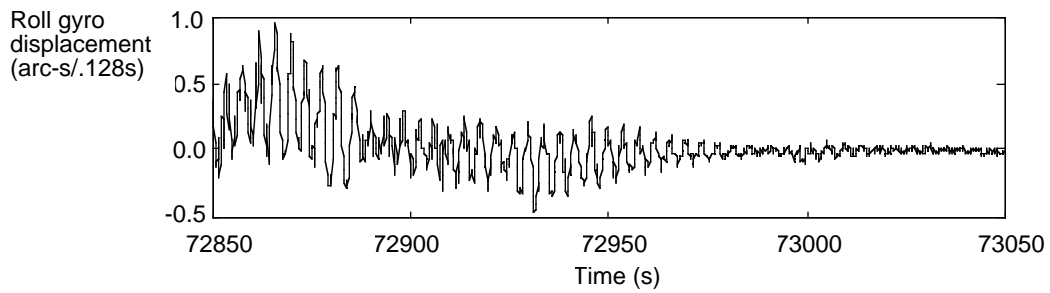


a) Roll jitter exceeding 4 arc-s over a 2 s interval

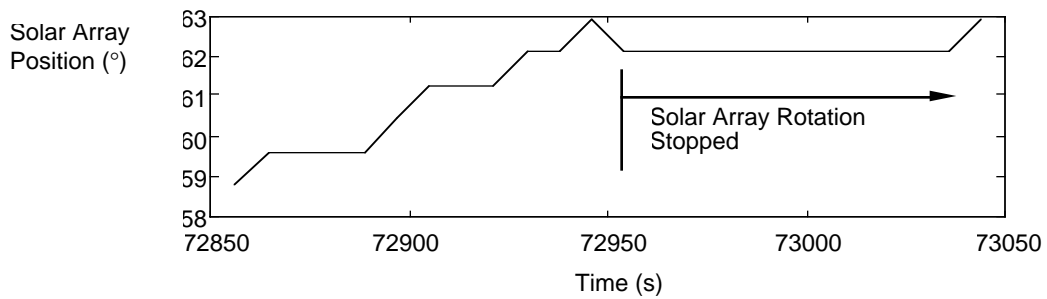


b) Roll jitter exceeding 10 arc-s over a 2 s interval

Fig. 26 Ground track of roll jitter on Jan. 22, 1992.

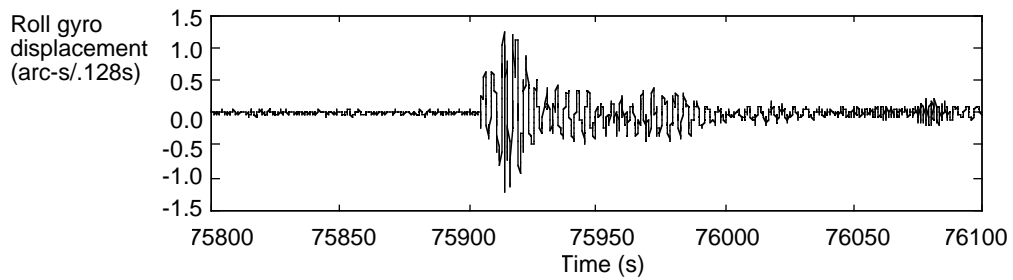


a) UARS roll response.

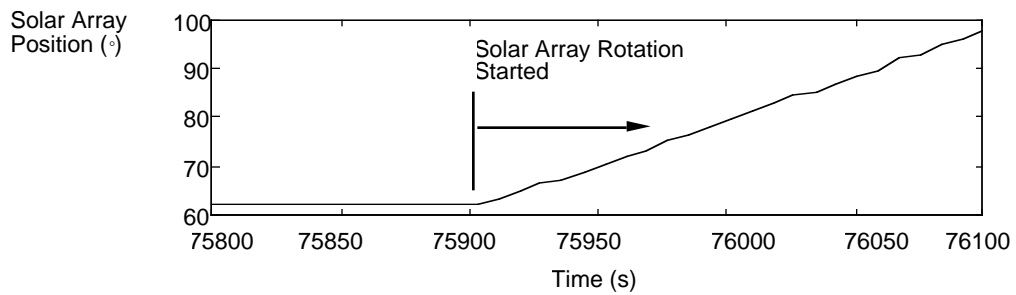


b) Solar array position.

Fig. 27 UARS roll response as the solar array rotation stopped.

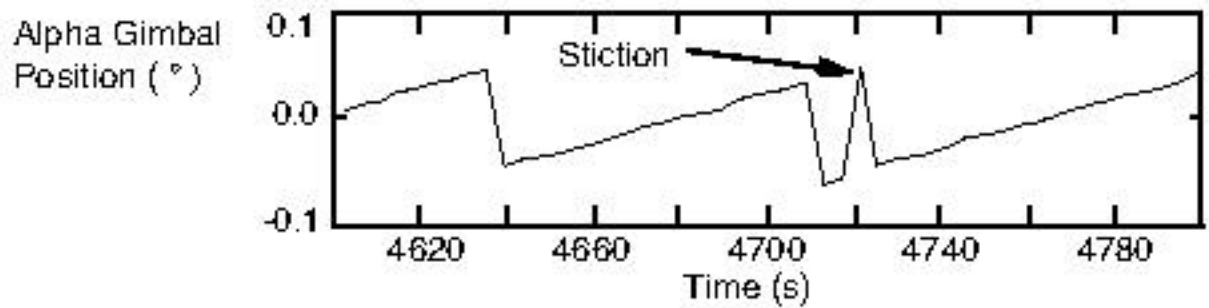


a) UARS roll response.

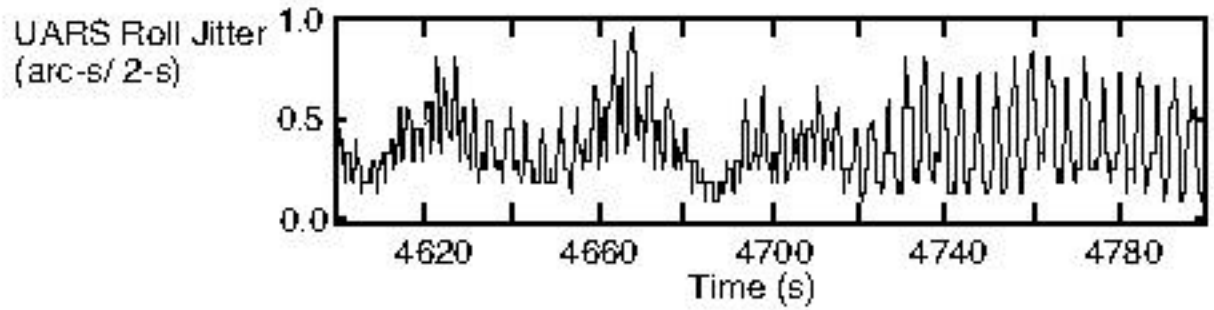


b) Solar array position.

Fig. 28 UARS roll response as the solar array rotation started.



a) High gain antenna alpha gimbal position (with rotation removed) during Tracking and Data Relay Satellite targeting



b) UARS roll jitter response during high gain antenna targeting

Fig. 29 UARS roll jitter response during high gain antenna targeting and alpha gimbal stiction.

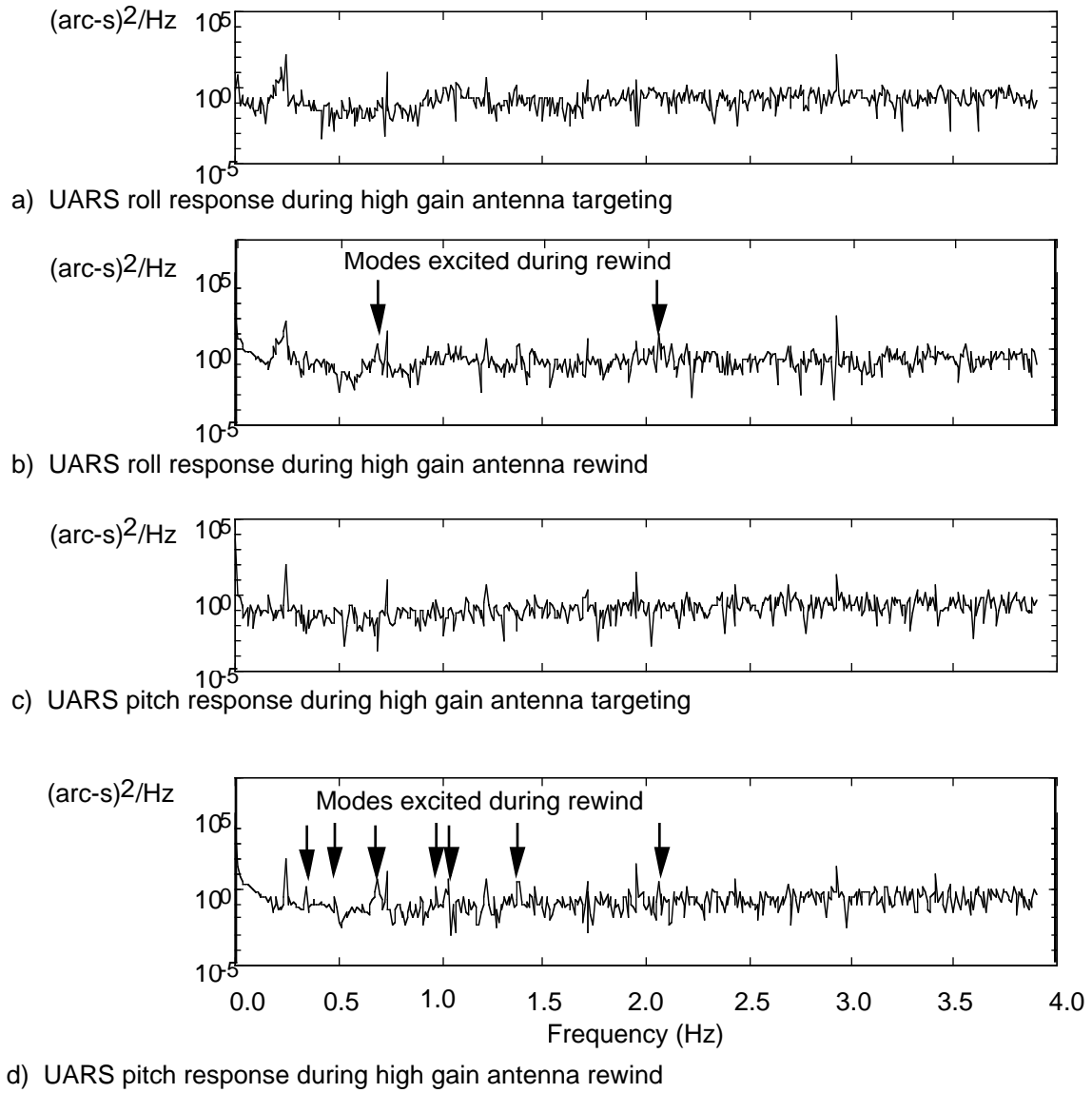
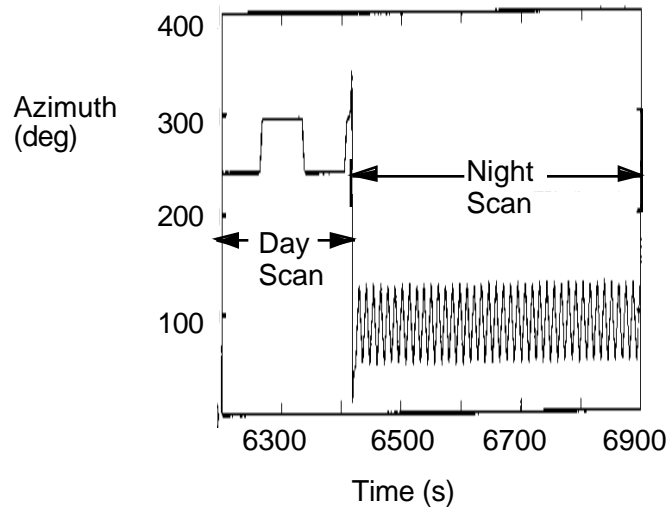
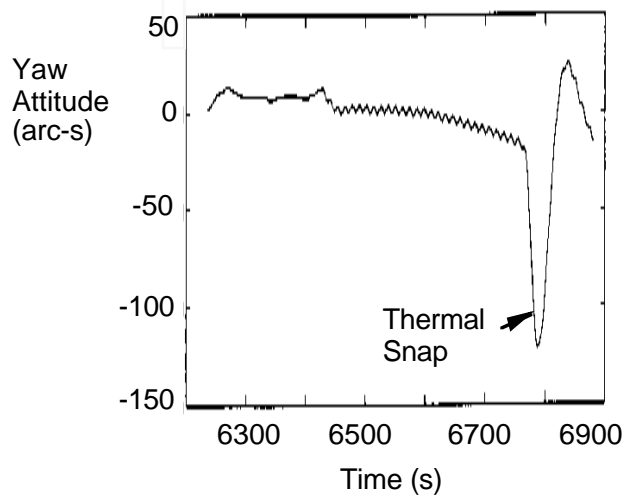


Fig. 30 UARS attitude response during high gain antenna targeting and rewind.

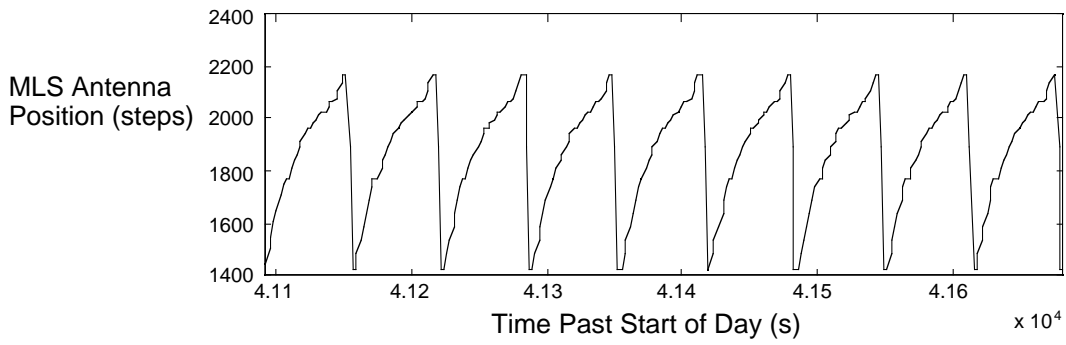


a) HRDI azimuth gimbal position

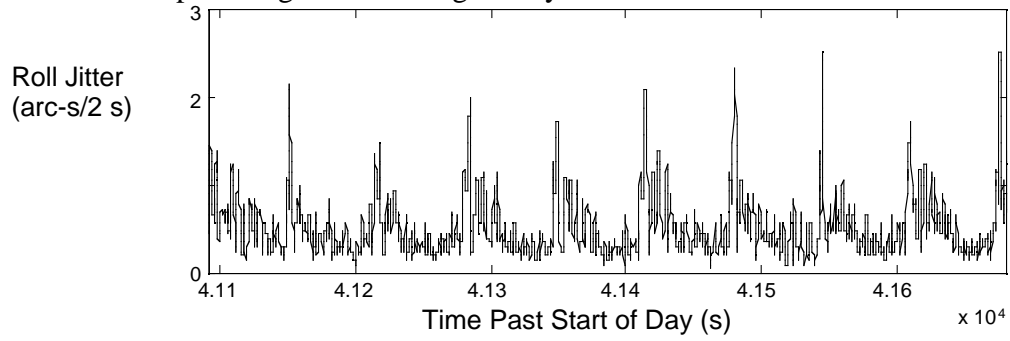


b) Spacecraft yaw attitude

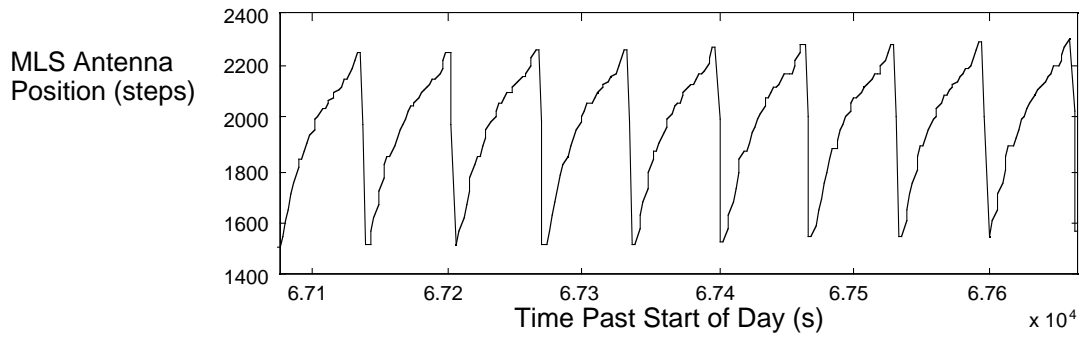
Fig. 31 Yaw response to HRDI night scan, day 139.



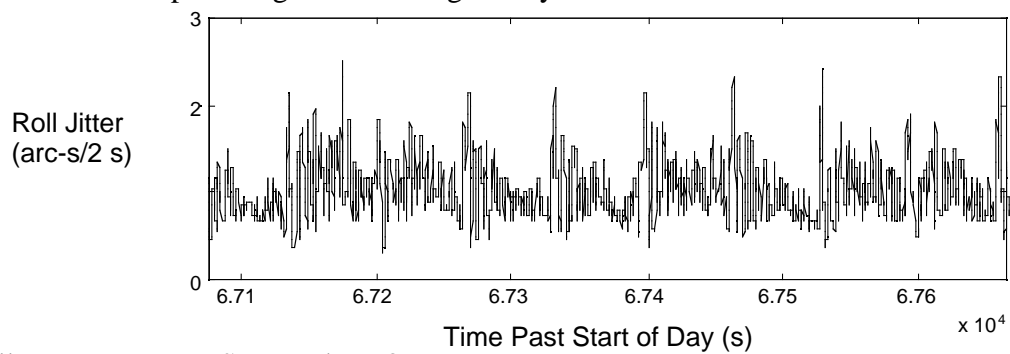
a) MLS antenna steps during limb viewing on day 301



b) Roll response to MLS scan, day 301



c) MLS antenna steps during limb viewing on day 737



d) Roll response to MLS scan, day 737

Fig. 32 Spacecraft roll response to MLS limb viewing.

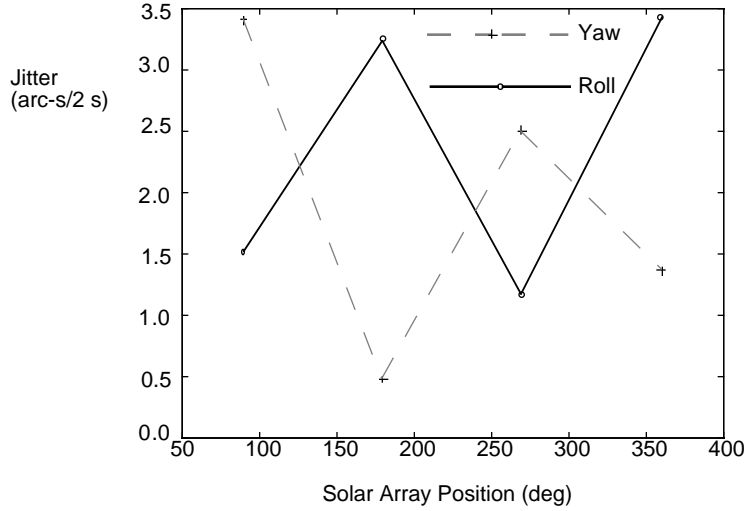
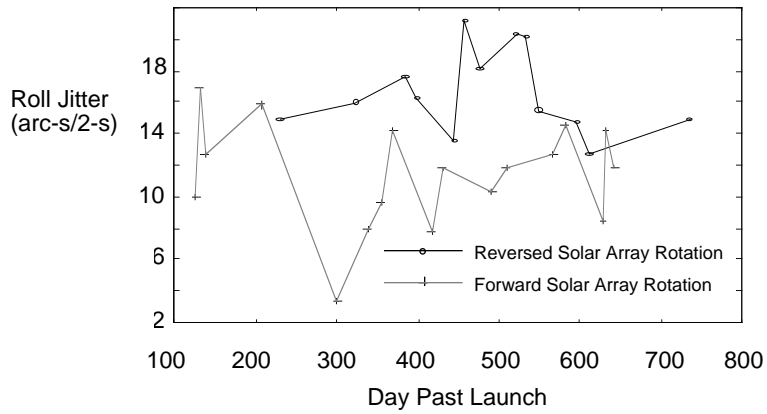
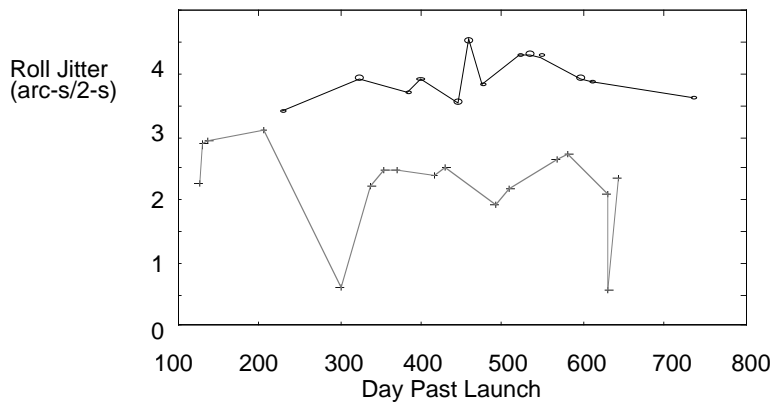


Fig. 33 Variation of median roll and yaw jitter with solar array position (day 233).

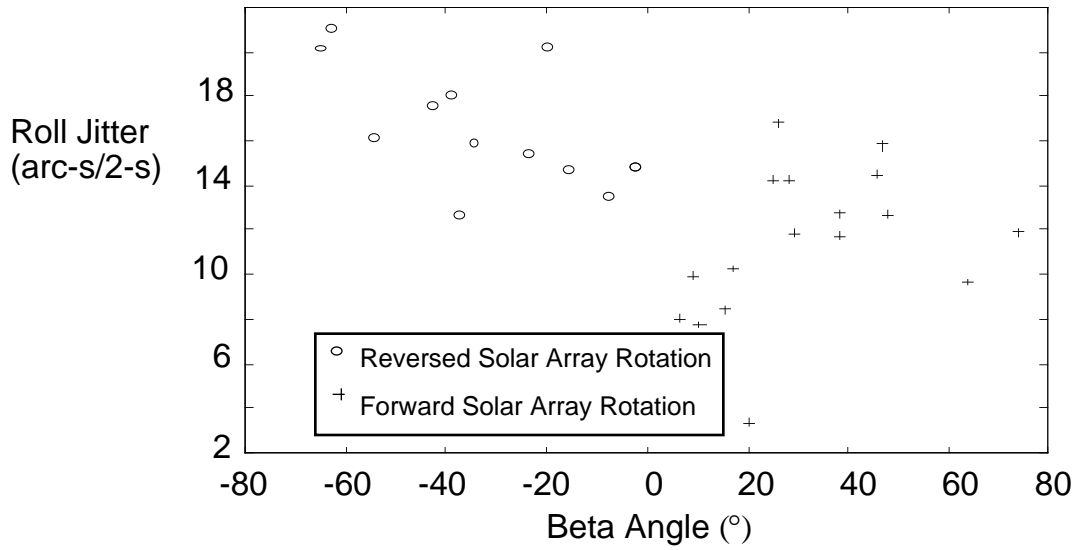


a) Maximum roll jitter

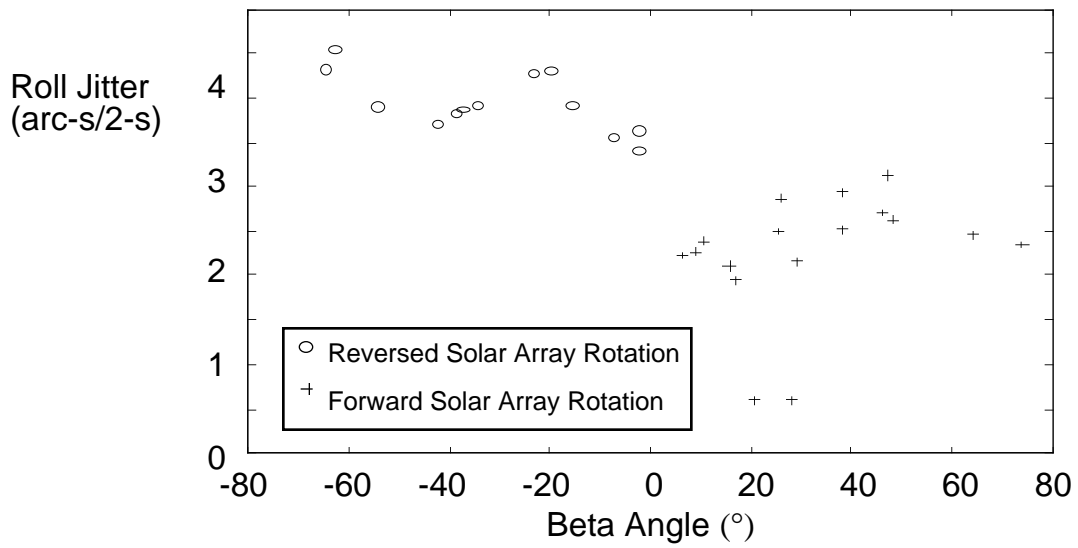


b) Average roll jitter

Fig. 34 Spacecraft roll jitter for days 128 through 737 past launch. Jitter due to thermal snap is excluded.



a) Maximum roll jitter



b) Average roll jitter

Fig. 35 Spacecraft roll jitter variation with Beta angle for days 128 through 737 past launch.

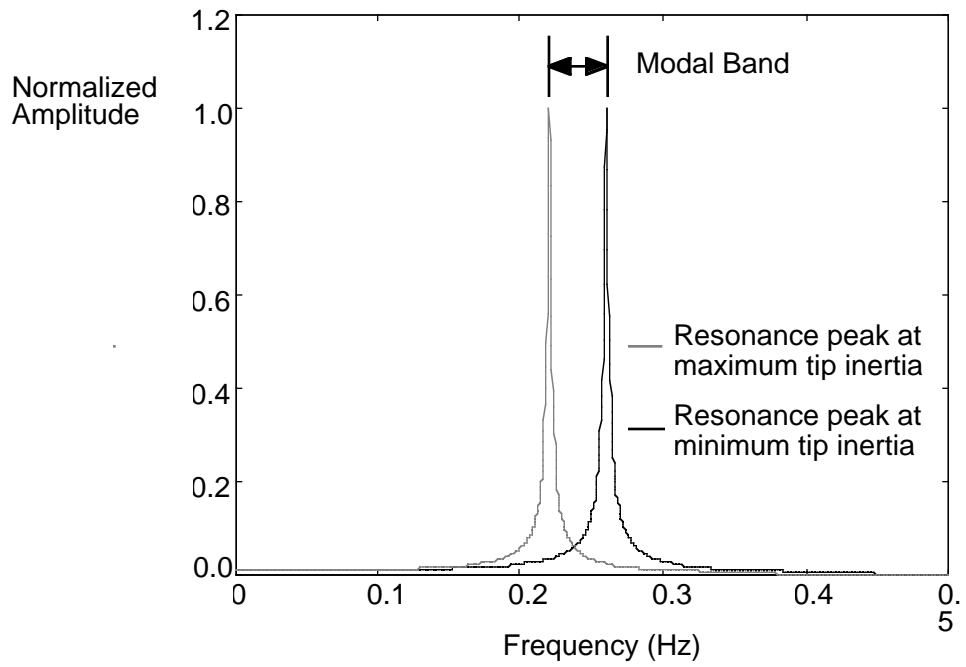


Fig. 36 Structural resonance peak displacement and modal band resulting from solar array rotation.

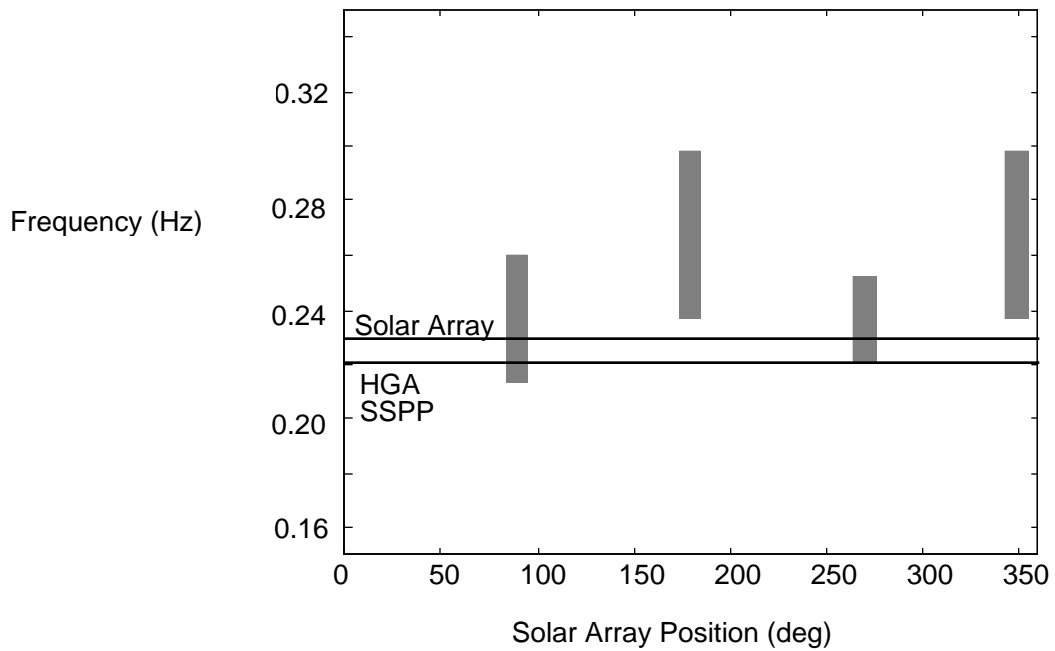


Fig. 37 Solar array modal frequencies range measured from day 128 through day 737 past launch for 90°, 180°, 270° and 360° positions.

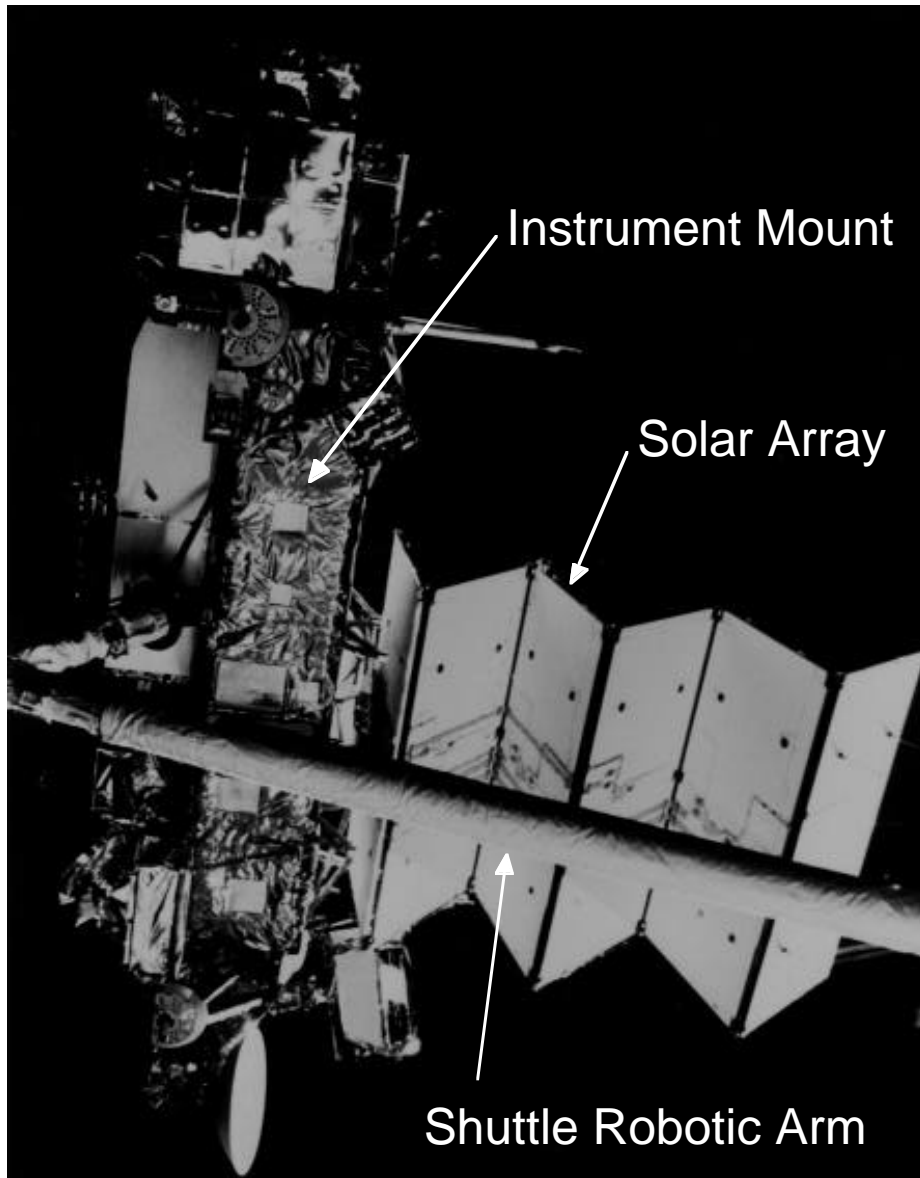
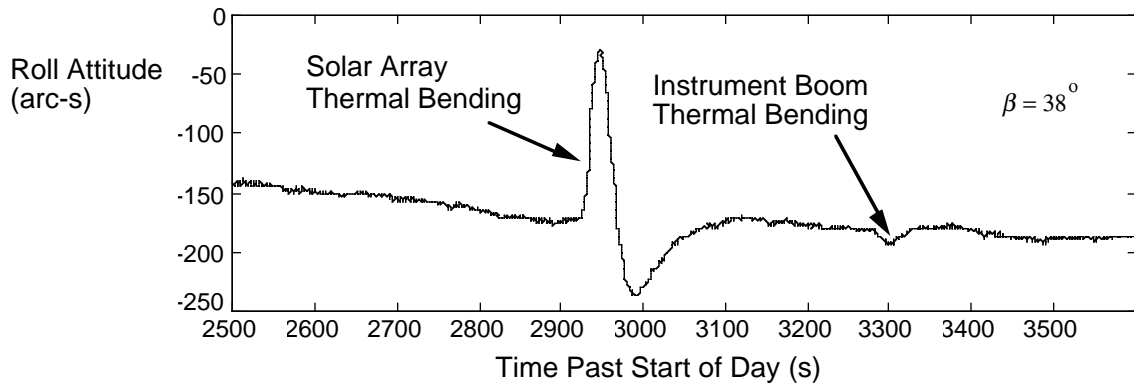
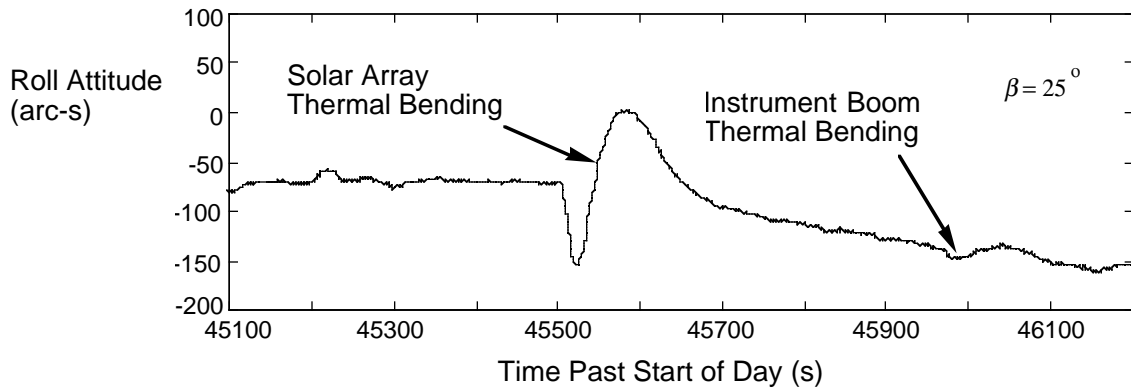


Fig. 38 The Upper Atmosphere Research Satellite being released from the Space Shuttle Discovery (STS-48) robotic arm.



a) Thermal bending on the 139th day after launch



b) Thermal bending on the 370th day after launch

Fig. 39 UARS attitude response to thermal elastic bending of the solar array and instrument boom.

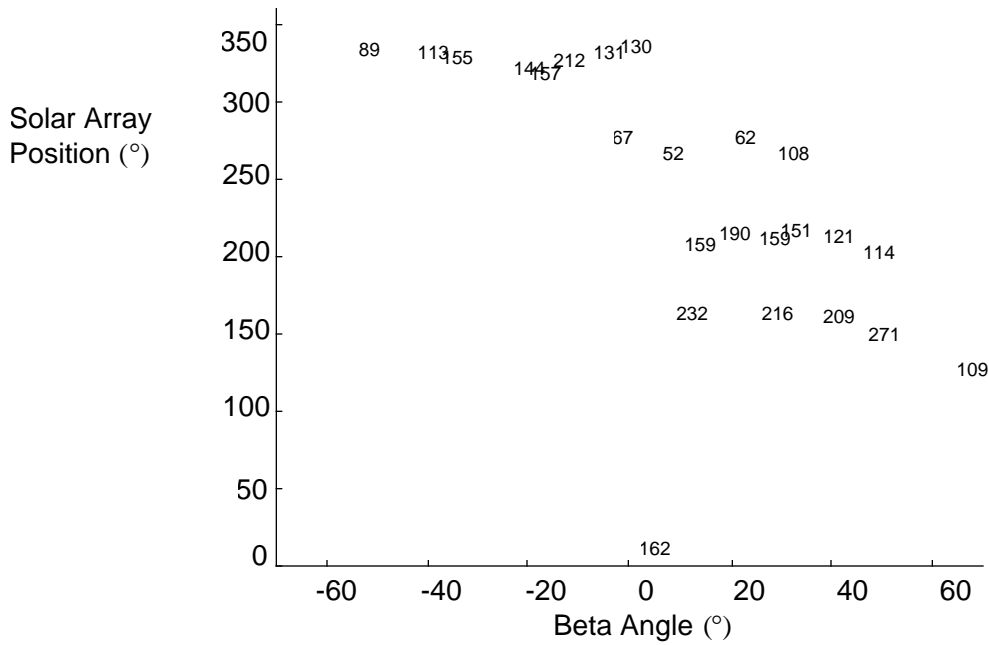


Fig. 40 Variation of sunrise thermal snap trough-to-peak roll attitude displacement with solar array position and Beta angle.

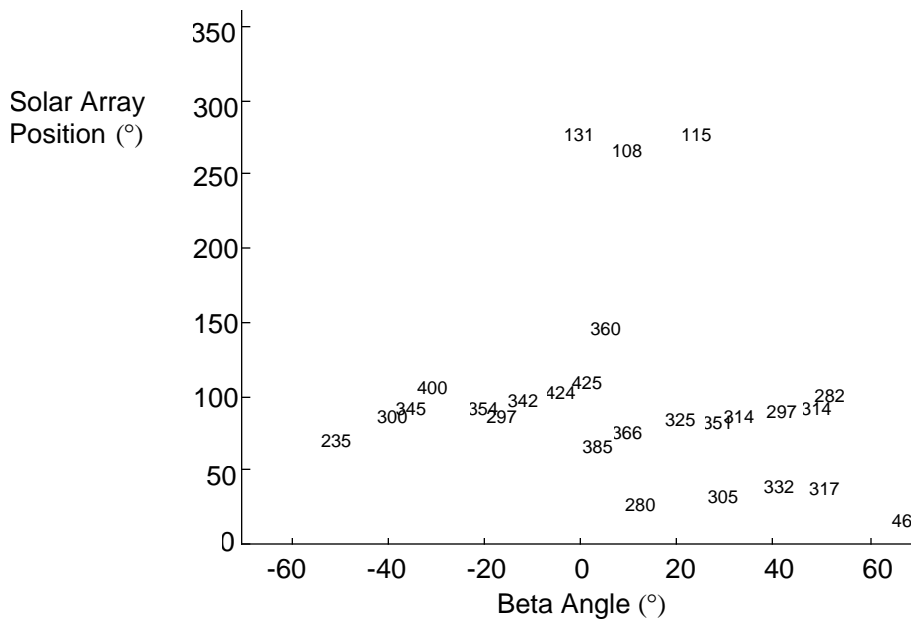
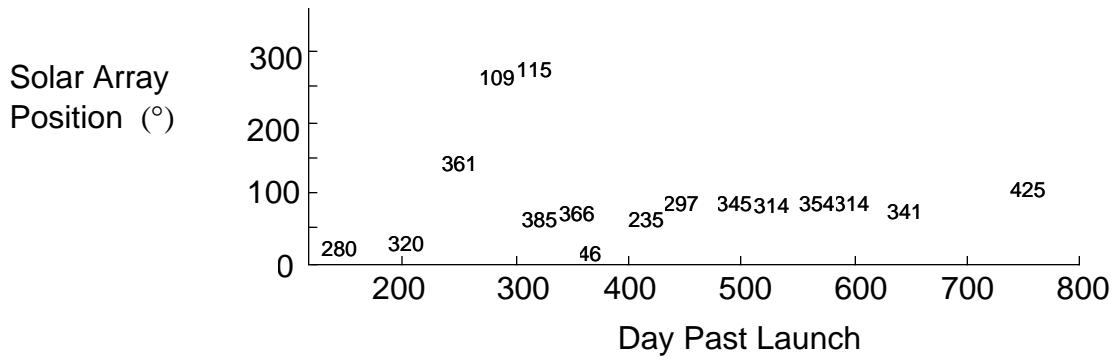
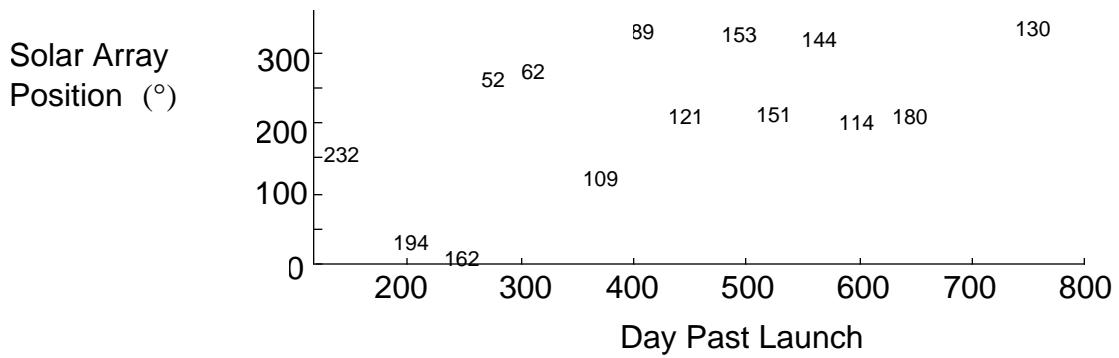


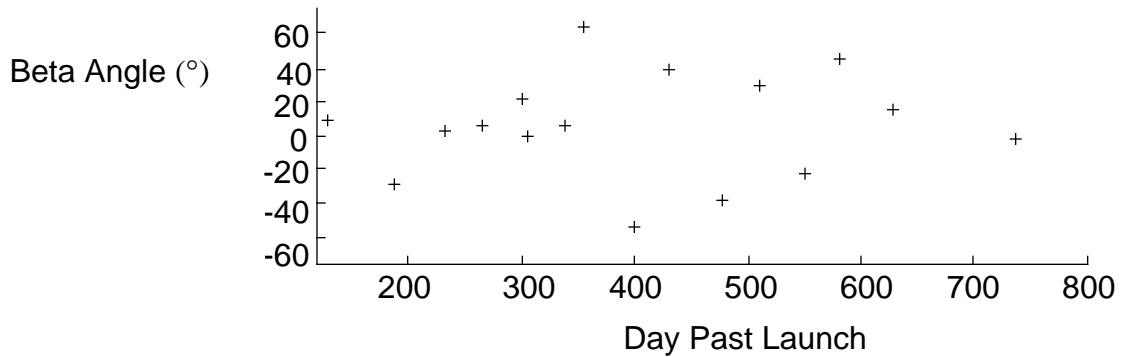
Fig. 41 Variation of sunset thermal snap trough-to-peak roll attitude displacement with solar array position and Beta angle.



a) Roll attitude displacement during sunset thermal snap (arc-s)



b) Roll attitude displacement during sunrise thermal snap (arc-s)



c) Beta angle during thermal snaps

Fig. 42 Sunset and sunrise thermal snap peak-to-peak displacement variations with solar array position and Beta angle.

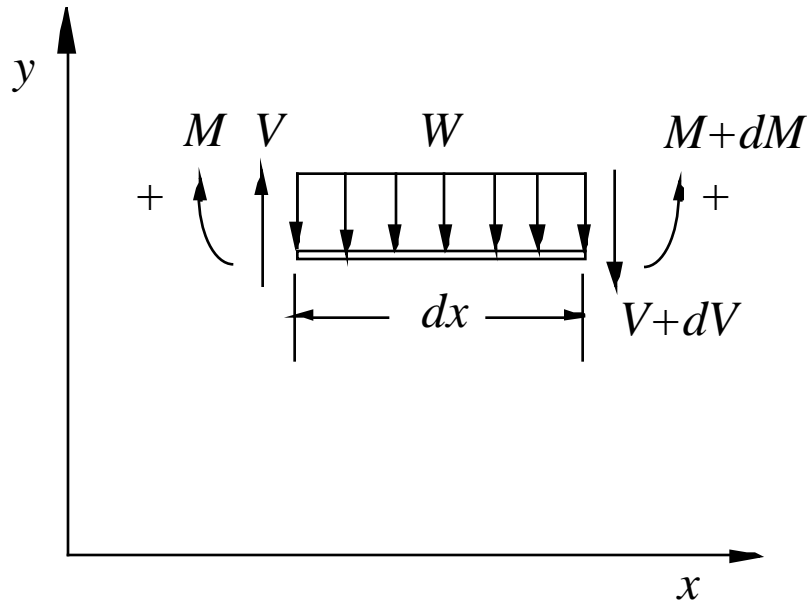


Fig. 43 A beam in bending.

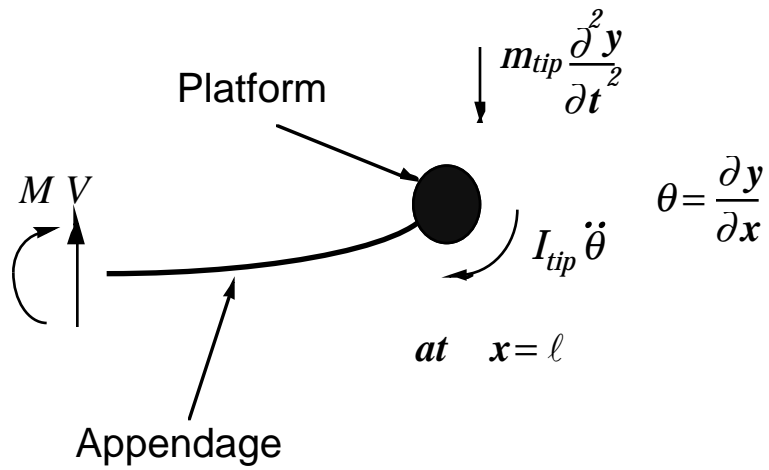


Fig. 44 Boundary conditions for a flexible appendage attached to a space platform.